TRANSVERSE MOMENTUM EVOLUTION OF HADRON-V^0 CORRELATIONS IN PP COLLISIONS AT $\sqrt{S}$ = 7 TEV

A Dissertation

Presented to

the Faculty of the Department of Physics

University of Houston

In Partial Fulfillment

of the Requirements for the Degree

Doctor of Philosophy

By

Sandun Yasassri Jayarathna Pahula Hewage

May 2015

TRANSVERSE MOMENTUM EVOLUTION OF HADRON-V^0 CORRELATIONS IN PP COLLISIONS AT $\sqrt{S}$ = 7 TEV

Sandun Yasassri Jayarathna Pahula Hewage

APPROVED:

Dr. Rene Bellwied, Chairman
Dept. of Physics

Dr. Ed. V. Hungerford
Dept. of Physics

Dr. Lawrence Pinsky
Dept. of Physics

Dr. Kevin Bassler
Dept. of Physics

Dr. Eric Bittner,
Dept. of Chemistry

Dean, College of Natural Sciences and Mathematics

Acknowledgements

TRANSVERSE MOMENTUM EVOLUTION OF HADRON-V^0 CORRELATIONS IN PP COLLISIONS AT $\sqrt{S}$ = 7 TEV

An Abstract of a Dissertation

Presented to

the Faculty of the Department of Physics

University of Houston

In Partial Fulfillment

of the Requirements for the Degree

Doctor of Philosophy

By

Sandun Yasassri Jayarathna Pahula Hewage

May 2015

Abstract

The Large Hadron Collider (LHC) at the European Organization for Nuclear Research (CERN) in Geneva, Switzerland, is capable of accelerating beams of protons (pp) and heavy-ions (Pb+Pb) up to nearly the speed of light which corresponds to center of mass energies of $\sqrt{s}$ = 7 TeV and $\sqrt{s_{NN}}$ = 2.76 TeV, respectively. The goal of pp program is to investigate physics of and beyond the standard model, while the heavy-ion program attempts to characterize the properties of a new state of matter called the Quark Gluon Plasma. The main aim of this dissertation is to identify particle production mechanisms in pp collisions, also as a reference for possible modifications due to the plasma formation in heavy-ion collisions. Two-particle azimuthal correlation measurements were employed, which allow the study of high-p_T parton fragmentation without full jet reconstruction. We present the results of correlations between charged trigger particles and associated strange baryons (Λ) and mesons (K^0_S). Enhancements of the azimuthal correlations are seen at $\Delta\varphi \approx 0$ and $\Delta\varphi \approx \pi$, resulting from back-to-back jet fragmentation in the parton center-of-mass system. Two model fit functions were introduced to characterize the properties of the jet peaks. Hard and soft yields were seperaded using the ZYAM method and extracted yields were compared with pQCD inspired models and inclusive spectra. The analysis was performed in different multiplicity bins to detect possible enhancements of Λ or K^0_S yields and the Λ/K^0_S ratio. The latter was observed in high multiplicity Pb+Pb collisions and interpreted as a novel production mechanism in the deconfined medium produced at the LHC. A novel data-driven feeddown correction for Λ is also introduced, which could allow a more accurate calculation of the primary Λ.

Contents

List of Figures

List of Tables

Chapter 1

Introduction to relativistic heavy-ion physics

From a Chimpanzee to Homo sapiens, human evolution took more than eighty five million years [1]. So, what makes the Homo sapiens more superior than the Neanderthal [2], who was his predecessor?. It is none other than our curiosity which makes us so special. Most of the modern scientific discoveries were triggered by human curiosity. We continuously ask questions and do our own research to find answers. One of the most puzzling questions we sought answers was, "What are the fundamental building blocks of nature?" From earth, water, fire and air to quarks, gluons and leptons it took more than ten centuries to solve this puzzle piece by piece. Anaximenes of Miletus, back in the latter half of the 6th century BC, thought that everything was made out of earth, water, fire and air [3]. In 1869 Dimitri Mendeleev published his periodic table of the elements [4]

and people believed that these elements were the fundamental building blocks of nature until J.J. Thompson discovered the electron back in 1900 [5]. Everything was changed in 1911 when Ernest Rutherford discovered the positively charged nucleus in his classic scattering experiment [6]. Over the past few decades experimental high energy physicists used powerful particle accelerators coupled with state of the art detectors and found thousands of new particles which are commonly known as the particle zoo. The existence and interactions of these particles are explained in a theory called the standard model of particle physics. In this chapter, I will describe the introductory theory associated with the standard model, mainly the theory of strong interaction, which is called Quantum Chromo Dynamics. Then, I will discuss some properties of this theory which are relevant to relativistic heavy-ion collisions, such as asymptotic freedom and the confinement of quarks and gluons into hadrons. These properties are crucial to the understanding of the phenomenon of quark deconfinement in relativistic heavy-ion collisions. The main scientific breakthrough of relativistic heavy-ion collisions compared with proton proton collisions is the creation of a new state of matter called the quark gluon plasma. Some of it s important properties and how physicists probe this new state of matter using different observables are briefly outlined in the following.

1.1 The standard model of particle physics

The standard model of particle physics [7, 8, 9, 10, 11] is a quantum field theory which describe the interaction of Electromagnetic, Weak and Strong forces between fundamental particles. It can be subdivided into two main components. The first is the set of elementary particles of which all matter is made and the second is the interaction between those elementary particles. The twelve elementary particles, all fermions[1], are equally divided between quarks and leptons. These twelve elementary particles and some of there important properties are summarized in the table 1.1.

Generation	Quarks			Leptons		
	Name	Charge	Mass	Name	Charge	Mass
1	u	$2/3e$	1.7-3.3 MeV/c^2	e	$-e$	0.511 MeV/c^2
	d	$-1/2e$	4.1-5.8 MeV/c^2	ν_e	0	< 2 eV/c^2
2	c	$2/3e$	$1.27^{+0.07}_{-0.09}$ GeV/c^2	μ	$-e$	106 MeV/c^2
	s	$-1/2e$	101^{+29}_{-21} MeV/c^2	ν_μ	0	< 0.19 MeV/c^2
3	t	$2/3e$	172±0.9 GeV/c^2	τ	$-e$	1.78 GeV/c^2
	b	$-1/2e$	$4.19^{+0.18}_{-0.06}$ GeV/c^2	ν_τ	0	< 18.2 GeV/c^2

Table 1.1: Elementary particles in the standard model [12].

[1] Obey Fermi–Dirac statistics and the Pauli exclusion principle

The fundamental particles are divided into three generations, each consisting of a charged lepton, a neutrino and two corresponding quarks. The six different (flavor) quarks are called up (u), down (d), strange (s), charm (c), top (t), and bottom (b). Quarks of the second and third generations are unstable and decay into quarks of previous generations; the only stable family of quarks in the standard model is the first generation. The six different leptons are comprised of the electron (e), the muon (μ), and the tau (τ), each carrying an electric charge of 1.6×10^{-19} Coulomb, and the neutral neutrinos of the same generations, namely the electron neutrino (ν_e), the muon neutrino (ν_μ), and the tau neutrino (ν_τ). Each of these twelve particles has an antiparticle partner with all the same features such as spin and mass, but opposite charge (electric, weak, color). There are four force carrier bosons[2], which are called gauge bosons, and one special boson called the Higgs, which is responsible for the generation of mass of all particles [13, 14]. The four categories of possible interactions occur through an exchange of the gauge bosons. All known interactions and associated gauge bosons are outlined in Table 1.2. Gravitation is not included in the standard model and described separately in the general theory of relativity [15]. Quarks are the only fundamental particles that interact strongly because of carrying a color charge; however, since they also carry electric charge and weak isospin, they interact both electromagnetically and weakly. All neutrinos interact only via the weak interaction due to no color and electric charge, while e, μ and τ can interact both electromagnetically and weakly.

[2]Obey Bose–Einstein statistics and have integer spin

Force	Strength	Gauge Boson(s)	Theoretical framework
Electromagnetic	10^{-2}	Photon (γ)	Quantum Electro Dynamics
Weak	10^{-7}	$W^{\pm}$, Z	Quantum Flavor Dynamics
Gravitational	10^{-39}	Gravitons	General theory of relativity
Strong	1	8 Gluons (g)	Quantum Chromo Dynamics

Table 1.2: Gauge bosons in the standard model.

1.1.1 Quantum Electro Dynamics (QED)

QED was developed by Shinichiro Tomonaga, Julian S. Schwinger, Richard P. Feynman and Freeman Dyson back in 1946 and 1950 as the quantum theory of light interacting with charged matter [16]. In classical electrodynamics, forces arise from potentials V(r) acting instantaneously on a charge particle at a given distance [17], but in QED forces are described by the exchange of virtual field quanta called photons. QED is an Abelian gauge theory where gauge field quanta are not self interacting and explained by U(1) group theory. All electromagnetic processes such as scattering, decay, absorption and emission are described by Feynman diagrams [18].

1.1.2 Quantum Flavor Dynamics (QFD)

QFD was developed by Sheldon Glashow Lee in 1961, and completed in 1967 by Abdus Salam and Steven Weinberg. QFD describes the weak interaction of quarks and leptons by exchanging the $W^{\pm}$ and Z^0 bosons. This weak interaction is responsible for the transition from one flavor of quark to another flavor of quark in the order of $t \rightarrow b \rightarrow c \rightarrow s \rightarrow u \leftrightarrow d$ [19]. The basic mathematical framework behind the weak interaction is SU(2) group theory [20]. Beta decay, which is the decay of a neutron to a proton, is governed by the weak interaction. In this scenario one down quark of the neutron decays into an up quark by emitting a W^- that then produces an electron and an anti electron neutrino ($\bar{\nu}_e$) [21]. Figure 1.1 lists all known quark and weak boson interactions.

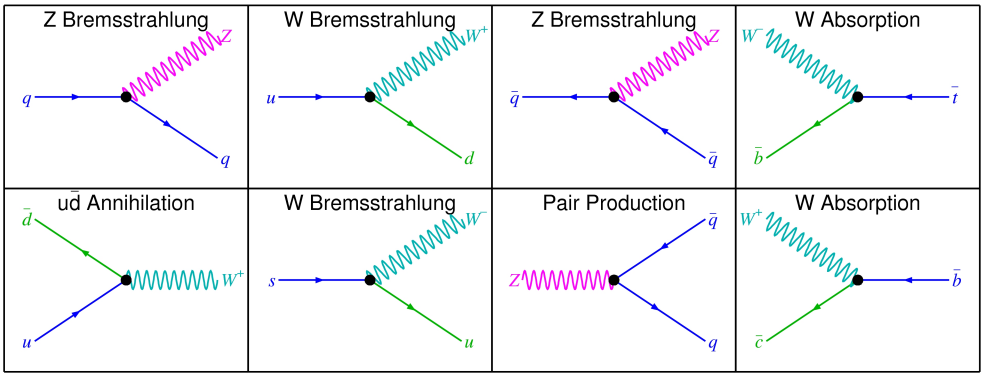

Figure 1.1: Weak quark vertices.

1.1.3 Hadrons in the standard model

In the late 1960s the so-called "eightfold path" was proposed by Murray Gell-Mann, according to which matter is comprised of quarks [22]. One puzzle of this theory was to describe the quark configuration of Ω^-, in which there are three quarks of the same flavor and spin 1/2, which was a direct violation of the Pauli exclusion principle. To avoid this conflict an additional degree of freedom was introduced, named color charge, which can be red (r), blue (b) or green (g). Anti quarks can be anti red ($\bar{r}$), anti blue ($\bar{b}$) or anti green ($\bar{g}$). Thus, composite particles predicted in the Standard Model are clusters of quarks and anti-quarks, commonly known as hadrons. There are two combinations of quarks that result in colorless[3] hadrons. Baryons, formed by three quarks (rgb) and their anti-baryons ($\bar{r}\bar{g}\bar{b}$). Examples are the proton (duu) and neutron (ddu). Mesons are formed by a quark and an anti-quark pair such as $r\bar{r}$. Examples are the pion and kaon.

1.2 Quantum Chromo Dynamics (QCD)

QCD describes the strong interaction between quarks. The strong interaction is mediated by the gauge boson of the strong interaction, the gluon. Gluon carry a combination of color and an anti-color charges, which results in a self-interaction between gluons, explained in the non-Abelian gauge theory of SU(3) [23]. In non-Abelian theories gauge invariance is achieved by adding n^2-1 gauge bosons of

[3]Color neutrality is obtained with a complementary combination of color and/or anti-color quarks

SU(n). This gives eight different gauge bosons (eight different gluons) as mediators in the strong interaction (for n=3, n^2-1=8). As an example, Figure 1.2 shows a g-quark interaction with a b-quark by emitting a $g\bar{b}$ gluon. This theory has been developed progressively and the last major contribution was by David J. Gross, H. David Politzer and Frank Wilczek with the discovery of asymptotic freedom, which was awarded the Nobel prize in 2004. Most of the physics in hadronic collisions is explained by QCD, thus the proper understanding of QCD is the basis of high energy physics.

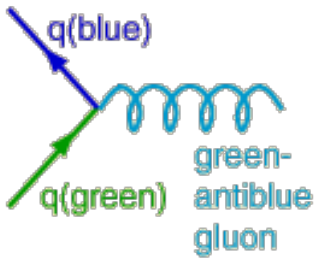

Figure 1.2: g quark interaction with b quark by emitting $g\bar{b}$ gluon.

1.2.1 The Lagrangian of QCD

We will mainly focus on the fundamental theory of strong interactions, QCD, based on the SU (3) special, unitary group in three (complex) dimensions. The QCD Lagrangian density, which describes the interaction of spin-half quarks of mass m and spin-one massless gluons is given by [24]

$$\mathcal{L}_{QCD} = \mathcal{L}_{Yang-Mills} + \mathcal{L}_{fermion} + \mathcal{L}_{gauge-fixing} + \mathcal{L}_{ghost} \tag{1.1}$$

- Here $\mathcal{L}_{Yang-Mills}$ describe the contribution from eight different gluons,

$$\mathcal{L}_{Yang-Mills} = -\frac{1}{4}\mathcal{F}^{A}_{\alpha\beta}\mathcal{F}^{\alpha\beta}_{A} \tag{1.2}$$

where $\mathcal{F}^{A}_{\alpha\beta}$ is the field strength tensor for the gluon field A^{A}_{α},

$$\mathcal{F}^{A}_{\alpha\beta} = \partial_{\alpha}A^{A}_{\beta} - \partial_{\beta}A^{A}_{\alpha} - gf^{ABC}A^{B}_{\alpha}A^{C}_{\beta} \tag{1.3}$$

The indices A, B and C run over the color degrees of freedom of the gluon field (1,2..8). The third term in equation 1.3 is a non-Abelian term which distinguishes QCD from QED. This is the most important term which gives rise to gluon self-interactions. The coupling constant, g, determines the strength of the interaction between colored partons, and f^{ABC} are the structure constants of the SU(3) color group.

- $\mathcal{L}_{fermion}$ give rise to the contribution from quark fields.

$$\mathcal{L}_{fermion} = \sum_{flavors} \bar{q}_{A}(i\gamma^{\mu}D_{\mu} - m)_{AB}q_{B} \tag{1.4}$$

The quark fields q_A are in the triplet representation of the color group and D is the covariant derivative [25]. The sum over flavors is a sum over the different flavors of quarks.

- To make calculations in perturbation theory from a gauge invariant Lagrangian, we need to mention the specific gauge in which to calculate. The usual gauge-fixing term is given by

$$\mathcal{L}_{gauge-fixing} = -\frac{1}{2\lambda}(\partial^{\alpha}A^{A}_{\alpha})^{2}. \tag{1.5}$$

λ=1 corresponding to the Feynman gauge and $\lambda \to 0$ gives the Landau gauge.

- To cancel out the unphysical gluon polarization introduced by the gauge-fixing terms, we introduce the ghost term.

$$\mathcal{L}_{ghost} = \partial_\alpha \eta^{A\dagger}(D^\alpha_{AB}\eta^B) \tag{1.6}$$

  where η^A is a complex scalar field which obeys Fermi statistics.

This explains the complete Lagrangian shown in equation 1.1.

$$\mathcal{L}_{QCD} = -\frac{1}{4}F^A_{\alpha\beta}F^{\alpha\beta}_A + \sum_{flavors}\bar{q}_A(i\gamma^\mu D_\mu - m)_{AB}q_B - \frac{1}{2\lambda}(\partial^\alpha A^A_\alpha)^2 + \partial_\alpha\eta^{A\dagger}(D^\alpha_{AB}\eta^B) \tag{1.7}$$

1.2.2 The confinement of quarks and asymptotic freedom

One of the key features of strong interactions is that gluons interact with each other due to the term $gf^{ABC}A^B_\alpha A^C_\beta$ in equation 1.7. This does not occur in the theory of quantum electrodynamics, in which there is no interaction between photons. One consequence of this fact is that the coupling constant (α_s) decreases with increasing energy, which is known as asymptotic freedom. The decrease of α_s with increasing momentum transfer can be seen in Figure 1.3. In high energy collisions, the particles which have large transverse momentum exchanges, the value of the coupling constant is reduced, which allows us to use perturbation theory. In this regime it is expected that models inspired by pQCD (perturbative QCD) would have the greatest success in reproducing the data. On the other hand, at low energies the coupling constant becomes strong. In this energy regime, the

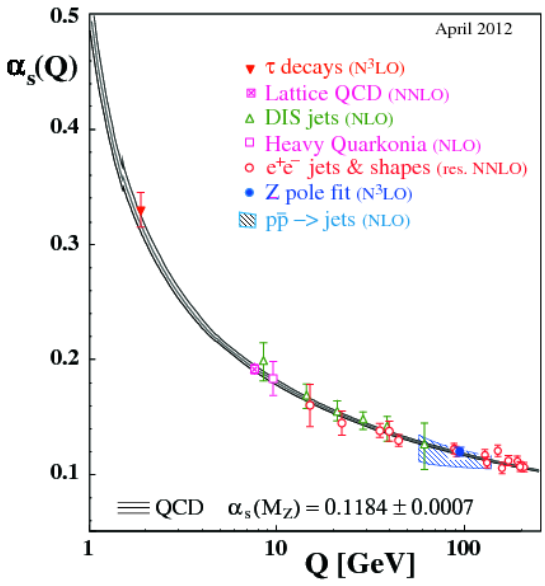

Figure 1.3: Measurements of α_s as a function of the momentum transfer Q [26].

perturbative theory does not converge and it is necessary to use other calculation strategies, namely non-perturbative QCD, using techniques such as Lattice QCD.

Another important consequence of gluon self-interactions is that the potential between two quarks is fundamentally different compared with the QED interaction of two electrons. The effective potential between two quarks separated by distance r is given in equation 1.8.

$$V_{eff} = -\frac{4}{3}\frac{\alpha_s \hbar c}{r} + kr \tag{1.8}$$

Empirically, the potential V_{eff} increases as the distance between the colored particles r becomes larger. Thus, for very small values of r a Coulomb type potential $(1/r)$ dominates and quarks are almost free. Moreover, when r increases, the potential has the form $V(r) = kr$, due to the string tension. Thus, it would

require an infinite amount of energy to separate two quarks. In high energy collisions, the energy available for the two quark system ($Q\bar{Q}$) exceeds the amount of energy required to create a new quark and anti-quark pair ($q\bar{q}$), as shown in Figure 1.4. Therefore, the initial quark Q does not have a color-singlet state with $\bar{Q}$ any longer, but with $\bar{q}$. This explains the nonexistence of isolated quarks and the reason why all quarks are usually confined into hadrons.

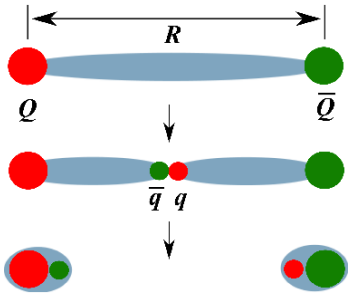

Figure 1.4: The QCD string breaking between two quark anti-quark pair [27].

1.2.3 Deconfinement of quarks

Lattice QCD predicts that, at very high energy densities and temperatures near 170 MeV, where the distance between the hadrons comes close to the range of the strong force ($\sim 1 fm$), hadrons crossover to a state where the quarks and gluons become the proper degrees of freedom, and their motion is no longer confined inside the hadrons [28]. This scenario is depicted in the Figure 1.5. The effective deconfinement of quarks and gluons transforms normal hadronic matter to a new state of matter called the Quark Gluon Plasma (QGP) [29, 30]. In the QGP, quarks and gluons can move freely, analogous to electrons in classical electromagnetic

plasma. According to the Standard Model, QGP formation restores fundamental symmetries that are usually not valid at low energies [31].

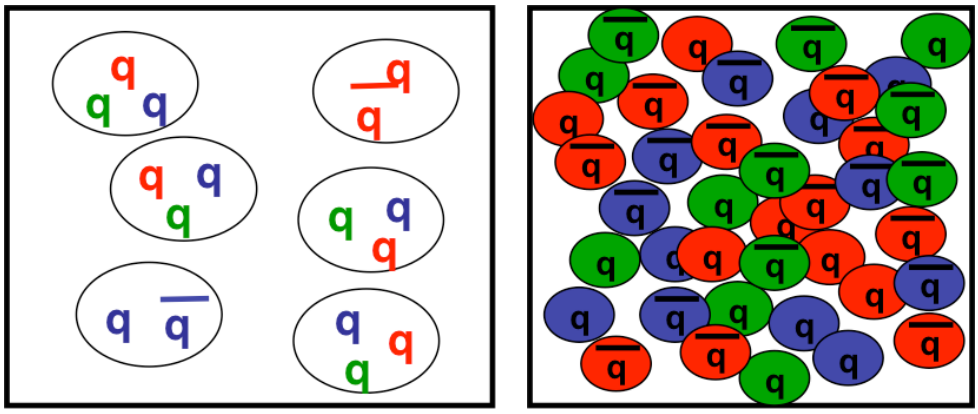

Figure 1.5: Deconfined quarks and gluons at high energy densities. Left figure shows normal nuclear matter where the quarks and gluons are confined. Black circles indicate the color-neutral hadrons. Right figure shows the deconfined matter, where colored constituents are able to move freely within the system.

1.3 The study of the Quark Gluon Plasma (QGP)

The QGP allows us to study hadronization [32, 33], confinement mechanisms, chiral symmetry breaking and the phenomenon of hadron mass generation. In addition to further understanding the theory of QCD, the QGP could also teach us about the Big Bang. It is believed that in the primordial epochs of the universe, all matter was concentrated in a very small volume, and in this scenario, during the first few microseconds of the universe matter should have existed as a state of deconfined quarks and gluons. Thus, there is interest in looking for similarities

between the process of evolution of the QGP system and the evolution of the early universe.

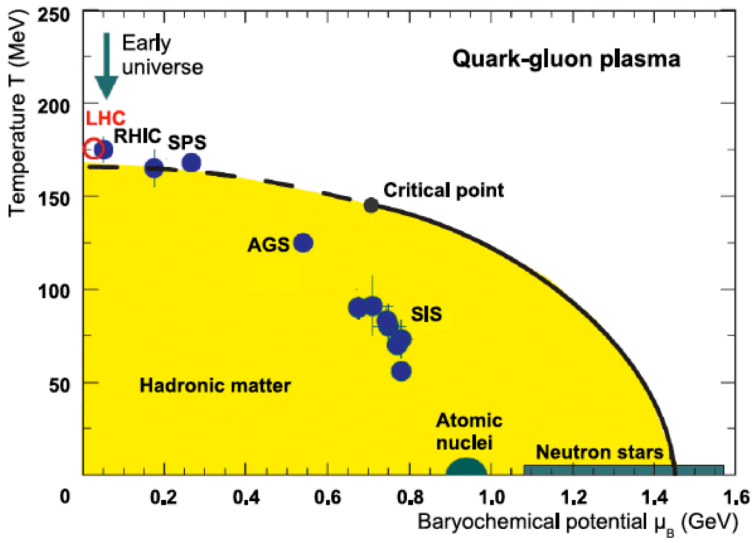

Figure 1.6: Phase diagram of QCD and the phase transition between hadronic matter and a QGP [34].

Figure 1.6 shows the phase diagram of QCD matter [35] as a function of temperature and net baryon density (baryon chemical potential). In high energy experiments, at RHIC and the LHC, it is estimated that producing an equal number of particles and anti-particles results in a baryonic density very close to zero (far left side of Figure 1.6). Under these conditions ($\mu_B \approx 0$, high temperatures) a crossover phase transition from normal hadronic matter to QGP is predicted by lattice QCD calculations. This is shown as a dashed line in the phase diagram. At high net μ_B and low temperatures, which is equivalent to conditions in neutron stars [36], a large hadronic density is reached by gravitational attraction, a first

order phase transition to a color super conducting phase might occur, indicated by a solid line in the phase diagram. At the end of the first-order phase transition line is the posited critical point of the QCD phase, where pressure in the hadronic and QGP phases are equal.

1.4 Little bangs and creation of the QGP in the laboratory

The Cosmological Big Bang Theory is the most effective theory to explain the very beginning of our universe [37, 38, 39]. As shown in Figure 1.7 (left), it all started from a singular point. At the beginning the temperature was very high and the universe rapidly cooled down and expanded. After 10^{-10} seconds the universe existed as a QGP and after 10^{-5} seconds all quarks and gluons were bound inside hadrons [40, 41]. Scientists mimic these high energy conditions by colliding two nuclei at nearly the speed of light in so-called relativistic heavy-ion collisions. This is shown in Figure 1.7 (right panel). The main reason for using heavy nuclei is to achieve very high energy densities in a finite volume of matter during the collision. These collisions create a fireball, which will eventually heat and compress and give rise to the conditions shown in Figure of 1.5 (right). The main goal of relativistic heavy-ion collisions is thus to study the properties of the QGP.

The left and right panel of Figure 1.7 share similarities, but there are a few important differences between the Big Bang and the little bang. The actual Big

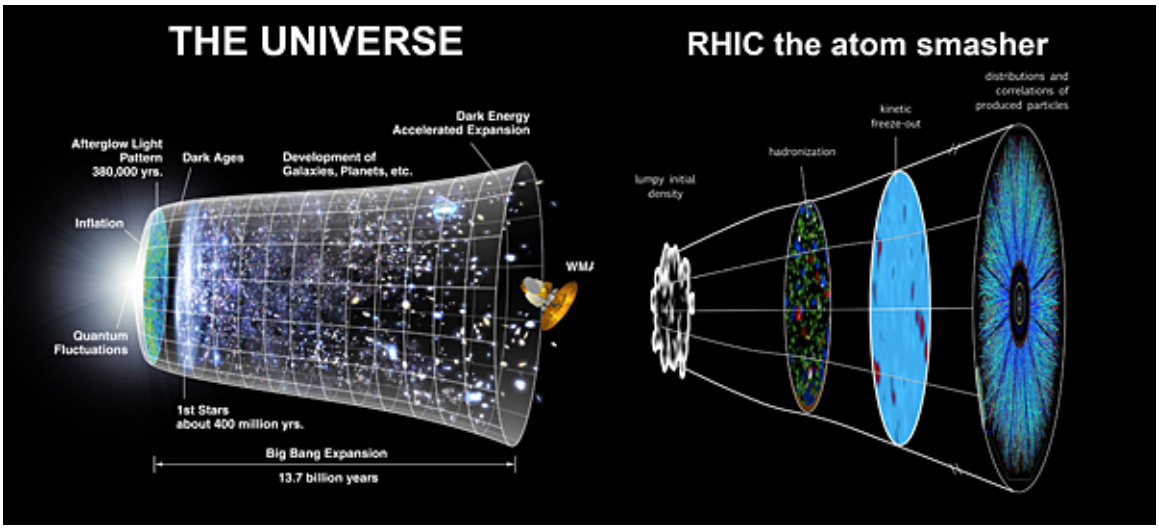

Figure 1.7: Time evolution of the big bang (left) and comparison with a heavy-ion collision (right) [42].

Bang expansion was dominated by gravitational forces while in little bangs there is no contribution from gravity. Therefore the expansion time in the Big Bang is higher than that of little bangs ($\tau_{BigBang} \approx 10\ \mu$s, $\tau_{LittleBang} \approx 4{\times}10^{-23}$ s) [43]. The second difference is the baryon to total particle ratio produced in a little bang is high compared with the Big Bang. This will give rise to a considerable baryon to anti baryon asymmetry in heavy-ion collisions.

Figure 1.8 shows a schematic sketch of the time evolution during a relativistic heavy-ion collision. Initial nucleons are traveling close to the speed of light, so they are highly Lorentz contradicted in the beam direction. In the initial state prior to the collision the distribution of quarks and gluons inside the heavy-ion is modeled by the color glass condensate (CGC) [44, 45, 46]. During the collision, high energy photons and jets are produced through hard scattering of quarks and

gluons. After the collision thermalization takes place and thermal photons are created and the entropy of the system increases. A QGP is produced if the system has a sufficient energy density. Hydrodynamical expansion follows. During this expansion, the temperature and density of the system decrease and hadronization of the QGP phase takes place. Gradually the mean free path between hadrons becomes large, and eventually freeze-out happens. Prior to freeze-out final state interactions play an important role.

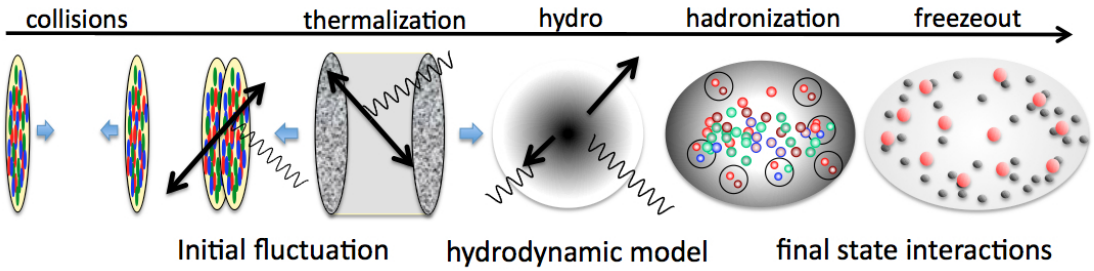

Figure 1.8: Schematic sketch of a relativistic heavy-ion collision. Particles (arrows) and photons (wavy lines) are emitted in several stages of the evolution [47].

Another illustration of the space-time evolution of a high-energy nucleus-nucleus collision is shown in Figure 1.9. Here t represents the time axis and z is the space axis.The two nuclei collide at time t=0. The three distant hyper-surfaces in the space-time evolution are characterized by their respective temperatures T:

1. T_c is the critical temperature at which QGP transition to the hadronic phase.

2. T_{ch} is the chemical freeze out temperature. At this temperature inelastic scatterings between hadronscease and all hadron yields are locked in.

3. T_{fo} is the kinetic freeze out temperature. At this temperature all elastic scattering between hadrons cease and their moments are locked in. At this point free streaming sets in.

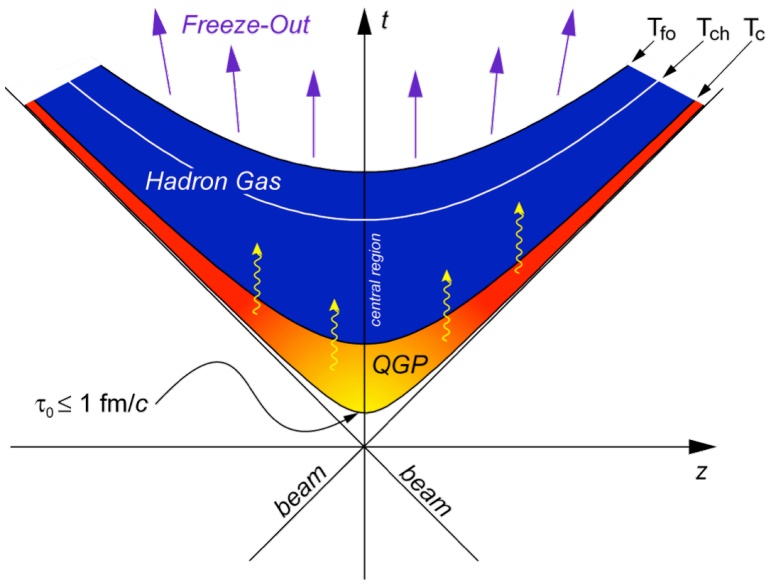

Figure 1.9: Theoretical view of a heavy-ion collision [48].

1.5 QGP formation signals in relativistic heavy-ion collisions

Proton-proton collisions are less extensive and distinct from heavy-ion collisions, since they are not associated with collective phenomena. The characterization of systems resulting from heavy-ion collisions is a major challenge, because it requires observables that are sensitive to the initial state of the collision. The

comparison between observables resulting from pp and A+A collisions allow to identify signatures due to the QGP formation and separate them from effects generally seen in pp collisions. High energy pp collision observables are understood in terms of pQCD-inspired theoretical models; therefore, to identify the QGP formation we are looking for any deviations from pQCD and trying to model them in various theoretical approaches.

1.5.1 Increased rates of strangeness production

Strangeness enhancement is one of the main expected signatures of QGP formation [49, 50, 51]. In the QGP phase, strange quarks will be more abundant than non-strange quarks. The ratio of strange to non-strange quarks in an equilibrating plasma is given by [52];

$$\frac{n_s}{n_q} = \frac{1}{2}\left(\frac{m_s}{T}\right)^2 K_2\left(\frac{m_s}{T}\right) e^{\mu_B/3T} \tag{1.9}$$

Therefore if μ_B >0, the ratio is larger than one. This leads to the production of more strange than non-strange quarks. During the hadronization phase, the abundant strange quarks can become bound, resulting in the enhancement of strange hadron production. One can define the enhancement factor as:

$$E = \frac{1}{N_{part}} \frac{dN^{AA}}{dy} / \frac{1}{2} \frac{dN^{pp}}{dy} \tag{1.10}$$

Figure 1.10 shows the enhancement factor for (multi-) strange particles in Cu+Cu and Au+Au $\sqrt{s_{NN}}$=200 GeV collisions. However, it is still uncertain whether

the enhancement is due to increased production in the QGP or to canonical suppression of strangeness in pp collisions. The canonical suppression arises from the need to conserve strangeness within a small, local volume, which limits the strangeness production in pp collisions relative to A+A collisions. In the language of statistical mechanics, while the canonical ensemble is valid in pp collisions, in A+A collisions, the grand canonical ensemble is applicable. Assuming that the

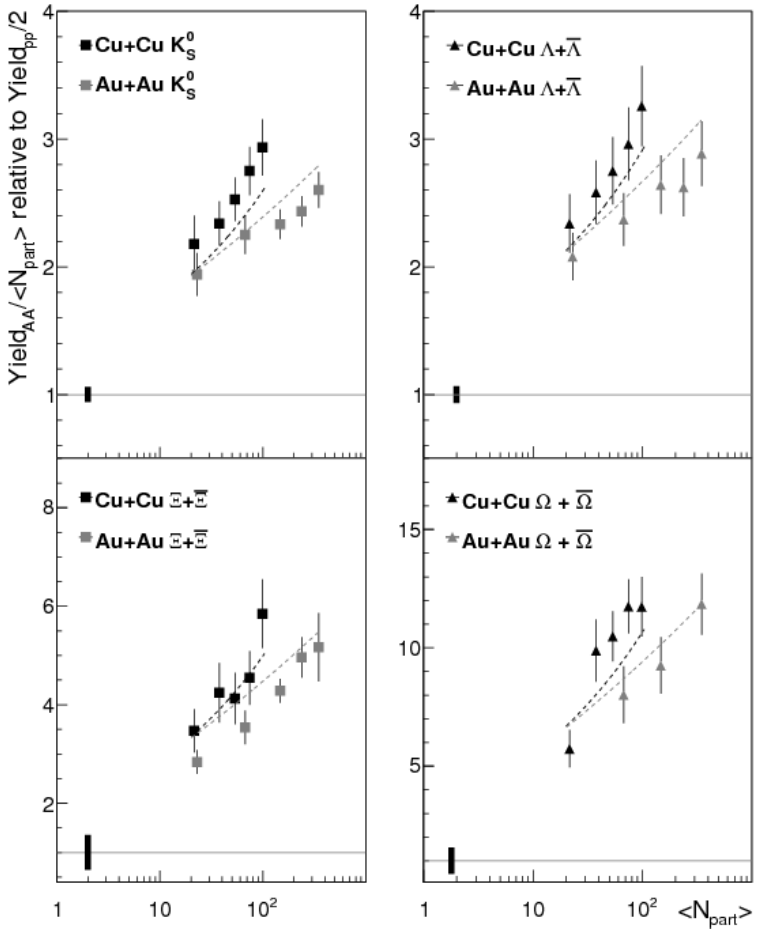

Figure 1.10: The enhancement factor for (multi-) strange particles in Cu+Cu and Au+Au $\sqrt{s_{NN}}$=200 GeV collisions [53].

system correlation volume is proportional to N_{part}, the canonical framework predicts that the yield per N_{part} increases with N_{part} as the phase space restriction due to strangeness conservation is lifted.

1.5.2 Photon production in heavy-ion collisions

The photons production is commonly referred to as "electromagnetic probes," due to they only interact electromagnetically. Since they are emitted during different stages of the collision evolution, we can identify which photons come from the QGP formation [54, 55]. One of the main reasons to study photon production is that they provide undistorted information about their production channels, since photons do not interact with the QGP and are also not affected by final state interactions.

1. Prompt photons: initial hard collisions produce prompt photons. Their production in a nucleon-nucleon reaction a+b $\rightarrow\gamma$+X can be calculated in leading order pQCD.

2. Fragmentation photons: initial hard scattered partons may fragment into photons (q$\rightarrow\gamma$+q).

3. Pre-equilibrium photons: in nucleus-nucleus collisions, an extended QCD medium is produced. Before achieving local thermal equilibrium the medium is in a pre-equilibrium state. Photons will be emitted in the pre-equilibrium stage as well. However, it is difficult to distinguish pre-equilibrium photons

from thermal photons. Simulations with a Parton Cascade Model indicate that pre-equilibrium photon production is equal to the thermal photon at p_T = 2 GeV. Low p_T photons are predominantly thermal.

4. Thermal photons: photons emitted from the (locally) equilibrated QGP and hadronic matter are called thermal photons. For QGP diagnostic purposes, these photons are the most important probes. In the QGP phase, the most important reactions for direct photon production are:

   (a) Pair annihilation $\bar{q}$+q →g+γ

   (b) Compton process q+g →q+γ

   (c) Bremsstrahlung q+q →$qq\gamma$

In Figure 1.11, the transverse momentum dependence of the invariant cross section in $\sqrt{s}$ = 200 GeV pp collisions and the invariant yield in $\sqrt{s_{NN}}$ = 200 GeV Au+Au collisions are shown. The three curves on the pp plot represent NLO pQCD calculations. For p_T > 2 GeV, the pQCD calculation is consistent with the pp data within the theoretical uncertainties. The dashed curves on the Au+Au plots are obtained by scaling the photon yield in pp collisions by the nuclear overlap function T_{AA}. At p_T < 2.5 GeV, the experimental Au + Au data are underestimated. At low p_T, the photon production increases faster than the binary NN collision scaled pp cross section. The solid lines in Figure 1.11 are fitted with an exponential plus binary collision scaled pp data. The results confirm the dominance of thermal radiation in the direct photon spectrum in the low and intermediate p_T range.

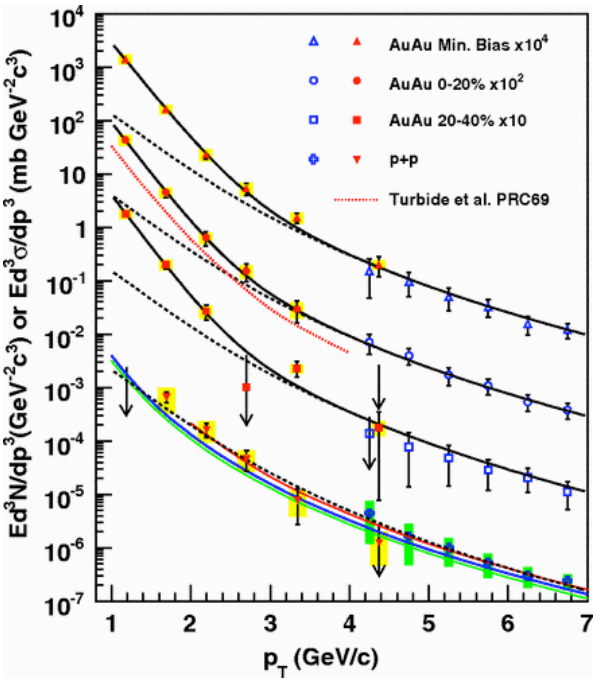

Figure 1.11: Invariant cross section (pp) and invariant yield (Au+Au) of direct photons as a function of p_T [56].

1.5.3 Jet quenching

Jets are clusters of several hadrons, all moving in approximately the same direction [57]. In hadron-hadron or in e^+e^- collisions one generally observes two jet structures with back-to-back distributions. In nucleus-nucleus collisions the jet structure is not obvious due to the large number of particles. However, jets are there and one can use specific jet algorithms to identify them [58]. The Jet structure in hadron-hadron collisions can be understood qualitatively in pQCD. The jet properties depend in general on two scales, the energy of the jet and its largest possible transverse momentum of one of its dijects. The basic two body

reaction 1 + 2 $\rightarrow$ 3 + 4 occurs at the quark or gluon level. The scattered partons are radiating gluons or splitting into quark-antiquark pairs. Such parton branching is governed by the DGLAP equation [59, 60]. Finally, the partons fragment into hadrons. The characteristic collimated hadrons from the fragmentation of an outgoing parton are called jets. Tthe most commonly observed structure seen is the two jet event. The reasoning behind jet quenching in heavy-ion collisions is that when a partonic jet travels through a dense medium, it will lose its energy via gluon radiation. The energy-degraded parton will ultimately fragment into a fewer number of particles above a fixed high momentum than it would have in the absence of a medium. High p_T particle suppression is usually expressed in terms of the nuclear modification factor R_{AA}:

$$R_{AA}(p_T) = \frac{(1/N_{evnt}^{AA}) d^2N_{ch}^{AA}/d\eta dp_T}{< N_{coll} > (1/N_{evnt}^{pp}) d^2N_{ch}^{pp}/d\eta dp_T} \tag{1.11}$$

If a A+A collision is a superposition of pp collisions, the expected ratio is unity. Figure 1.12 (left) shows the R_{AA} for central and peripheral Pb-Pb collisions measured in the ALICE experiment. A clear deviation of R_{AA} is seen for both centralities. Since peripheral collisions are almost identical with pp collisions (in terms of produced particle multiplicites), the nuclear modification factor reaches nearly a constant value after $p_T > 2$ GeV. This reflects the fact that produced particles experience no medium effects in high p_T for pp or peripheral systems. In central collisions, R_{AA} shows a strong dependence on p_T for the full p_T range.

Figure 1.12 (right) shows the comparison of all measured R_{AA} in ALICE, STAR

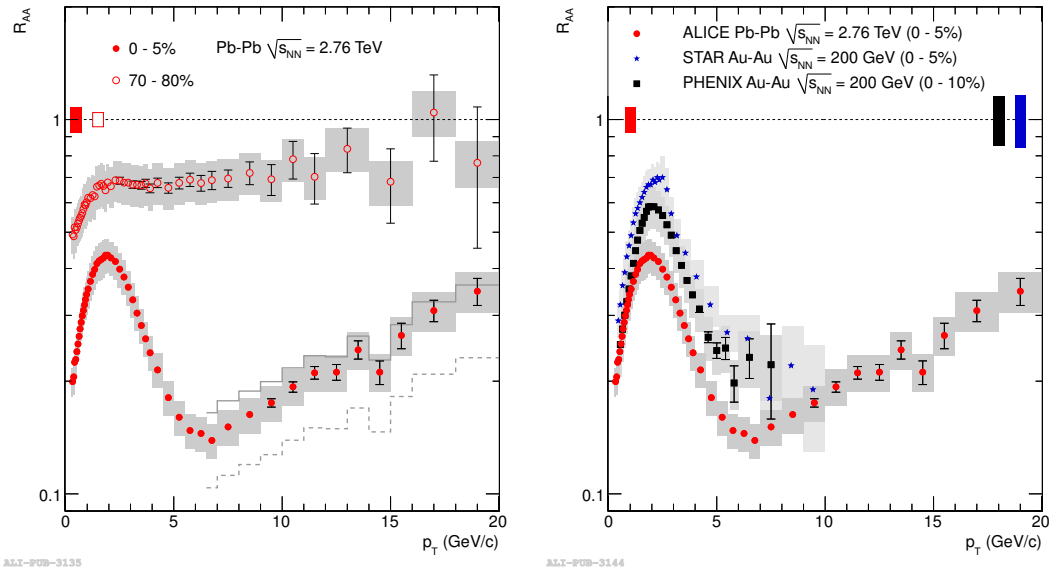

Figure 1.12: Nuclear modification factors of charged particles in central and peripheral Pb-Pb collisions (left). Nuclear modification factors of charged in central Pb-Pb collisions in comparison to RHIC results(right) [61].

and PHENIX experiments. We see a much stronger suppression at the LHC than at RHIC at hight p_T. The main conclusion is that at the LHC we have a larger energy loss and the produced QGP medium is denser than at RHIC.

1.5.4 J/ψ suppression

In heavy-ion collisions heavy quarks are expected to be produced only during the early partonic scattering state. Thus they will coexist with the surrounding medium. Therefore, the measurement of heavy flavor hadrons can provide useful information about the properties of the strongly interacting medium [62, 63]. The

J/ψ particle is a bound state of a $c\bar{c}$ quark pair and can be reconstructed via leptonic decay channels. In the QGP environment color charge is subject to screening due to the medium and the heavy quark anti-quark binding gets weakened. This will lead to a vanishing strong potential term in equation 1.6 and the new potential is given by the Cornell potential [64]:

$$V_{eff} = -\frac{4}{3}\frac{\alpha_{eff}}{r}e^{-r/\lambda_D} \tag{1.12}$$

Here λ_D is the screening length. If λ_D is less than the bound state radius of $< r^2_{J/\psi} >^{1/2}$ then it is impossible to bind a $c\bar{c}$ quark pair inside the QGP. Therefore we will observe a suppressed J/ψ production in relativistic heavy-ion collisions compared to pp collisions. The screening strength will depend on the temperature of the medium and thus the J/ψ yield can be used as a thermometer in the deconfined matter [65]. Figure 1.13 shows the inclusive J/ψ R_{AA} as a function of the charged-particle density (left) and number of participating nucleons (right) measured in ALICE compared with PHENIX results. Here charged particle density is related to the energy density of the created medium. A clear J/ψ suppression is observed in all charged particle densities considered. Moreover measured J/ψ R_{AA} in ALICE is three times larger than measured in PHENIX for $dN_{Ch}/d\eta >$ 600.

1.5.5 Resonance production

Resonance particles are short lived particles with a mean lifetime of 10^{-23}s. Due to this short lifetime they decay inside the deconfiend medium or the dense hadronic

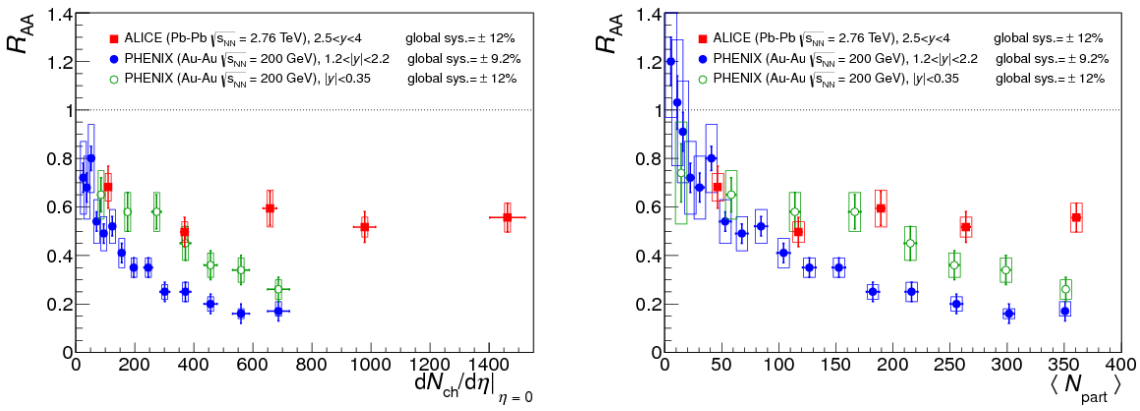

Figure 1.13: Inclusive J/ψ R_{AA} as a function of the charged-particle density (left) and number of participating nucleons (right) measured in ALICE at $\sqrt{s_{NN}}$ = 2.76 TeV TeV compared to PHENIX results at $\sqrt{s_{NN}}$ = 200 GeV [66].

states decaying in the cooling process. The formation time of a hadron is given by [67]:

$$\tau_{form} = \tau_0 \frac{E}{m} \tag{1.13}$$

In the above equation E is the energy and m is the mass of the hadron. From the above equation we can infer that a high energy hadron has a long formation time, whereas a low momentum and heavy mass hadron has a shorter formation time and is potentially produced already in the deconfined matter.

Thus, measuring and studying the properties of heavy resonances will enable us to understand the important signatures of the produced QGP medium in particular chiral symmetry restoration. The interaction of these resonances with the QGP medium can modify various resonance properties and lead to effects such as mass shift and width broadening [68, 69]. RHIC has a shorter QGP formation

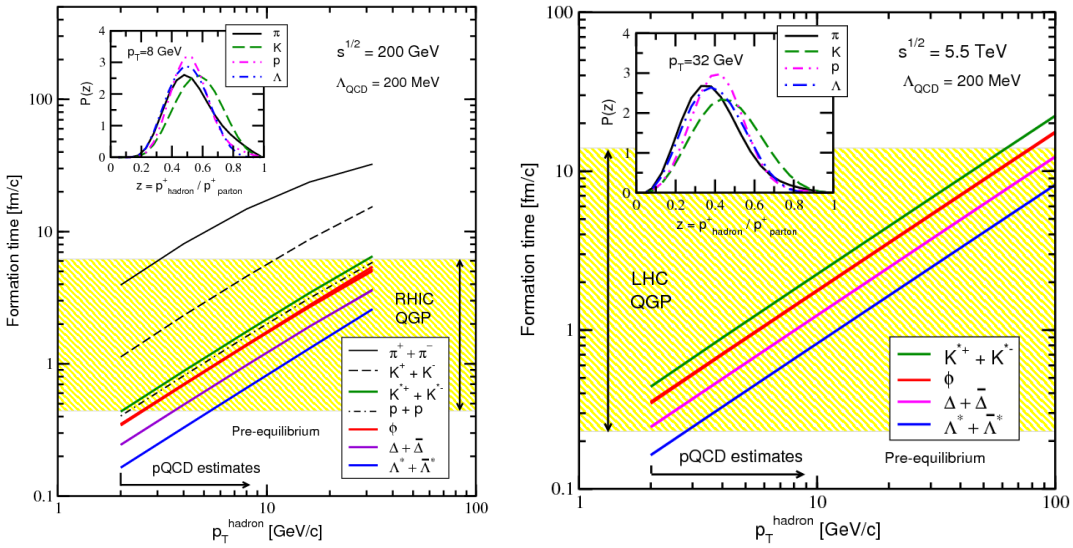

Figure 1.14: RHIC (left) and LHC (right) QGP formation time in different energy regimes.

time than the LHC,therefore these properties of heavy resonances can be better studied at LHC than RHIC, as shown in Figures 1.14.

1.6 Importance of proton proton collisions

Proton-Proton collisions served as the baseline for new physical signatures in relativistic heavy-ion physics. Scattering processes in pp collisions can be divided according to the kinematics of the scattered particles, namely the hard and soft processes. We use QCD as the underlying theory for both processes. For hard processes, such as W or high-p_T jet production, the governing physics can be well

understood using perturbative QCD. For soft processes, such as the total cross sections, diffractive processes or underling particle production, the rates and properties are dominated by non-perturbative QCD effects and they are much less understood. The overall event structure of a pp collision is shown in Figure 1.15.

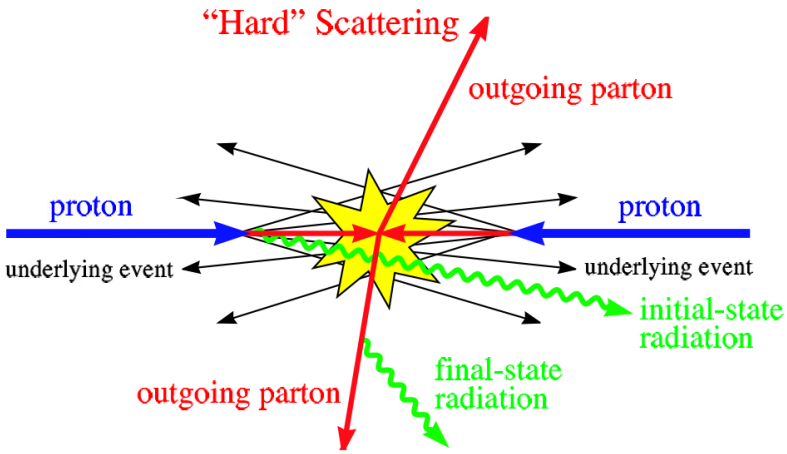

Figure 1.15: Typical pp collision event [70].

Except for the underlying event in the above figure all the other physical concepts can be well described by the pQCD calculations. This underlying event is an unavoidable background in pp collisions and better understanding of it would enhance the physics of hadron collisions and also it would help to fine tune Monte Carlo event generators. To get a proper understanding of pp collisions first we have to look into the substructure of the proton.

1.6.1 QCD factorization theorem

Hard and soft components can be separated and parameterized via the QCD factorization theorem [71, 72, 73]. The cross section for a given physics process can be described as a convolution of parton density (parton distribution function), hard scattering cross sections and final state fragmentation functions.

$$\frac{d\sigma_{pp}^{h}}{dyd^{2}p_{T}} = \sum_{abcd} \int dx_{a} dx_{b} f_{a}(x_{q}, Q^{2}) f_{b}(x_{b}, Q^{2}) \hat{\sigma}(ab \rightarrow cd) \frac{D_{h/c}^{0}}{\pi Z_{c}} \tag{1.14}$$

Here $f_a(x_q, Q^2)$ and $f_b(x_b, Q^2)$ are the parton distribution functions of two incoming protons. They provide how partons are distributed inside a proton and they can be extracted from fits to deep inelastic scattering data. $\hat{\sigma}(ab \rightarrow cd)$ is the only pertibative component, which can be calculated by using matrix elements, and $\frac{D_{h/c}^{0}}{\pi Z_{c}}$ is the fragmentation function or the probability of hadronizing the parton c in to a hadron h. Fragmentation functions are extracted from e^+e^- collisions [74].

1.6.2 Substructure of the proton

Even though the proton is composed of three valence quarks, gluons and sea quarks, the exact composition is still not well understood. The distribution of partons inside the proton depends on the Bjorken-x [75, 76], which is the fraction of the proton momentum carried by the parton and Q^2, the momentum scale that characterizes the hard scattering.

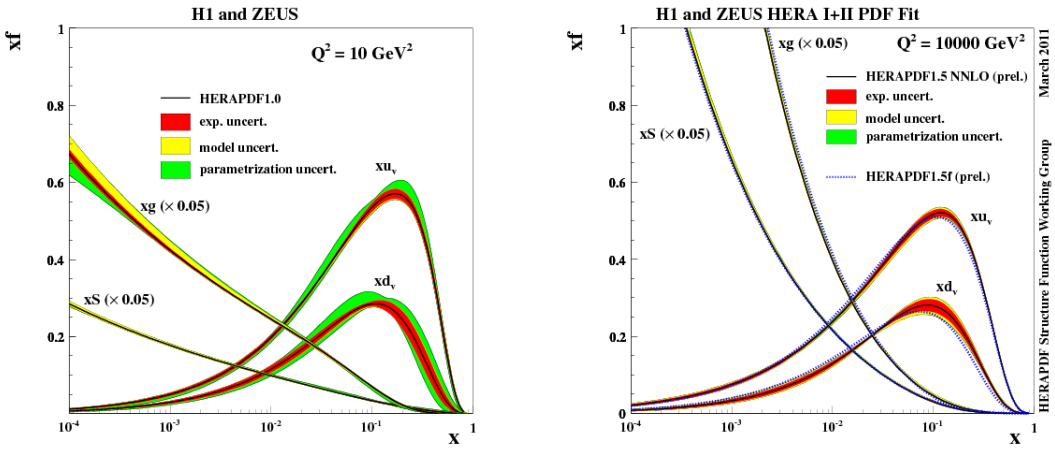

Figure 1.16: Parton distribution functions from HERAPDF at Q^2 = 10 GeV^2(left) and at Q^2 = 10000GeV^2(right) [77].

These quantities, x and Q^2, are also used to parameterize Parton Distribution Functions (PDF) [78, 79, 80], as seen in Figure 1.16. At lower energies, the valence quarks are dominant while at higher energies, the gluons and sea quarks are dominant. In Figure 1.16 subscript v stand for valence quarks and s stands for sea quarks. In both plots gluon and sea distributions are scaled down by a factor 20, which means the mean values of the distributions are higher than the valence quark distribution.

Chapter 2

CERN, the Large Hadron Collider and the ALICE detector

To the public, it is known as the “Big Bang Machine", for scientists it is known as the Large Hadron Collider (LHC), the world’s largest particle accelerator. The LHC is located at CERN, which has contributed to the field of science and technology in numerous ways, including several Nobel prize discoveries and the development of the World Wide Web. In this chapter I will briefly discuss the experimental accelerator facilities at CERN and outline their physics goals. I will detail the ALICE detector and its subsystems. The chapter will conclude with a description of the ALICE firmware, such as trigger systems and data acquisition and the ALICE software for data reconstruction, analysis and simulations.

2.1 CERN

CERN stands for the “Conseil Européen pour la Recherche Nucléaire", which is the french acronym for the world’s largest physics laboratory (European Council for Nuclear Research in English). Founded in 1954 and located at the border between Switzerland and France, it hosts more than 10000 physicists and engineers from nearly 100 countries all around the world who aim to unravel the mysteries of the universe [81]. The idea of establishing CERN came from several famous scientists from Europe such as Niels Bohr, Louis de Broglie and Edoardo Amaldi. CERN has two major experimental sites: the Meyrin site which is the main laboratory site and the Prevessin site. Both are shown in Figure 2.1. The CERN Control Centre and the entrance to the CERN’s second largest accelerator, the SPS, are located at Prevessin site, while the entrance to the LHC is located at Meyrin site.

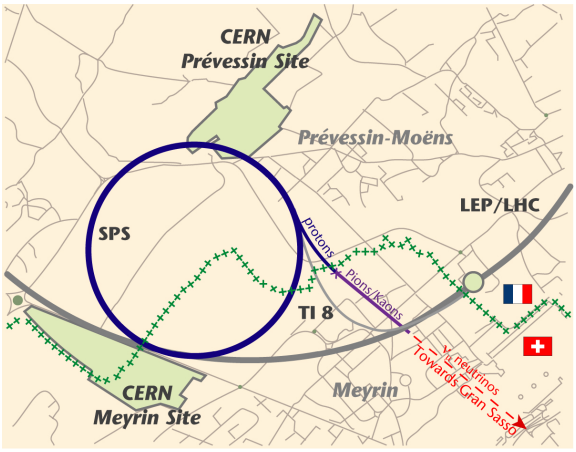

Figure 2.1: Map of the Meyrin and Prevessin sites relative to the SPS and LHC rings [82].

2.1.1 Scientific achievements

Several important discoveries in particle and nuclear physics have been achived by experiments at CERN. The most important are summarized in Table 2.1.

Year	achievements
1983	W and Z bosons discovered by UA1 and UA2 experiments. Led to the Nobel prize in Physics [83].
1989	Development of the World Wide web by Tim Berners-Lee and Robert Cailliau [84].
1992	Development of multi wire proportional chamber by Georges Charpak, which led to the Nobel prize in Physics [85].
2012	A boson with mass around 125 GeV/c^2 discovered by CMS and ATLAS experiments (Higgs boson), which led to the Nobel price in Physics [86, 87].

Table 2.1: Groundbreaking discoveries in science and technology that originated at CERN

2.1.2 The CERN accelerator complex prior to LHC

Today, CERN has five actively operating particle accelerators, linked together in the order of increasing energy of particle beams. They are capable of accelerating various ion beams to different energies. The Accelerators and Beam Physics department is responsible for beam alignment over the complete CERN accelerator facility from the sources to the highest energy accelerator. The Cern Control Center (CCC), operational since 2006, merged separate control rooms of the Laboratory's five accelerators into one. The main responsibility of the CCC is the operation of cryogenics and technical infrastructures.

2.1.2.1 Linear accelerator

CERN has two linear accelerators (Linacs): Linac 2 for protons and Linac 3 for Pb ions. Linac 2 is on the Alvarez Proton Linac, which has been operational from 1978. It provides pulsed 1 Hz beams of up to 175 mA at 50 MeV and uses a duoplasmaton ion source to provide H^+ ions [88]. These accelerators use Radio Frequency Cavities, based on alternating charged conducting plates. When the beam passes through these plates they provide a push and pull to the ions, which leads to acceleration. Linac 2 is the starting point of proton beams and directs them to the next stage of the accelerator chain. Linac 3 uses an Electron Cyclotron Resonance (ECR) ion source to provide heavy ions at 4.2 MeV for injection into the Low Energy Ion Ring (LEIR) [89, 90]. Figure 2.2 shows the schematic diagrams of the ion sources used in these liner accelerators.

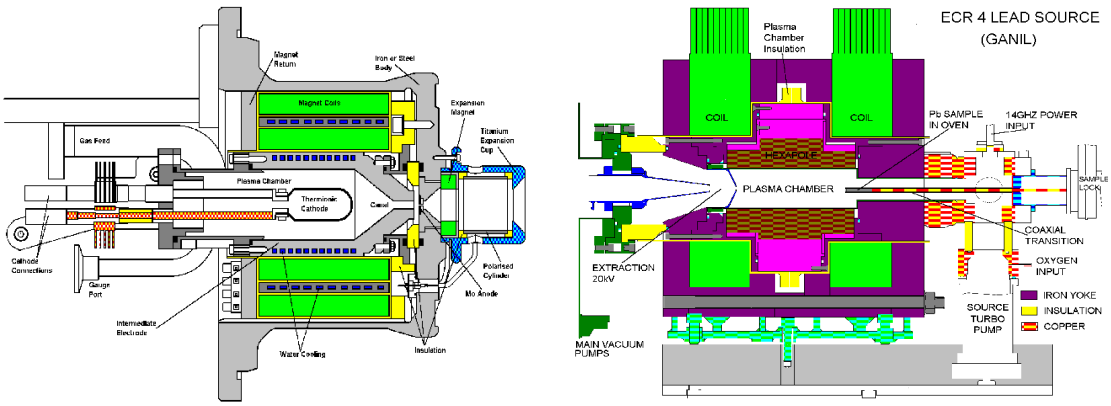

Figure 2.2: Duoplasmaton ion source (left) that provides H^+ ions and the ECR ion source (right) that provides heavy ions($^{208}_{53}Pb^+$) [91].

2.1.2.2 Proton Synchrotron Booster (PSB) and Low Energy Ion Ring (LEIR)

Both PSB and LEIR are intermediate accelerator rings used to increase the H^+ and $^{208}_{53}Pb^+$ energy. Linac 2 is linked to the PSB and proton beams gain energy from 50 MeV to 1.4 GeV. Linac 3 is linked to the LEIR where heavy-ion beams gain energy from 4.2 MeV to 72 MeV [92] .

2.1.2.3 Proton Synchrotron (PS)

The Proton Synchrotron was CERN's first synchrotron. The first proton beams were accelerated in 1959 to an energy of 25 GeV with a velocity of 99.93% the speed of light [93]. The ring has a circumference of 628 meters and has 277 conventional electromagnets operating at room temperature. Figure 2.3 shows the general layout of the PS complex.

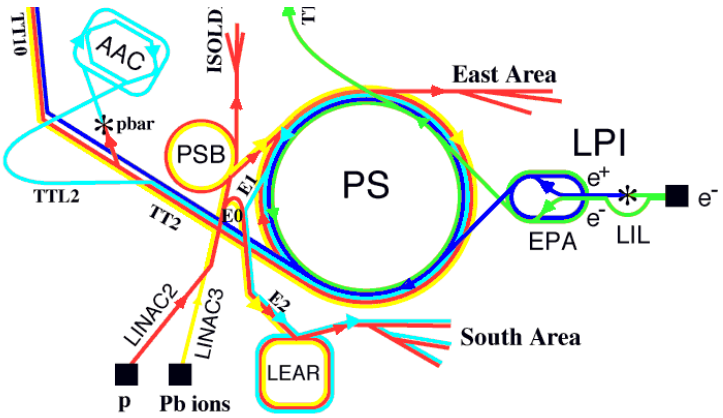

Figure 2.3: General layout of the PS complex

2.1.2.4 Super Proton Synchrotron (SPS)

The SPS was online in 1979. It is capable of accelerating protons to an energy of 450 GeV, and delivering them to three fixed target experiments. The ring has a diameter of nearly seven kilometers and consists of 1317 conventional electromagnets.

2.2 Large Hadron Collider (LHC)

The Large Hadron Collider (LHC) [94, 95, 96, 97, 98, 99] is a superconducting accelerator designed to accelerate beams of protons to record energies of 7 TeV

when operating at maximum power, leading to collisions at $\sqrt{s} = 14$ TeV; in heavy-ion mode the maximum energy for Pb ions is 2.76 TeV per nucleon, leading to collisions at $\sqrt{s_{NN}} = 5.5$ TeV. Over the past three years the LHC has been commissioned for operation in $\sqrt{s} = 7$ TeV, which is half the maximum energy, corresponding with 3.5 TeV per proton. The machine provides beam to the experiments for approximately 10^7 s / year for interactions with pp and 10^6 s / year for A+A systems. The LHC is a synchrotron for two counter rotating hadron beams. The main 26.7 km-long LHC tunnel was originally used by the Large Electron Positron collider. The main ring is divided into eight equal sectors in. In the midpoint of each octant is called a “Point". Each point can host experiments or be used to clean the beam, dump the beam or accelerate the beam, as shown in Figure 2.4.

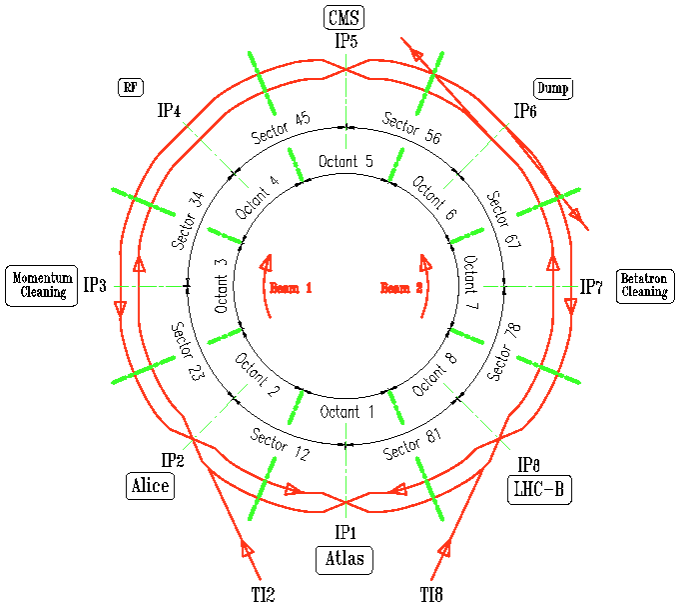

Figure 2.4: Layout of LHC and different activities in eight sectors [100].

At Points 1, 2, 5 and 8 beam pipes are allowed to intersect and here the four major experiments at the LHC are located. The LHC uses several types of cryogenic magnets to control and accelerate the beam [101]. The approximate length of an arc shown in Figure 2.4 is 2.8 km, filled with curved 15 m long superconducting dipole magnets for bending the beam along the track of the tunnel interspersed with superconducting quadrupole magnets to focus the beam. To achieve a 7 TeV beam the LHC needs a magnetic field of 8.3 T, which requires a cryogenic system that lowers the temperature to 1.9K using super fluid Helium [102]. At intersection points a given physics process with cross section σ is proportional to the event rate N with the proportionality constant is called Luminosity ($\mathcal{L}$), given by N=$\mathcal{L}\sigma$. So the higher $\mathcal{L}$, the higher the number of collisions at intersection points. The definition of $\mathcal{L}$ is:

$$\mathcal{L} = \frac{kN^2 f}{4\pi\sigma_x\sigma_y} \tag{2.1}$$

Where k is the number of bunches, N is the number of protons per bunch, f is the revolution frequency and σ_x, σ_y are the beam sizes at the collision points. To increase $\mathcal{L}$ we can increase k and N or decrease σ_x, σ_y. Therefore, at intersecting points the magnets can be used to focus the beam, causing higher $\mathcal{L}$ during the collisions, as shown in Figure 2.5.

The LHC has been running since 2010. In addition to the standard pp and Pb+Pb runs at nominal energy the collider also provides special runs. In 2010, for a short period of time it accelerated beams of protons to an energy of 2.76 TeV

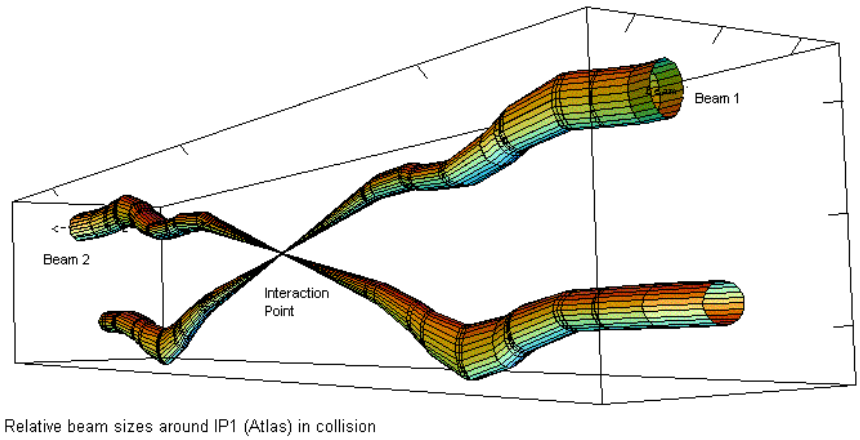

Figure 2.5: Relative size of the beam compared to the beam size at interaction point [103]

for direct comparison of results obtained in future Pb+Pb collisions. In 2012 it collided protons with Pb ions for a short period of time at 5.02 TeV. Figure 2.6 shows the integrated luminosities provided for each of the experiments in year 2011 for pp and Pb+Pb collisions.

2.2.1 pp collisions in LHC and physics goals

In each year of operation, the LHC will collide beams of protons (pp collisions) for eleven months. The main physics goal of the pp program is to observe the Higgs boson [105, 106, 107] and to search for physics beyond the Standard Model [108, 109, 110]. Observation of the Higgs boson requires both high energies as well as high luminosities [111]. The LHC is designed to meet these two requirements, operating at unprecedented energies and also at high luminosities.

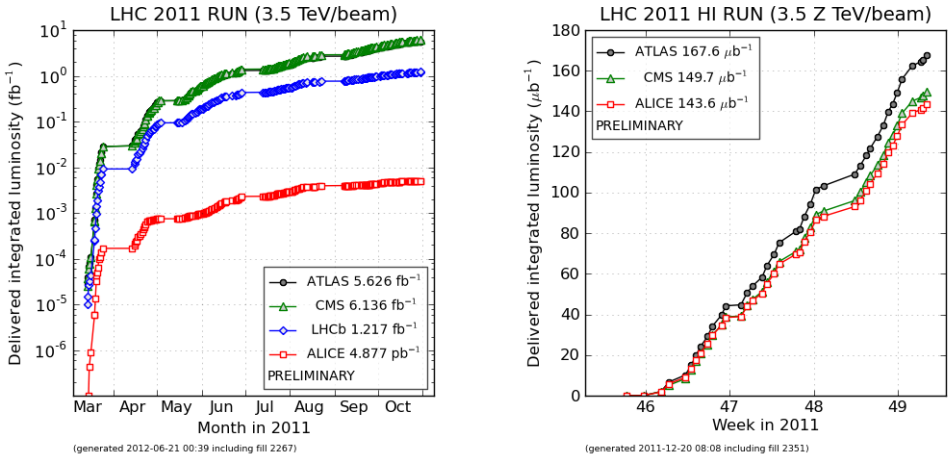

Figure 2.6: Luminosity delivered to each experiment in 2011, left panel shows pp luminosity and right panel shows heavy-ion luminosity. ALICE luminosity is less than that at ATLAS and CMS due to restrictions in readout electronics of the detector. The reduction in luminosity is achieved by defocusing the beam prior to the intersection point [104].

2.2.2 Pb+Pb collisions in LHC and physics goals

For one month a year the LHC accelerates lead nuclei. The main physics goal is the detection and characterization of the Quark Gluon Plasma, the phase of deconfined quarks which existed only microseconds after the Big Bang [112, 113], as detailed in section 1.4.

2.2.3 Experimental facilities at LHC

There are four major LHC experiments taking data since the commissioning in 2009. They are ATLAS, ALICE, CMS and LHCb. ATLAS (A Toroidal LHC Apparatus) is the largest of the experiments. Its main objective is the measurement of the Higgs boson. ATLAS is designed with an emphasis on jet measurements [114]. The Compact Muon Solenoid (CMS) shares many characteristics with ATLAS. Its main objective is also the measure of the Higgs boson and to search for physics beyond the standard model of particle physics. In terms of measurements, it focuses on muons and forward directions. The Large Hadron Collider beauty experiment (LHCb) focuses on the study of CP violation in B mesons. LHCb is capable of studying a large number of possible decay channels for these mesons, which requires excellent resolution for secondary decay vertices [115].

2.3 The ALICE Experiment

ALICE (A Large Ion Collider Experiment) [116, 117] was designed to improve the understanding of the theoretical foundation of high energy physics in pp and AA systems. ALICE is the only dedicated heavy-ion experiment at the LHC. Its detectors are designed to measure and identify hadrons, leptons and photons produced in the interaction region. To achieve the physics goals of the ALICE experiment it is necessary that particles with very low transverse momentum (typically 100 MeV/c) and particles with the highest transverse momentum (100 GeV/c) are well determined. To achieve this ALICE use all available particle detection methods

from RICH [1] to silicon detectors. Figure 2.7 is a schematic of the ALICE director showing all its subsystems.

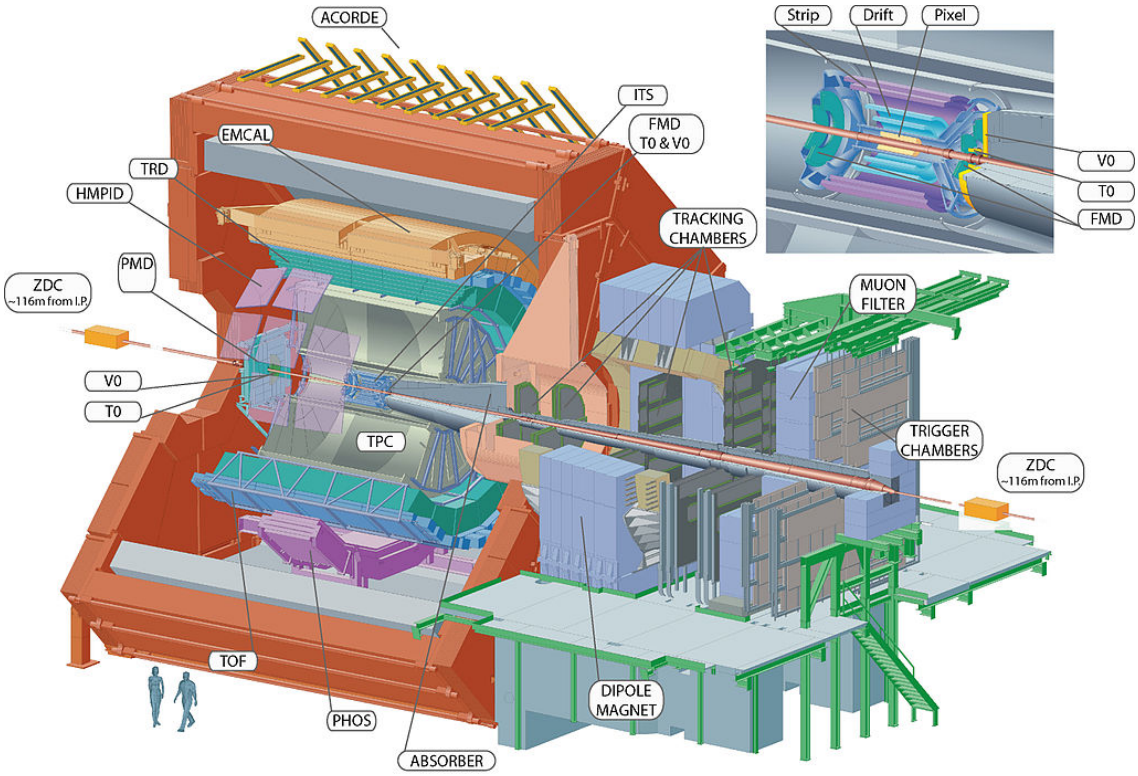

Figure 2.7: ALICE experiment and its 18 detector subsystems. On the top right is a zoomed view of the central tracking system. [118]

The reconstruction process of trajectories in ALICE works well even in a scenario of a maximum of 8000 particles produced in central Pb+Pb collisions. The detection of charged trajectories is performed using the tracking detectors around the Beryllium beam pipe. Identification of particles is done by combining the information of energy loss of the trajectory in various subsystems. First, the ionization energy loss is measured in the Silicon Detectors (ITS) and the gas volume

[1] Ring-Imaging Cherenkov

of the TPC, then the radiation in the TRD (Transition Radiation Detector) and HMPID (High Momentum Particle Detector) is measured. Finally the time traversed to reach the Time Of Flight detector (TOF) is determined. This information is also complemented with the detection of photons in the PHOS (Photon Spectrometer) and Electro Magnetic Calorimeter (EMCal). In the forward directions the detection of muons is performed by a spectrometer dedicated to just this task. In Figure 2.8 (left) the distribution of the detectors is shown as a function of pseudorapidity and Figure 2.8 (right) shows the particle identification range of each detector. All central detectors are embedded in a large solenoidal magnet with magnetic field of 0.5 T.

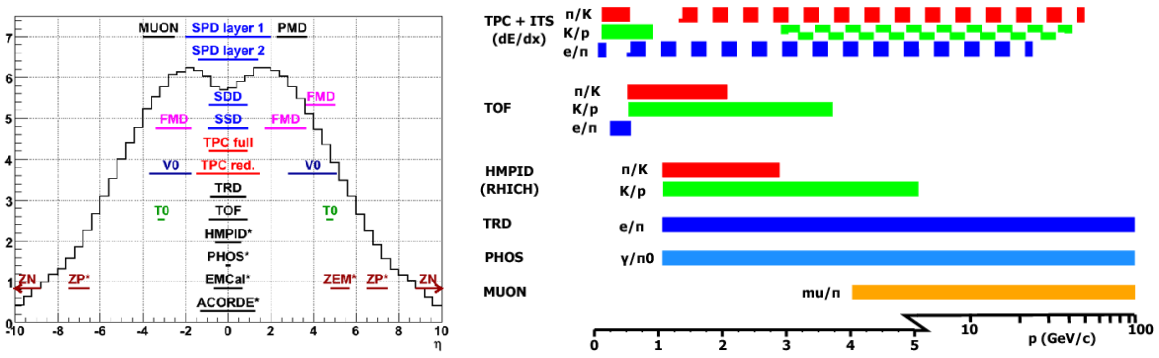

Figure 2.8: Detector acceptance and PID capability of each detector. The maximum possible η achieved by ALICE tracking detectors are restricted to -1.5 to 1.5, the only higher η PID detector is the μ arm.[119]

Besides these components, there is a set of detectors at large values of pseudorapidity to characterize the events and to act as triggers. These include the T0 and V0 detectors, as well as the FMD (Forward Multiplicity detector) that measures multiple charged particles. Finally, there is a dedicated detector to measure

photon multiplicity, located in a region of pseudorapidity between 2.3 < η <3.7, called the PMD (Photon Multiplicity Detector) and a Zero Degree Calorimeter (ZDC), another dedicated detector to measure spectator nuclei (not involved in the collision in the case of Pb+Pb collisions). In Figure 2.3 one can observe that ALICE records much less $\mathcal{L}$ compared with ATLAS and CMS. The main reason is that ALICE uses relatively slow drift detectors such as the TPC and parts of the ITS. At full $\mathcal{L}$ and interaction rate these detectors may be overloaded, therefore at the ALICE interaction point the beam $\mathcal{L}$ is artificially reduced to 10^{29} cm^{-2}s^{-1} from the maximum 10^{30} cm^{-2}s^{-1} that is delivered to ATLAS and CMS.

2.4 ALICE detectors

This section will briefly outline each of the detectors in ALICE used in this thesis, as well as their most important objectives. The other subsystems are not very relevant to the analysis, but are part of a versatile set of detectors capable of addressing a large number of physical problems. These detectors meet other needs and can be seen in more detail in Appendix C, with larger technical information contained in the ALICE Physics Performance Report [116].

2.4.1 Inner Tracking System (ITS)

The ITS consists of six layers of silicon detectors mounted on a cylindrical structure outward from the beam pipe, as one can see in Figure 2.9. These layers are

located with a radius between 4 and 43 cm from the axis of the beam, covering η=±0.9 for any particles that come from a region of interaction of ±5.3 cm along the beam direction in the center of the detectors. The maximum radius of 43 cm allows the ITS trajectories to be matched to trajectories of the TPC, which has an inner radius of 85 cm.

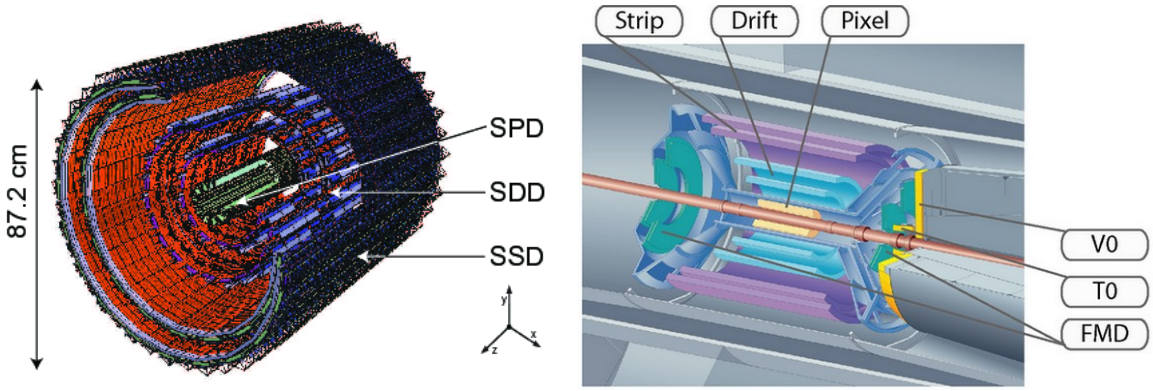

Figure 2.9: Schematic diagram of the ITS (left) and placement of ITS in central tracking region [120].

The main goals of the ITS are:

1. Determination of the primary vertex of interaction with better than 100 micron accuracy in x and y directions
2. Reconstruction of secondary vertices from decays of hyperons and D and B mesons
3. Reconstructing the trajectories of particles down to 200 MeV/c or less

The first two layers with a smaller radius are Silicon Pixel Detectors (SPD), each consists of about 107 silicon pixels. The intermediate layers are Silicon Drift

Detectors (SDD). Finally, there are two more layers that are Silicon Strip Detectors (SSD). The SPD detector has a fast readout time and therefore acts as a trigger detector by determining the instant time of the interaction.

2.4.2 Time Projection Chamber (TPC)

The TPC is the main tracking detector of ALICE. The primary technical challenge is that the detector must be able to handle interaction rates in Pb+Pb collisions of about 8 kHz, of which 10% are central collisions where the charged particles density per unit pseudorapidity can reach $dN_{ch}/d\eta$ = 8000, resulting in about 20,000 total charged particles within the TPC for a central event.

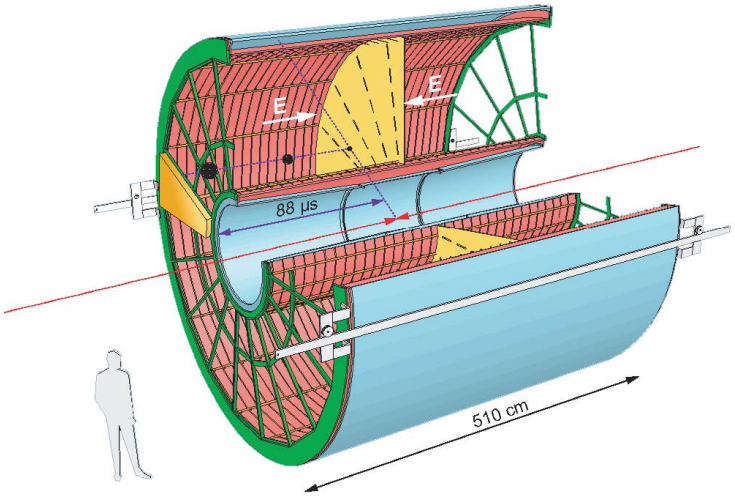

Figure 2.10: TPC and different components used in PID [121].

The TPC is composed of a cylindrical gas volume (barrel), divided into two half volumes of equal size, separated by a 30 μm thick high voltage electrode

to generate the drift field towards the end caps. The inner and outer radius of the TPC are 80 cm and 280 cm, respectively. The detector has an overall length of 500 cm along the beam direction, the main axis of the TPC is parallel to the beam pipe. End caps consist of with multi-wire proportional chambers (MWPC) with 18 trapezoidal pad readouts. When charged particles pass through the gas, their ionization produces free electrons and the drift electric field makes these electrons cross the chamber and deposits them at the end plates. The resulting electric current is readout by the readout pads.

2.4.2.1 Charged particle identification using TPC

The basic principle behind TPC particle tracking is the motion of a charged particle in a magnetic field. Radius of curvature by a charged particle in a magnetic field is given in r=p/qB, where p is the particle momentum, q is the charge of the particle, and B is the magnetic field perpendicular to the motion of particle. Charged particles will bend either clockwise or counterclockwise, depending on its charge. As explained in section 2.4.2, these charged particles ionize the gas and create free electrons, which drift towards the end caps by an electric field of 400 V/cm. The end caps consist of MWPCs that can read the x and y position of the drift electrons. The z position is usually measured along the beam axis and can be determined by the time it took the free electron to get to the end caps and the drift velocity of the TPC. To determine the particle species we measure how much energy a particle loses per unit length (dE/dx) as it travels through the TPC. The energy loss per unit length of a charged particle of charged Z and traveling with

a speed of β=v/c in a dense medium is given by Bethe-Bloch function [122]:

$$-\left\langle \frac{dE}{dx} \right\rangle = \frac{4\pi N e^4}{m_e c^2} \frac{Z^2}{\beta^2} \left\{ ln \frac{2 m_e c^2 \beta^2 \gamma^2}{I^2} - \beta^2 - \frac{\delta(\beta)}{2} \right\} \tag{2.2}$$

In the above equation $m_e c^2$ is the rest energy of the electron, N is the number density of electrons in the traversed matter, e is the elementary charge, I is the mean excitation energy of the atom and $\delta(\beta)$ is the density effect correction to ionization energy loss. Figure 2.11 shows the specific energy loss dE/dx vs momentum for tracks measured with the ALICE TPC. Here the x-axis is the rigidity, which

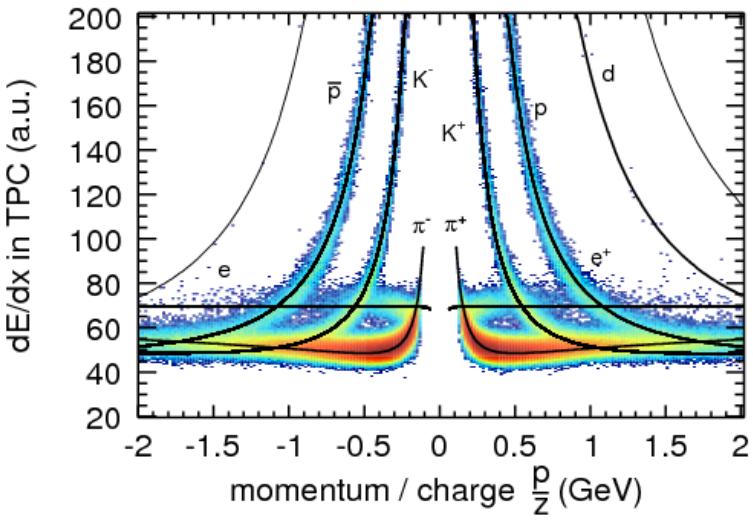

Figure 2.11: Specific energy loss dE/dx vs momentum for tracks measured with the ALICE TPC [123].

is the momentum over the charge. All of the particles here have a charge of ±1. Positively charged particles are on the right and negatively charged particles are on the left. At a given momentum, heavier particles lose more energy, thus in the

the y-axis mass of the particles increases. As one can see from the above figure, charged particles are not possible to identify beyond momentum ≈1 GeV/c.

2.4.3 V0 detector

The V0 detector [124] is a fast, versatile detector used characterize events. Its signals are used in different ways:

1. They generate a trigger signal that captures any minimum bias event
2. They are an indicator of centrality (ie the impact parameter) in heavy ion-collisions
3. They filter a large part of beam-gas events
4. They provide a fast wake-up signal for the TRD

The V0 detector consists of two sets of counters located on each side of the barrel tracking system (V0A and V0C). Each counter is segmented into 4 rings and each ring has 8 independent modules, as shown in Figure 2.12. The counters are read by WLS/clear fibers coupled to PMTs working inside the ALICE magnetic field. The V0A has a pseudorapidity coverage of 2.8< η < 5.1 and the V0C covers -1.7> η > -3.7.

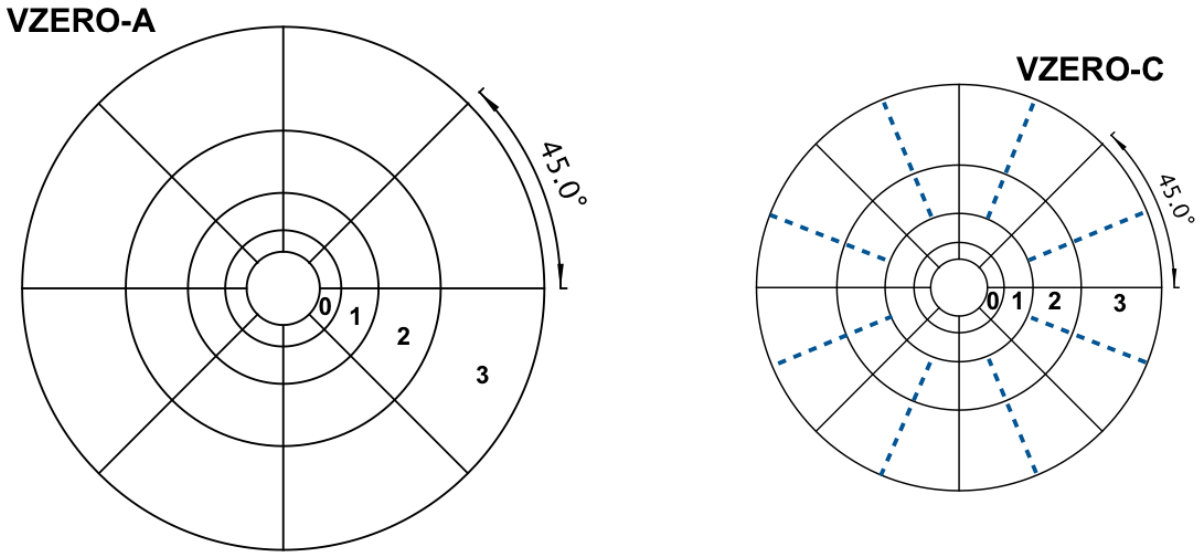

Figure 2.12: Sketches of VZERO-A and VZERO-C arrays showing their segmentation. Scintillator thicknesses are 2.5 and 2 cm, respectively [125].

2.5 ALICE trigger system

The trigger system of ALICE is constructed to select a variety of events, taking into account constraints imposed by the bandwidth of the data acquisition system (DAQ) and High Level Trigger (HLT) [126]. The challenge of the event selection is to deal with very different detectors regarding the electronic readout time and response time within each pp and Pb+Pb collision. The first level of the ALICE trigger must necessarily be fast, and is called the level zero trigger, or L0. This signal needs to be processed with a time latency of no more than 1.2μs after a collision, and only a few detectors are able to answer back that rapidly (SPD, V0, T0, Muon Spectrometer). A slower signal, processed in a maximum 6.5μs time latency, is called the level one trigger, or L1. The next level is delayed to 88μs to

avoid stacking interactions in the detector system (the level 2 trigger, L2). All of these levels, L0, L1 and L2 are processed in real time by electronics during data taking. The most complex and sophisticated trigger is the HLT, which consists of a group of processing computers that already perform a fast reconstruction of each of the events that passed the selection of the lower-level event triggers. The trigger signals are processed by the Central Trigger Processor (CTP) of ALICE [127].

2.6 ALICE Data Acquisition system (DAQ)

ALICE uses different beam conditions to characterize and investigate a variety of physics observables, and thus needs a distinct number of trigger classes to identify each collision event. The three most frequent trigger events in ALICE are central, semi-central and minimum- bias. The main purpose of the ALICE DAQ system is to communicate with the ALICE Trigger system and reject unwanted physics events, bridge HLT algorithms with useful physics events while data tacking and direct selected events (trigger events) to permanent data storages [128]. The other importance of the DAQ are that it can check the quality of the raw data produced using dedicated software packages and monitor the overall system performance. Detector Data Links (DDL) are high speed optical links used to interface detector readout electronics to the DAQ [129]. The receiver end of the DDL consists of a DAQ Readout Receiver Card (D-RORC)[130]. The support software to the D-RORC are provided by Local Data Concentrators (LDCs). One LDC controls several D-RORCs. The overall data and signal flow form a trigger signal to the

detectors and the associated information from the CTP. Detector signals (event fragments) are then injected to the DDLs and assembled into sub-events in the LDCs via D-RORCs. Then all D-RORCs from sub detectors send a busy signal to CTP and DAQ sends a signal to CTP requesting permission to enable or disable the most common triggers. Finally if a positive response from CTP to enable the trigger is received LDCs direct the sub-events to a farm of machines called Global Data Collectors (GDCs), where the whole events are built. The data flow and DAQ architecture overview is shown in Figure 2.13.

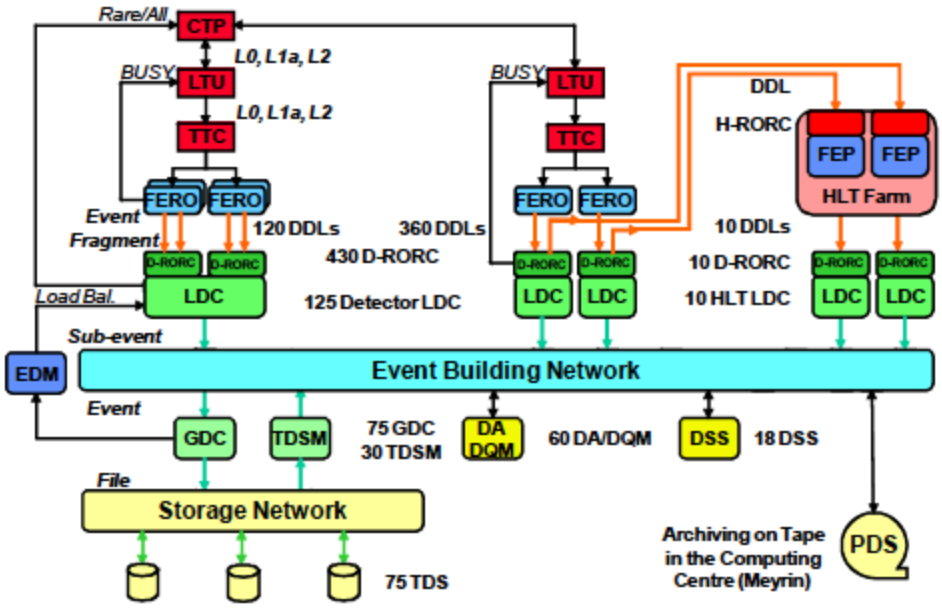

Figure 2.13: DAQ architecture overview

2.7 ALICE software framework

The ALICE software framework (offline project) provides the infrastructure for the development and operation of the data processing framework. The main tasks of AliRoot are simulation, reconstruction, calibration, alignment, visualization and analysis of data [131, 132, 133]. Two main parts of the software environment are the AliRoot framework and the ALICE computing grid. AliRoot is a object oriented data analysis package implemented via C++. It can be run on Linux and Apple OS-X operating systems with prior installation of ROOT and Geant 3. AliRoot provides an environment for the event generation, detector simulation, event and track reconstruction, data acquisition and complete data analysis. Codes for simulation and reconstruction from the different detectors are implemented separately. It can also perform detector simulations via different transport packages like GEANT 3, GEANT 4 [134, 135] and FLUKA [136] and can generate hadronic collisions via PYTHIA and HIJING. The ALICE computing grid is a world wide computer network that provides storage and analysis framework facilities for the data generated in ALICE [137]. The GRID points are organized according to the MONARC model, ranging on computing power from Tier 0 to Tier 2. Tier 0 is the largest and Tier 2 is the smallest computer centers [138]. The current ALICE grid has five Tier 0 and Tier 1 facilities and more than 80 Tier 2 facilities around the globe. The main user interface to the ALICE Grid is called the Alice Environment (AliEn) [139]. It provides data management, data transfer, AliRoot interface, analysis job submission and job monitoring through a single web interface.

Chapter 3

Data, event, track selection and analysis software development

This chapter will describe the data, event, track selections and analysis methods used in this thesis. The data selection section describes both real data and Monte Carlo data sets used, along with some naming conventions in ALICE. The event and track selection section describes how to obtain a reliable data sample for the final analysis. The concept of filter bits will be discussed here. The final part of this chapter deals with the analysis software development and data containers used in this thesis for a reliable systematic error estimation.

3.1 ALICE proton-proton data selection at $\sqrt{s} = 7$ TeV

The analysis is performed on four different data sets recorded by the ALICE detector back in 2010 at a center of mass energy of $\sqrt{s} = 7$ TeV. The ALICE naming convention for run year and period is LHCYYX, where YY stands for the last two digits of the year and X is for the period number where data was recorded. Each data period is incorporated with different run numbers and inside one run number there is a certain number of events in ESD and AOD format [140]. Depending on the analysis and the analysis software used, either an ESD or an AOD data format will be preferred. Furthermore each ESD and AOD has several filtering processes, such as calibration and reconstruction iterations, called passes that range from pass 1 to pass 3. ALICE has a data quality control group called the PWGPP (Physics Working Group of Physics Performance). If some problems are detected on a certain data set or a special data set is needed for a special analysis, they reconstruct the data set again and assign a number for the AOD, for example AOD086, AOD147. In this analysis I developed my own analysis software to run on the AOD format. Table 3.1 summarizes the data set specifications used in this analysis. All the necessary data information can be found in the ALICE Monalisa web interface.

3.2 ALICE Monte Carlo data selection at $\sqrt{s} = 7$ TeV

The Monte Carlo data used in ALICE can be divided into two levels.

Data set	Recording month	AOD Number	Pass	Number of events
LHC10b	April 2010	AOD 147	pass 2	25 Million
LHC10c	May 2010	AOD 147	pass 2	67 Million
LHC10d	June,July 2010	AOD 147	pass 2	107 Million
LHC10e	July, August 2010	AOD 147	pass 2	71 Million

Table 3.1: Overview of the ALICE data sets used in the data analysis at $\sqrt{s}$ = 7 TeV and the number of events per data set.

1. The generated level Monte Carlo is the out put of a certain event generator. This level generates particles with kinematics such as p_T, η, ϕ and certain other distributions for a given event. Each particle has an integer number associated with it for particle identification, which is called the PDG (Particle Data Group) value [141]. For example, the proton has a PDG value of 2212, the pion is 211 and anti-particles have the same magnitude but are negative. In this analysis we use PYTHIA 6 with the tune Perugia-0 (tune number 320) for particle generation. For Pb+Pb collisions the event generators used in ALICE are HIJING or AMPT [142]. Analysis done at this level is used to compare the corrected results with real data.

2. The reconstructed level Monte Carlo is the output of a complete detector simulation and reconstruction. In this type of simulation the generated level particles are propagated through the detector using a Monte Carlo transport code to reconstruct the primary vertex, tracks and detector hits. This

will allows physicists to get a good understanding of the detector performance. To simulate detector components and particle transport through certain detector elements, ALICE uses the Fortran based simulation package called GEANT3 [143]. During this simulation all the conditions present in real data tracking were maintained and final results were saved in ESD or AOD format for a particular anchor run. Here anchor run corresponding to the data set containing reconstructed real data, for example LHC10b or LHC10c. Each event generator has default tunes that the user can change accordingly until the results from real data and MC data comparable.

MC data set	Anchor run	Generator	Tune	Number of events
LHC10d1	LHC10b	Pythia 6	Perugia-0	25 Million
LHC10d4	LHC10c	Pythia 6	Perugia-0	61 Million
LHC10f6a	LHC10d	Pythia 6	Perugia-0	103 Million
LHC10e20	LHC10e	Pythia 6	Perugia-0	3 Million

Table 3.2: Overview of the MC data sets used in the data analysis at $\sqrt{s}$ = 7 TeV and the number of events per data set. All these MC events undergo the same event and track selection cuts that were used in the real data.

3.3 Event selection

For a solid physics analysis it is important to extract a clean sample of data out of the raw data recorded in the collisions. Certain unwanted events were rejected online via the ALICE trigger system that was explained in Chapter 2.5. This section explains further data cleaning using the offline trigger system and analysis event selection cuts.

3.3.1 Trigger selection

The first event selection of this analysis is done by accepting events that fulfill the ALICE minimum bias trigger [144]. This trigger requires a charged track detection in the Silicon Pixel Detector or a signal in the V0 detectors and signals from two beam-pick-up counters to ensure the existence of two proton-proton bunches during the trigger selection [145]. A signal in the beam-pick-up counters rejects unwanted background triggers from beam-gas events. This trigger allows us to select almost exclusively inelastic proton-proton collisions [146]. In addition to the online trigger, an offline event selection in AliROOT called AliPhysicsSelection, which reprocesses the trigger decision, was implemented in the analysis software. Figure 3.1 shows the charged particle multiplicity distribution before (left) and after (right) the minimum bias trigger selection. It should be noted that the abrupt bump before the trigger selection due to unwanted background signals is removed and a smooth distribution remains after the trigger selection.

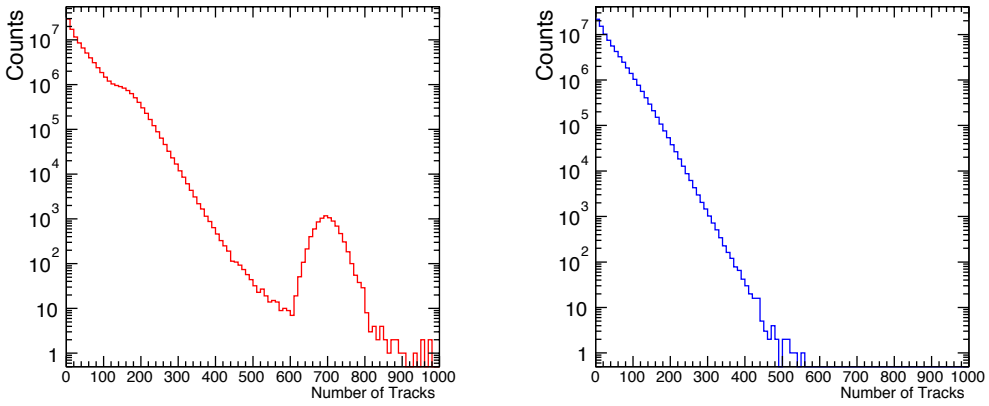

Figure 3.1: Multiplicity distribution before (left) and after (right) the minimum bias trigger selection.

In Monte Carlo data, the generated level analysis should come before and the reconstructed level analysis after the trigger selection to get a proper reconstruction efficiency denominator and numerator.

3.3.2 Primary vertex reconstruction

The second event restriction is based on the primary vertex selection in the longitudinal direction. ALICE primary vertex reconstruction undergoes several steps.

1. Estimation of the vertex position using SPD track-lets (SPD only Primary vertex).

2. Reconstruction of tracks in the TPC, from outside to inside (TPC only Primary vertex).

3. Extrapolation of TPC reconstructed tracks to ITS.

4. Track back-propagation to outermost ITS layer, TPC and outer detectors.

5. Re-fitting of reconstructed tracks inward.

6. Accurate vertex determination using fully reconstructed tracks (TPC+ITS Primary vertex).

The primary vertex reconstructed in this analysis is not just from TPC only tracks, but also from ITS or TPC+ITS tracks to ensure the best resolution for the primary vertex position. We restrict the primary vertex position within $|Z_{Vertex}|$ <10 cm with respect to the nominal interaction point. This ensures a better track uniformity in the ALICE TPC acceptance of -1< η <1. Once the primary vertex position cut is in place we are looking into some special events called Pileup Events, which are events with more than one proton-proton collision per bunch crossing. These events need to be removed before further analyzing data. In this analysis we used a predefined ALIROOT function called AliESDEvent::IsPileupFromSPD(). That will return a Boolean function if it detects any pileup event. The Boolean function can be used to reject that event from our analysis. The same procedure was followed for the Monte Carlo reconstructed primary vertex. Figure 3.2 shows the fully reconstructed primary vertex z position fitted with a Gaussian (left) and a comparison of MC reconstructed primary vertex with the real data reconstructed primary vertex (right).

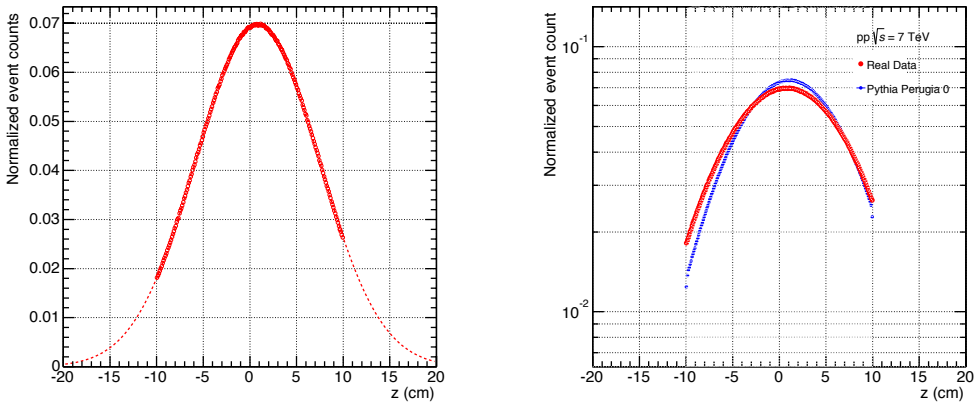

Figure 3.2: Primary vertex z position fitted with a Gaussian (left) and a comparison of MC and real data reconstructed primary vertex (right).

3.4 Charged track selection

Throughout this analysis we are using three types of reconstructed tracks. Charged primary tracks, charged leading tracks and neutral strange particle tracks. Reconstruction and detection of neutral strange particles will be discussed in detail in Chapter 4. Charged primary tracks are the charged particle trajectories, which are produced in the collision, and decay products, except the particles, which come from weak decays of strange hadrons. The charged leading track of the event is the highest p_T track of the event except if it is a daughter track of weak decays of strange hadrons. The restriction we apply for a charged particle should not be a decay daughter of strange hadrons in order to eliminate any short range $\Delta\eta, \Delta\phi$

correlations. This will be discussed in detail in Chapter 5. ALICE use a convention called filter bits to select certain attributes of reconstructed tracks. Filter bits range from 0 to 10. Table 3.3 illustrates the various filter bits and default track cuts used in this analysis for AOD147.

Bit	Cut	Method
Bit7 (128)	TPC only tracks	Min Number of TPC Clusters > 70 Tracks constrained to SPD vertex
Bit8 (768)	Hybrid tracks	Max DCA To Vertex xy < 2.4 Max DCA To Vertex z < 3.2 Set Max Chi2 TPC Constrained Global (36) Set Max Fraction Shared TPC Clusters (0.4) Set DCA To Vertex2D (kTRUE)

Table 3.3: Overview of the various filter bits and default track cuts used in this analysis.

In this analysis we use filter bit 768 as the default track cut and for any systematic study we also used filter bit 128. All charged particles were in the p_T range of 0.2 to 50 GeV/c.

3.4.1 Charged track quality analysis

Once the event cuts are placed in the data set we need to check the reconstructed tracks for their quality. This can be done by analyzing certain track distributions such as ϕ, η and p_T. Any deviations found in the η and ϕ distributions of charged tracks will alert us to a faulty or switched off detector element during the data taking. Events with such deviations are rejected from the final data sample. Figure 3.3 shows a ϕ distribution that was recorded while several TPC read-out sectors were corrupted.

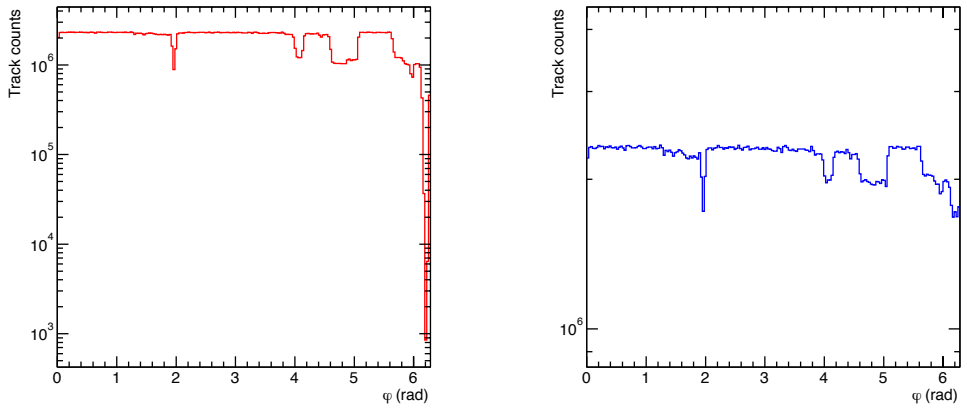

Figure 3.3: ϕ distributions caused due to malfunctioning TPC sectors.

For this analysis uniform ϕ and η distributions were required. Figure 3.4 shows these distributions for TPC only and Hybrid tracks.

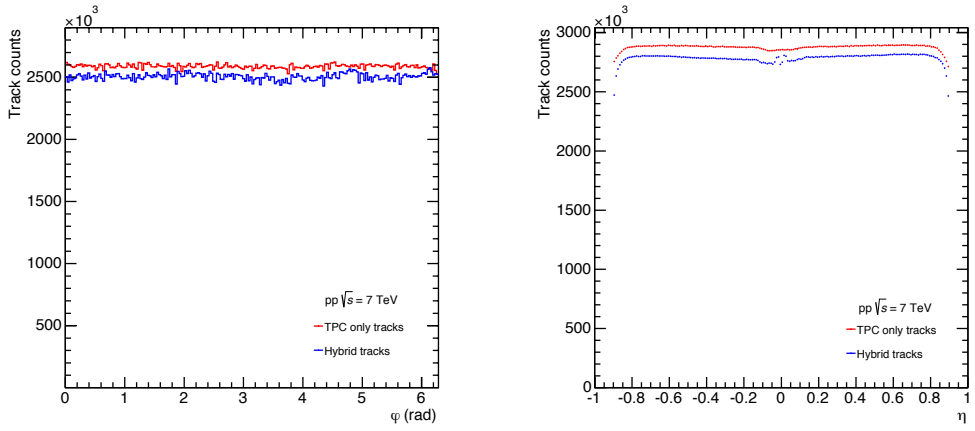

Figure 3.4: ϕ (left) and η (right) distribution of TPC only and Hybrid tracks.

More information on event selection and track quality analysis in pp collisions can be found in [147].

3.5 Analysis software development

One of the most challenging parts of a high energy physics analysis is the development of analysis software. The software development for this thesis was two fold. First we developed a code to do Quality Assurance (QA) on reconstructed charged tracks and tune the strange hadrons topological cuts. Continuous submission of jobs to the ALICE GRID is inefficient to tune topological cuts because each time we change a cut we need to submit jobs. Therefore I developed an object oriented C++ class that runs on top of Aliroot named AliV0TreeMaker.cxx

and AliV0TreeMaker.h. The sole purpose of this class is to make a highly filtered TTree root object out of existing AOD files [148]. The final TTree has 77 branches ranging from primary vertex position to Monte Carlo PDG values. The event structure was maintained by using simple float variables to event wise observables and Standard Template Library (STL) vectors for track wise observables, this allows one to do event by event physics analysis locally without submitting jobs to the GRID again [149].

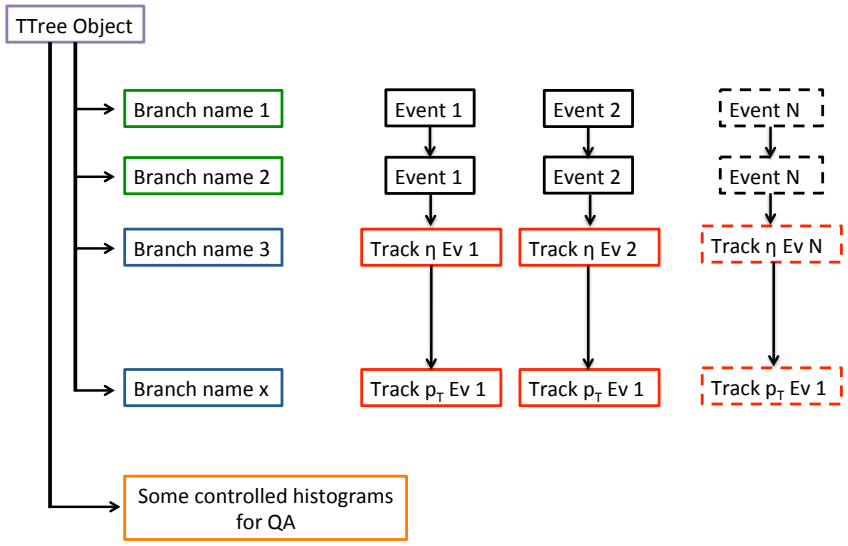

Figure 3.5: Branch flow of the final ROOT object analyzing in HPCC.

Figure 3.5 shows the hierarchy of branching configurations in the final ROOT file downloaded form GRID. Green boxes are the branches containing event information, such as primary vertex distributions or particle multiplicities. These branches support only simple float type variables. The blue boxes are the special

branches supporting STL vectors, for example, Branch name 3 holds the η distributions of events 1 to N. A red box corresponds to one STL vector, so if one needs to get η distributions of all events one should loop through events 1 to N and for each event open the vector to get the track information. The main reason to use vectors as data containers is to do event mixing, which requires event-by-event track information to build a special type of event buffer. Figure 3.6 and 3.7 shows the event wise and track wise information stored in the final TTree object. Once all data files were downloaded and merged the final root file was more than 500 GB.

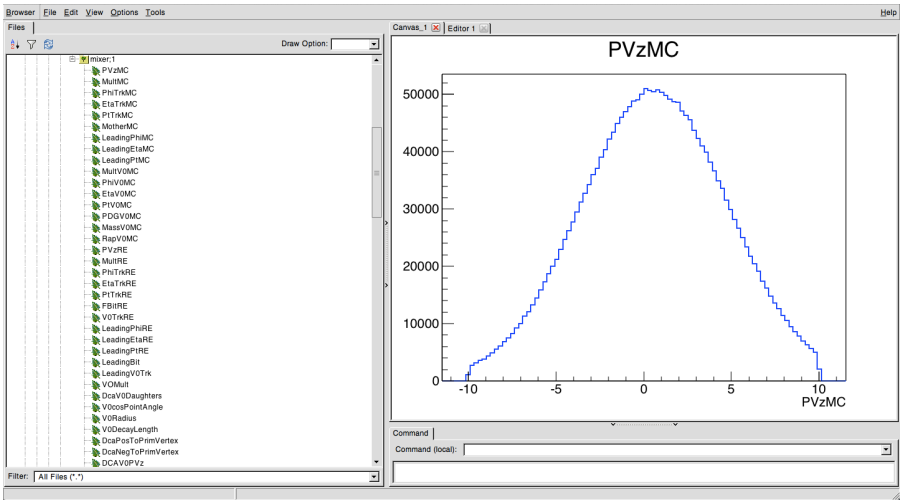

Figure 3.6: Event vise distributions such as primary vertex z position can be stored in the final TTree object.

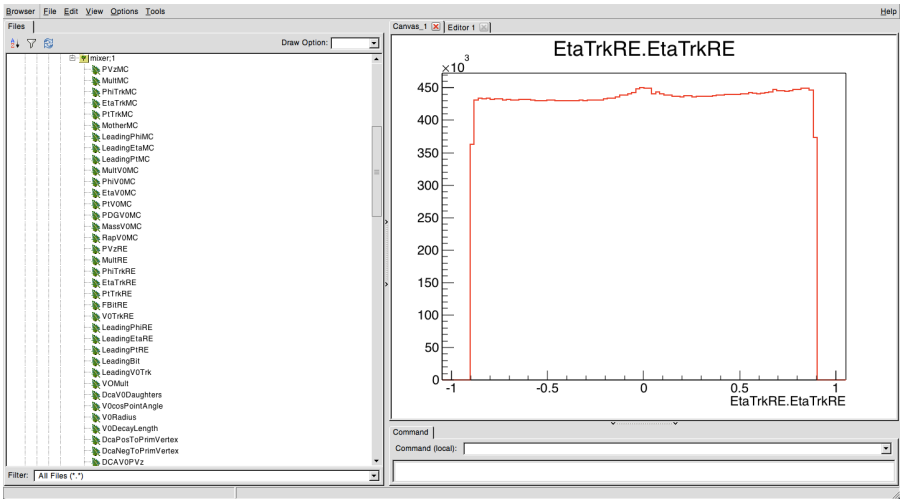

Figure 3.7: Track vise distributions such as η also can be stored in the same TTree object.

The second and final analysis took place on a High Performance Computing Cluster (HPCC) at the Center for Advanced Computing and Data Systems at the University of Houston. For this purpose the 500 GB final root file was chunked into several smaller 500 MB root files and stored in a local storage at HPCC. To read and plot required distributions out of a TTree object another C++ class named AliV0Module.cxx and AliV0Module.h, now run on top of ROOT, was implemented. All small root files were analyzed in parallel by dispatching several thousand jobs via HPCC. One of the biggest advantages of this type of local analysis is the efficiency, as well as the accuracy, of the systematic error calculation increases.

Chapter 4

Neutral strange particle reconstruction

Measuring hadrons that contain strange quarks is of interest since the original hadrons in the collision do not contain strange quarks among their valence quarks. Even though there are strange quarks in the quark sea of colliding hadrons the amount is very low compared with the strange quarks produced at LHC energies [150, 151]. Therefore strange quarks are virtually all produced during the collision and carry useful information about particle production mechanisms in pp and Pb+Pb collisions. Moreover, the fact that the strange quark mass is close to the critical temperature where the transition to the QGP (as seen in Figure 1.6) is expected allows us to study mass specific hadronization mechanisms [152]. The specific mass of the strange quark, which is systematically lower than the heavy quark masses means that the energy required for creating a $s\bar{s}$ pair is less than

that required to create heavier quarks, ensuring that the strange quark is the most abundant of the heavy species. Strange hadrons produced in high energy collisions can be divided into two parts, namely singly strange and multi strange hadrons. Singly strange hadrons carry a single s quark or anti s quark while multi strange hadrons carry more than one s or anti s quark. Moreover strange hadrons are available in both charged and neutral versions. The main focus of this thesis is to investigate production mechanisms of neutral strange hadrons such as K^0_S, Λ and $\bar{\Lambda}$. This chapter describes the reconstruction and detection of neutral strange particles in proton-proton collisions at 7 TeV. Various topological cuts and kinematic cuts will be introduced in this chapter. Signal extraction and reconstruction efficiency determination from Monte Carlo simulations will be described in the later part of this section.

4.1 Measuring the strangeness

Since neutral strange hadrons do not generate any tracks in the TPC they can only be reconstructed from their charged daughter particles. The following table shows the various types of strange hadrons and their decay channels. One strange hadron may have more than one decay channel, only the highest probability channel is mentioned. This probability of a strange hadron to decay in to a given set of daughter particles is known as its branching ratio (BR).

The decay of the particles listed in the table occurs after a characteristic time τ in the rest frame of the particle. This is usually not specified in units of time,

Hadron	$c\tau(cm)$	Mass (MeV/c^2)	Quark content	BR (%)	Decay channel
K^0_S	2.68	497.61	$\frac{1}{\sqrt{2}}(d\bar{s}-s\bar{d})$	69.2	π^++π^-
Λ	7.89	1115.68	uds	63.9	p+π^-
$\bar{\Lambda}$	7.89	1115.68	$\bar{u}\bar{d}\bar{s}$	63.9	π^++$\bar{p}$
Ξ^-	4.91	1321.71	dss	99.9	Λ+π^-
$\bar{\Xi}^+$	4.91	1321.71	$\bar{d}\bar{s}\bar{s}$	99.9	π^++$\bar{\Lambda}$
Ω^-	2.46	1672.45	sss	67.8	Λ+k^-
$\bar{\Omega}^+$	2.46	1672.45	$\bar{s}\bar{s}\bar{s}$	67.8	Λ+k^+

Table 4.1: Summary of most abundant strange hadrons and their properties.

but in distance units by multiplying by the speed of light c. In the lab frame, this is the distance traversed by a particle prior to decay. When we study the production of particles in high energy collisions we subdivide them into two categories: primary and secondary particles. Primary particles are produced directly in the hadron-hadron interaction most likely by quark fragmentation, in addition there are secondary particles that are produced as a result of the decay of primary particles. The strange hadrons studied in this analysis can be derived not only from the quark fragmentation, but also from other multi strange particle decays. For example, a Λ hadron may be produced by the decay of Ξ^0, Ξ^-, and the decay of Σ^0. In ALICE, the convention is that primary particles are all those originated in the primary hadron-hadron interaction and products of strong decays (resonances) whereas the secondary particles are weak decay products or products of

the interaction of primary particles with the material of the detector. Strong decays occur very close to the primary vertex. This is the case for example for the Σ^0 that decays in 10^{-20} s. In this brief interval, the particle traversed a distance far below the spatial resolution of the detector and is therefore still located practically within the interaction vertex. Thus, it is impossible to determine, in the laboratory frame, if a particle is a product of a strong decay or really a product of the initial collision. This is not the case for weak decays of strange hadrons, which typically occur in 10^{-8} to 10^{-9} s and therefore the particles travel a considerable distance in the laboratory before decaying into two daughter particles. This allows us to separate the decay vertex from the primary vertex of interaction.

4.2 Introduction to strange Hadrons

The strange hadrons studied in this thesis are the K_0^S meson and the Λ baryon and its corresponding antiparticle $\bar{\Lambda}$. They have weak decay topologies and are reconstructed through the detection in the decay channels given in Table 4.1. They decay into two charged particles in a decay topology called V^0; V is due to the shape of the decay trajectories that are always oppositely charged and bend in different directions in the magnetic field, and zero denotes the net total charge of the decaying particle. As mentioned in the previous section these strange hadrons decay weakly and we can distinguish the primary and secondary vertices. This allows us to identify the secondary tracks of all these weak decays and exclude then from primary particles. Once we have detected such secondary trajectories in an

event, it is necessary to combine the charged decay particles in pairs to obtain potential V^0s, which we call candidates. Then we use the concept of invariant mass to characterize potential V^0 candidate clusters (Eq 4.1).

$$M_{V^0}^2 = (E_1 + E_2)^2 - (\overrightarrow{p}_1 + \overrightarrow{p}_2)^2 \tag{4.1}$$

Here the subscripts are for the daughter particles. E is the energy and p is the momentum. If we replace daughter particle 1 and 2 with negative and positive tracks the above equation becomes:

$$M_{V^0}^2 = (E_{pos} + E_{neg})^2 - (\overrightarrow{p}_{pos} + \overrightarrow{p}_{neg})^2 \tag{4.2}$$

Expanding the energy term via relativistic kinematics gives:

$$M_{V^0}^2 = (\sqrt{m_{pos} + \overrightarrow{p}_{pos}} + \sqrt{m_{neg} + \overrightarrow{p}_{neg}})^2 - (\overrightarrow{p}_{pos} + \overrightarrow{p}_{neg})^2 \tag{4.3}$$

The mass term in above equation is used assuming a hypotheses consistent with the decays listed in Table 4.1, for example in the case Λ the path that correspond with the positively charged particle should be of a particle whose mass is the proton and the other path should be corresponding to a negative charge particle whose mass is the π^-. So the final equation for Λ is given in Eq 4.4.

$$M_{\Lambda}^2 = (\sqrt{m_p + \overrightarrow{p}_{pos}} + \sqrt{m_{\pi^-} + \overrightarrow{p}_{neg}})^2 - (\overrightarrow{p}_{pos} + \overrightarrow{p}_{neg})^2 \tag{4.4}$$

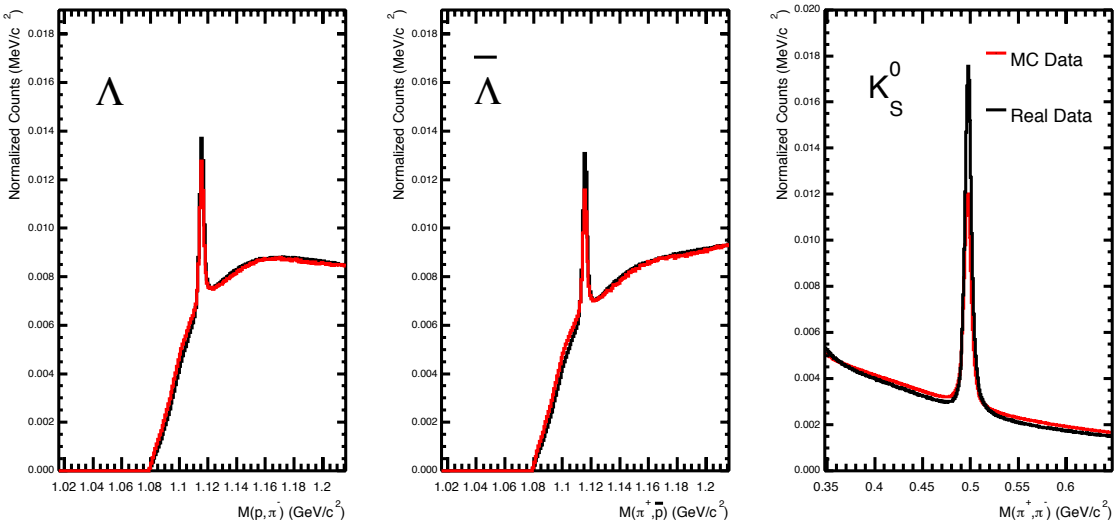

Figure 4.1: Neutral Λ, $\bar{\Lambda}$ and K^0_S invariant mass distributions for real data (black) and Monte Carlo data (red). Note that mass peaks are visible in all three distributions at 1.115 GeV/c^2 and 0.4976 GeV/c^2, corresponding with the mass of the Λ, $\bar{\Lambda}$ and K^0_S, respectively.

Figure 4.1 shows the invariant mass distribution for all three V^0 hadrons. The peak corresponds to the mass of the V^0 particle. Once we obtain the candidates we use a nominal set of cuts for particular daughter tracks to reduce background, as explained in the next section.

4.2.1 Topological selection of candidates

If we combine any two tracks with the appropriate mass hypothesis in a given event, we have a huge amount of V^0s as potential candidates. To reduce the combinatorial background due to misidentified V^0s we define a set of minimum topological cuts on two daughter tracks. These geometric cuts are selected with certain criteria that make it more likely that the tracks originate from a decay of a V^0. In particular, it is important to reject particles coming from the primary vertex, since we know that the decay topologies we study require that the trajectories come from secondary vertices. In this analysis we use five topological cuts, as described in Figure 4.2. The first cut is the distance of closest approach (DCA) of two daughter tracks. The two paths must be very close to the secondary vertex, presumably at the V^0 decay time. We are also looking for two tracks that do not originated from the primary vertex in order to reject primary particles. Thus, it is desirable that the DCA of each daughter track to the primary vertex (variables 2 and 3 in Figure 4.2) is larger than the resolution of the primary vertex. We also reject V^0s whose decay point is very close to the primary vertex (variable 4). Finally, the cosine of the steering angle of the V^0 (variable 5 in Figure 4.2) has to be close to one, which causes the V^0 to have a position vector and time vector aligned along the decay axis. Thus ensures that the possible V^0 came from the direction of primary vertex. The minimum topological cuts were determined previously during the development of the official ALICE software for V^0 reconstruction using secondary decays.

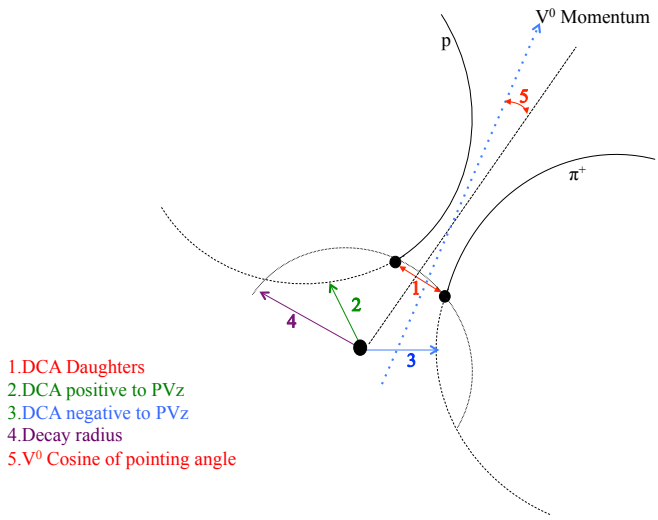

Figure 4.2: Conventional decay topology of a V^0 particle.

The minimum cuts can be summarized as follows (parameter number is associated with the labels in Figure 4.2):

1. DCA between daughter tracks should be less than 1 σ (parameter 1).

2. Minimum impact parameter for the daughter tracks at the primary vertex is 0.02 cm (parameters 2 and 3).

3. Minimum decay radius (radius of fiducial volume) of 1 cm and a maximum decay radius of 100 cm to ensure that the decay does not occur beyond the inner radius of the TPC to ensure detectability (parameter 4).

4. Minimum allowable value of the cosine of pointing angle is 0.95 to ensure that the V^0 comes from the direction of primary vertex (parameter 5).

With these topological cuts it is possible to observe low background invariant mass distributions in Figure 4.3, which show the expected peak positions around 1.1156 GeV/c^2 for Λ and $\bar{\Lambda}$ and 0.4976 GeV/c^2 for K^0_S. Even though we measure the invariant mass distributions with the expected mass peaks, they exhibit combinatorial background outside the peak area. Table 4.2 shows the nominal topological cuts used in this analysis.

Topological cut	Value
DCA between daughter tracks	< 1 (σ)
DCA between daughter tracks and primary vertex	> 0.06 (cm)
Minimum decay radius	> 0.5 (cm)
Cosine of pointing angle K^0_S (Λ, $\bar{\Lambda}$)	> 0.997 (0.995)

Table 4.2: Overview of the selection cuts used based on the decay topology of V^0.

In oder to further reduce the background more cuts need to be tuned. The distributions and systematic selection of the optimized topological cuts will be discussed in more details in Chapter 6.1. Other than the above cuts we used a few quality cuts for each daughter track:

1. Each daughter track must be well within $|\eta|$ <0.9 to ensure that the trajectories are inside the central region of TPC where the detection efficiency is approximately constant for different η.

2. Each daughter track in a V^0 pair must have opposite charge.

3. The quality of the charged track reconstruction in the TPC is determined by how many clusters a track is composed of. Each daughter track must contains at least 70 clusters.

4. To ensure a more reliable daughter track another cut was introduced, which is the "Ratio of TPC Crossed Rows to Findable Clusters". This is the ratio of the number of TPC pad rows actually crossed by the track to the number of clusters that could be found. The main purpose of this cut is to reduce the 'detector health' dependence of track reconstruction. In this analysis we use a minimum cut of 0.8.

ALICE developed two tracking strategies for V^0 reconstruction.

1. On-the-fly V^0 finder:
   (a) Works during tracking.
   (b) Check the likelihood of having a V^0 while adding cluster to the tracks.
2. Off-line V^0 finder:
   (a) Use after full tracking.
   (b) Selection of secondary tracks depending on their DCA to primary vertex.
   (c) Association of two opposite charged secondary tracks + topological cuts.

In this analysis we used Off-line V^0 reconstruction only. The following Figure 4.3 shows the comparison of V^0s before and after applying the topological selections.

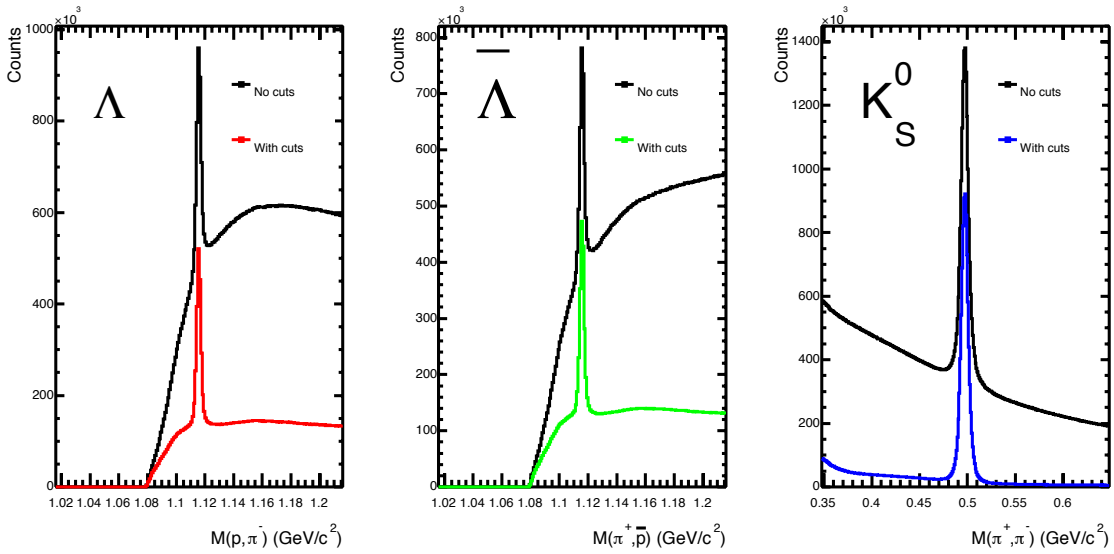

Figure 4.3: Impact of placing the topological cuts on each candidate. Note that the combinatorial background is strongly reduced after these selection cuts.

4.2.2 Particle identification of charged daughter tracks using energy loss in TPC

As described in Chapter 2.4.2, ALICE is able to identify some particles by measuring the amount of energy deposited in the TPC. Since this energy loss is depends on the particle type we can remove misidentified daughter tracks in a given V^0 decay channel. For example we demand the TPC to select π^+ and π^- as daughter particles in the case of K^0_S and $p(\bar{p})$, $\pi^-(\pi^+)$ in the case of $\Lambda(\bar{\Lambda})$. The effect of

applying this selection cut is shown in Figure 4.4.

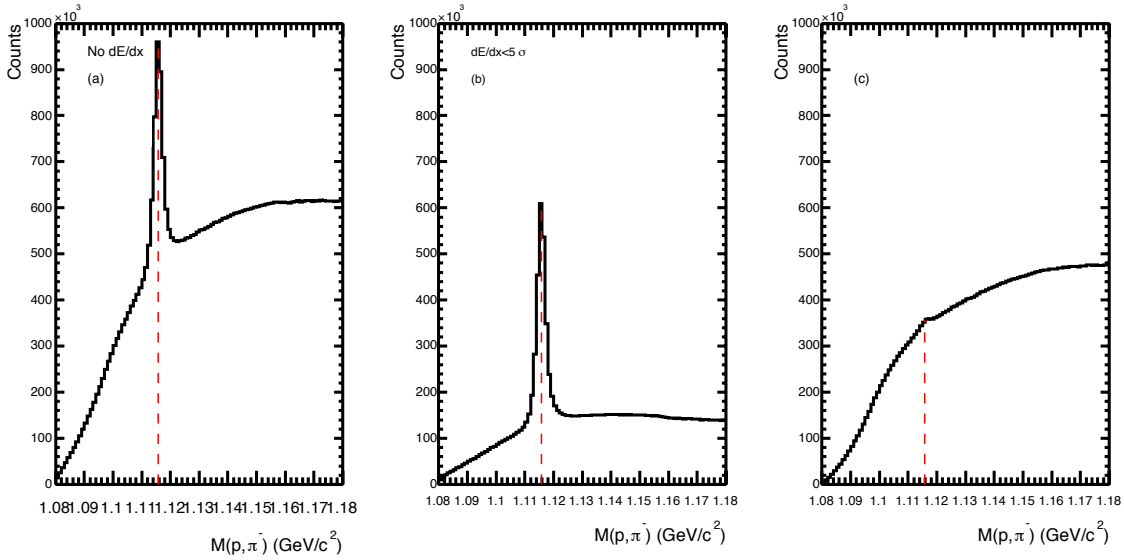

Figure 4.4: Result of placing the dE/dx cut on daughter tracks of Λ. The red dashed line represent the mass peak. After placing the cut (b) the rejected background (c) has no mass peak, which shows the importance of using the dE/dx selection.

In the above Figure 4.4 (a) the mass peak in the region (1.1157 GeV/c^2) is clearly visible and denoted by the red dashed line, but there is a very substantial combinatorial background beside and under the peak. In Figure 4.4 (b), we see that a large portion of this combinatorial background is removed by demanding the two trajectories of the daughter particles of a Λ mother particle deposited energy in the TPC corresponding with the particle species of the desired type, in

this case, proton for positive and π^- for the negative particle. The most important point to observe is that no significant portion of the signal is removed which can be seen in Figure 4.4 (c), where the invariant mass distribution of the rejected candidates shows no mass peak in the signal region. This selection cut is particularly important because it drastically reduces the asymmetry of the background noise on both sides of the invariant mass peak which in turn stabilizes the signal extraction process described later in the section 4.4.1. However, there is still a residual asymmetry between the background noise on each side of the invariant mass peak. The next selection criteria will be very important to resolve this residual asymmetry.

4.2.3 Selection cut based on proper lifetime of V^0

An additional selection cut applied to study V^0 is the selection by $c\tau$, which is the decay length in the particles rest frame. Here τ is the proper decay time in particles rest frame. For the strange hadrons in this study measured values of the $c\tau$ are given in Table 4.1. In the transverse plane for a particle of mass m with momentum p_T and a decay length r and a decay time t_r, τ can be written in the laboratory frame as:

$$\tau = m\frac{r}{p_T} \tag{4.5}$$

To get the dimension of the decay length we multiply τ by the speed of light. Since the probability of decaying a V^0 in $t_r >> \tau$ is quite low, it is interesting to consider an upper limit value for t_r. This will exclude particles with decay vertices so far

from the primary vertex that there is a high probability that this is a non-primary candidate. The limits considered for Λ and $\bar{\Lambda}$ are $ct_r < 30$ cm ($4\ c\tau$) and for K^0_S $ct_r < 40$ cm ($7\ c\tau$). Another important contribution from this cut is the rejection of secondary candidates arising from interactions with the material of the detectors, since these interactions typically occur at relatively small distances near the geometric center of ALICE. Figure 4.5 shows the effect of the $c\tau$ cut in the analysis. Figure 4.5 (a) shows the invariant mass peak for Λ without a $c\tau$ cut, as we can see the combinatorial background is clearly visible around the peak. Figure 4.5 (b) shows the effect of demanding a $ct_r < 30$ cm selection cut, which considerably reduces the combinatorial background. On the other hand 4.5 (c) shows the effect of having a cut of $ct_r > 30$ cm, which corresponds with the removal of some combinatorial background as well as a complete loss of the signal peak.

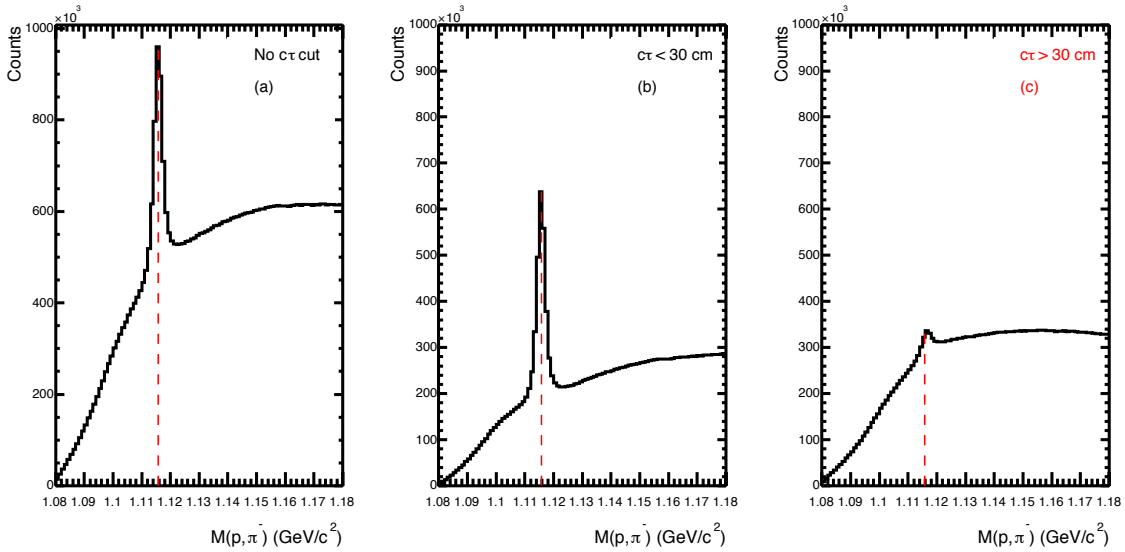

Figure 4.5: Comparison of invariant mass peak distributions without a $c\tau$ cut (a), with a $c\tau$ cut ($ct_r < 30$ cm) (b) and with the wrong selection (c) of the $c\tau$ cut ($ct_r > 30$ cm).

4.2.4 Rejection of V^0 candidates with the same decay topology

When we reconstruct V^0 hadrons from their decay daughters there is a possibility of identifying two different V^0 with the same decay topology. An additional selection criterion was introduced to reject strangeness decays with the same topology and with invariant masses consistent with other particles. The issue is illustrated in Figure 4.6. The blue and red dashed lines represent the Λ and K^0_S mass peaks, respectively. It is important to note the presence of the blue line underneath the red K^0_S mass peak (Λ contamination of K^0_S) and the red line underneath the blue

Λ mass peak (K^0_S contamination of Λ). Since we use different topological cuts on Λ, $\bar{\Lambda}$ and K^0_S, any Λ contamination cannot be completely removed by changing the topological cuts of K^0_S and vise versa.

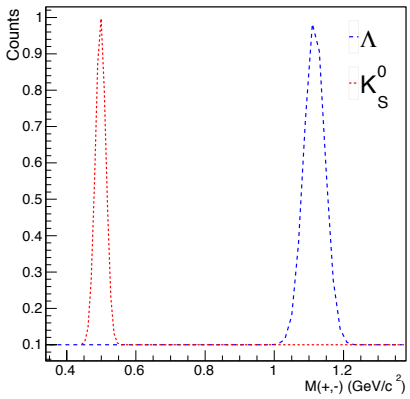

Figure 4.6: Effect of overlapping two invariant mass distributions due to competing candidates.

To remove this contamination we demand the following condition for each candidate.

1. For Λ and $\bar{\Lambda}$ candidates we reject a V^0 mass window with the mass hypothesis of K^0_S with the condition $|M(\pi^+,\pi^-)$ - 496.7 MeV/$c^2| < 10$ MeV/c^2.

2. For K^0_S candidates we reject a V^0 mass window with the mass hypothesis Λ and $\bar{\Lambda}$ with the condition $|M(p(\bar{p}),\pi^+(\pi^-))$ - 1.1157MeV/$c^2| < 5$ MeV/c^2.

This selection cut is important to reject candidates that decay with the same topology and therefore would not be filtered by only topological cuts. This rejection

criterion is complementary to previous selections and further reduces combinatorial background, particularly for higher transverse momenta, where selection by energy loss in the TPC is not that efficient.

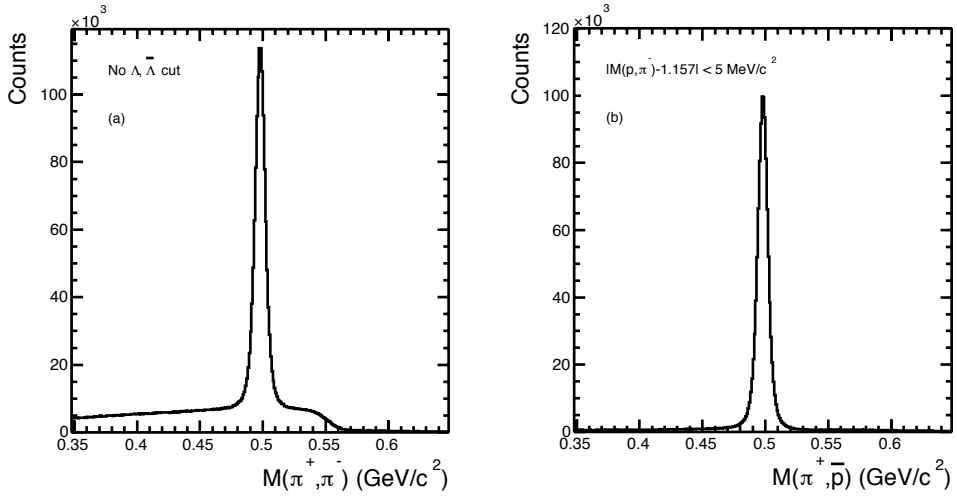

Figure 4.7: Before (a) and after (b) applying a Λ invariant mass cut on K^0_S. The combinatorial background becomes liner after this selection cut, which will be useful in calculating the net signal and background.

Figure 4.7 shows the effect of rejecting Λ and $\bar{\Lambda}$ mass peaks in the mass of K^0_S. We observe that the combinatorial background is more symmetrically distributed after this additional selection cut. In the following Figures 4.8-4.10 shows the K^0_S, Λ and $\bar{\Lambda}$ invariant mass peaks for the considered momentum studies of this analysis after all selection cuts. Green vertical lines represent the $\pm 6\sigma$ region and blue vertical lines represent the $\pm 12\sigma$ region around the measured mass peak, respectively after a Gaussian and liner polynomial fit to the data points (section 4.3).

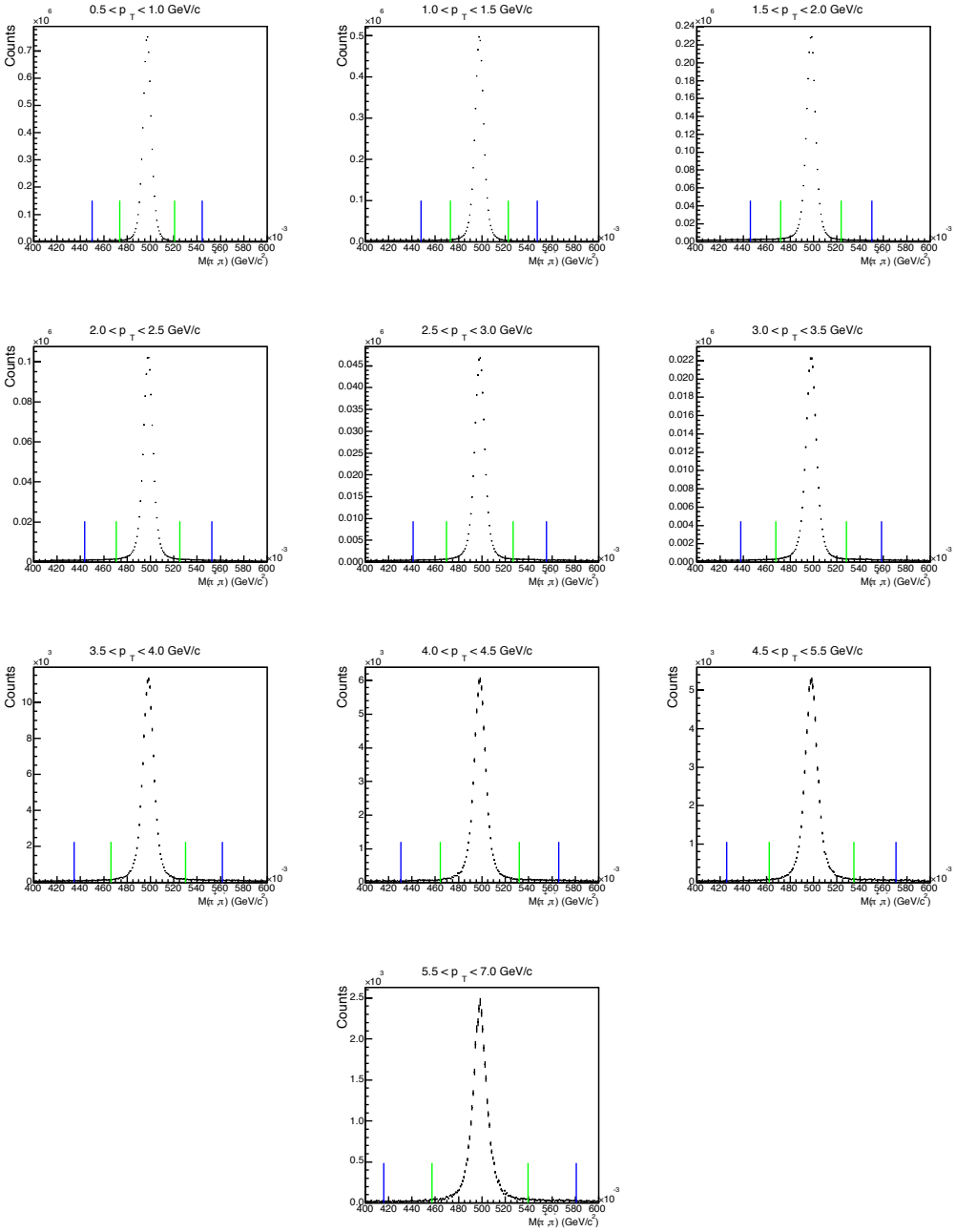

Figure 4.8: K^0_S invariant mass peaks after all selections have been performed. Two green vertical lines represent the $\pm 6\sigma$ region and blue vertical lines represent the $\pm 12\sigma$ region around the measured mass peak, respectively.

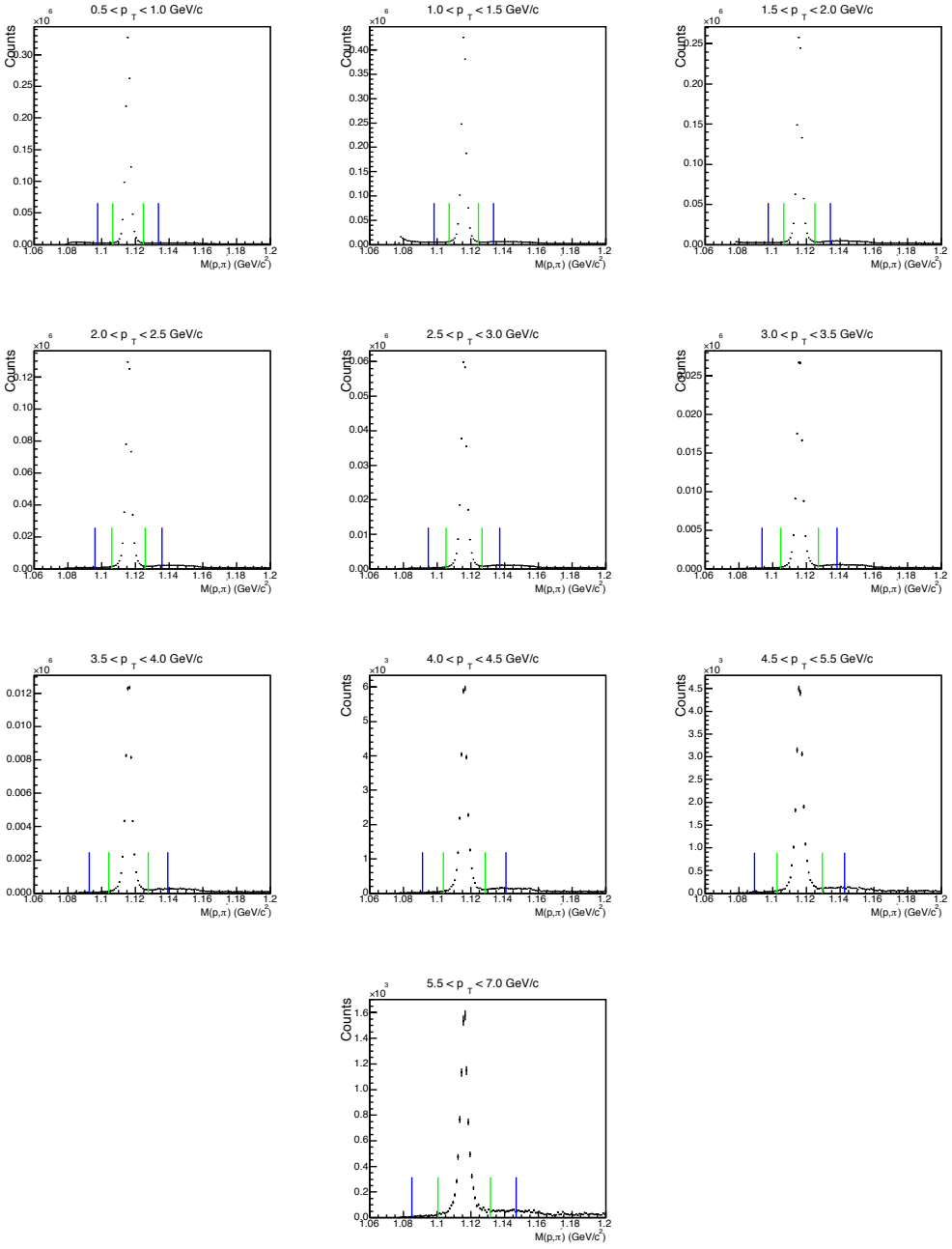

Figure 4.9: Λ invariant mass peaks after all selections have been performed. Two green vertical lines represent the $\pm 6\sigma$ region and blue vertical lines represent the $\pm 12\sigma$ region around the measured mass peak, respectively.

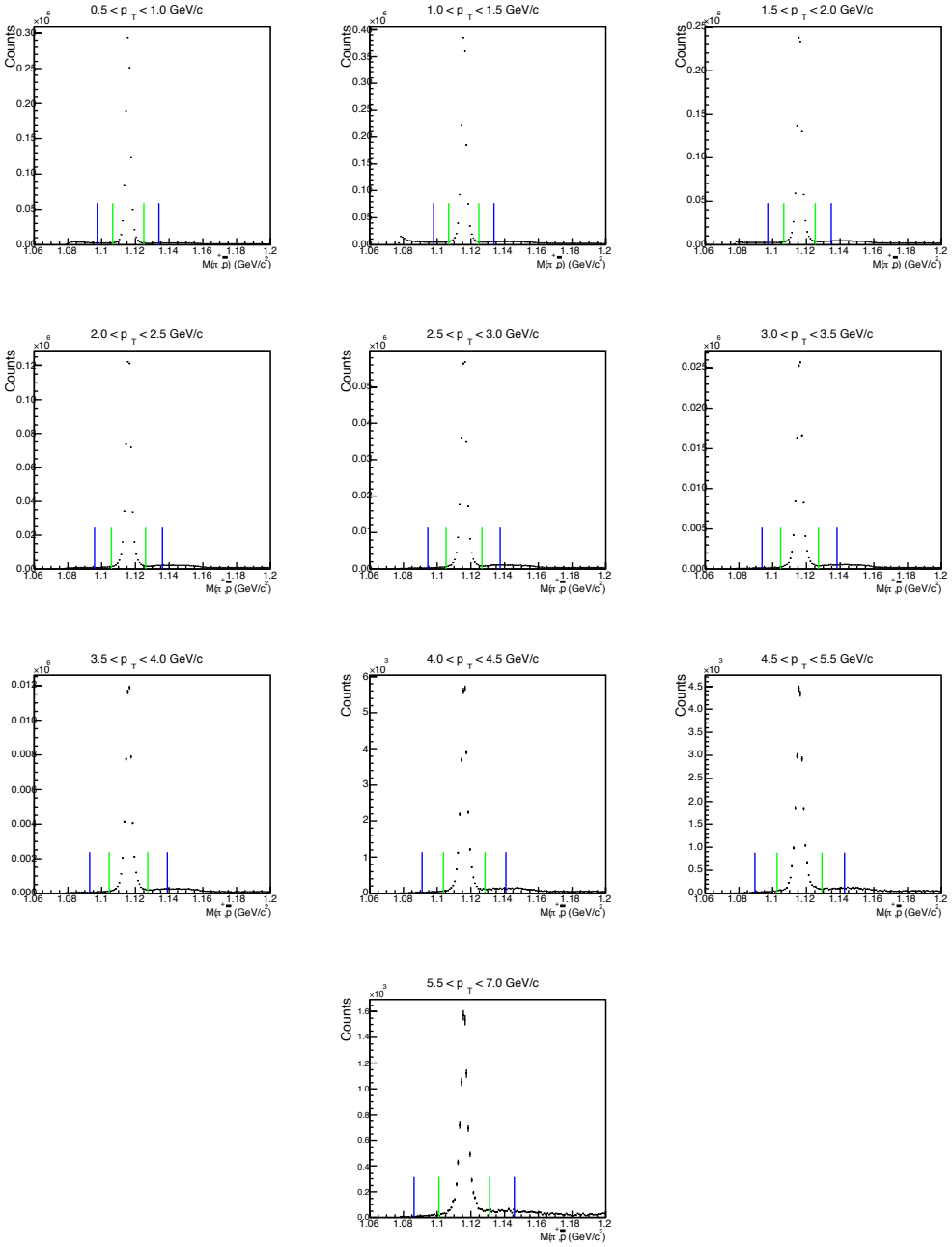

Figure 4.10: $\bar{\Lambda}$ invariant mass peaks after all selections have been performed. Two green vertical lines represent the $\pm 6\sigma$ region and blue vertical lines represent the $\pm 12\sigma$ region around the measured mass peak, respectively.

4.3 Determination of the V^0 transverse momentum spectra

In this section we will discuss how to obtain the number of V^0s in the invariant mass peaks for different transverse momentum regions after applying all selection cuts discussed the previous sections. Once we obtain the candidates in a particular p_T region we fill the transverse momentum spectra. We will also discuss two of the most important necessary corrections to these spectra:

1. The reconstruction efficiency correction, based on a Monte Carlo technique.
2. A novel feeddown correction, in order to subtract Λ and $\bar{\Lambda}$ coming from multi strange decays.

4.3.1 Signal extraction

Once the candidate selections described in previous sections are applied, we obtain the invariant mass distributions as shown in Figure 4.11. The next step is the calculation of the number of candidates in this peak region. First we fill different invariant mass distributions in each relevant transverse momentum region.

To quantify the signal and background we introduce a Gaussian function for the signal and linear function for the background, and we fit data distributions

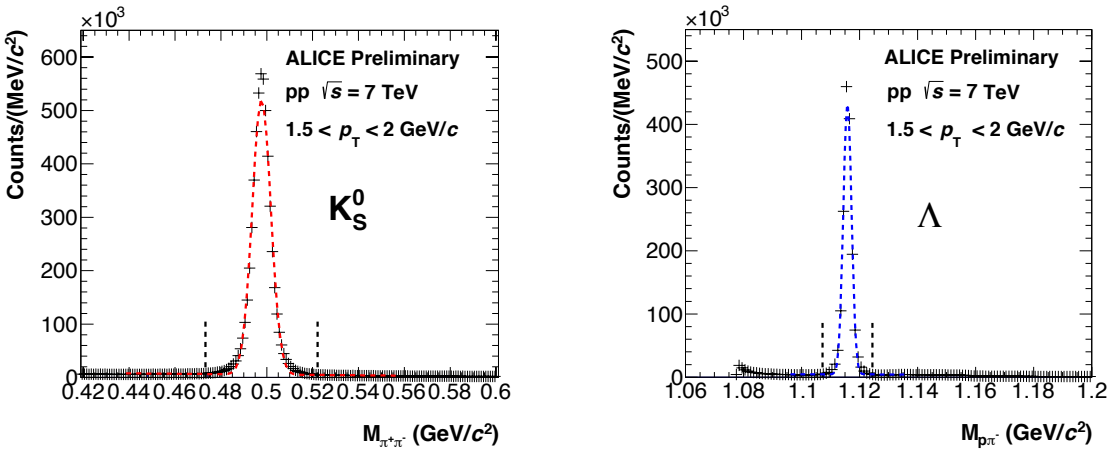

Figure 4.11: Λ (left) and K^0_S (right) invariant mass peaks after all selections have been performed. The dashed curve is the fitted Gaussian plus linear function and the two black vertical lines represent the $\pm 6\sigma$ region around the measured mass peak (Λ = 1.115 GeV/c^2, K^0_S = 0.497 GeV/c^2).

with this fit function, which is given in Equation 4.6.

$$f(x) = \frac{1}{\sigma\sqrt{2\pi}} e^{-\frac{(x-\mu)^2}{2\sigma^2}} + cx + d \tag{4.6}$$

Here a, b, c and d are free parameters and σ is the width and μ is the mean (invariant mass peak position) of the Gaussian distribution. Using these two parameters we can sample three different regions of the invariant mass distribution.

1. Signal region: We select the nσ mass window around the extracted mean of the Gaussian. Thus the limits of the signal region are [μ-nσ, μ+nσ].

2. Left side of the background: We select a 2nσ mass window to the left of the extracted mean of the Gaussian as the left background region. Thus the

limits of this region is [μ-2nσ, μ-nσ].

3. Right side of the background: We select 2nσ mass window to the right of the extracted mean of the Gaussian as the right background region. The limits of this region are [μ+nσ, μ+2nσ].

Here n is an integer value chosen based on the regularity of the invariant mass distributions (in this analysis n=6). The different regions are shown in Figure 4.11. In order to subtract the background in the peak region the width of the two background sampling regions was chosen to be equal to the width of the peak region, so one simply can subtract the counts in the background regions from the number of candidates in the peak region. This procedure of signal extraction is called the bin counting method.

The final signal extraction can be written as:

1. N_{RS}= N[μ-6σ, μ+6σ]

2. N_{BK}= N[μ-12σ, μ-6σ]+N[μ+6σ, μ+12σ].

3. N_{NT}= N_{RS}-N_{BK}.

N_{RS} denote the number of candidates contained in the interval [μ-6σ, μ+6σ] underneath the mass peak (Raw Signal) and N_{BK} is the total background signal in the two intervals[μ-12σ, μ-6σ], [μ+6σ, μ+12σ]. The net signal (NT) is simply the difference of the above two values. We repeat this procedure for each transverse momentum interval, resulting in transverse momentum, which we called

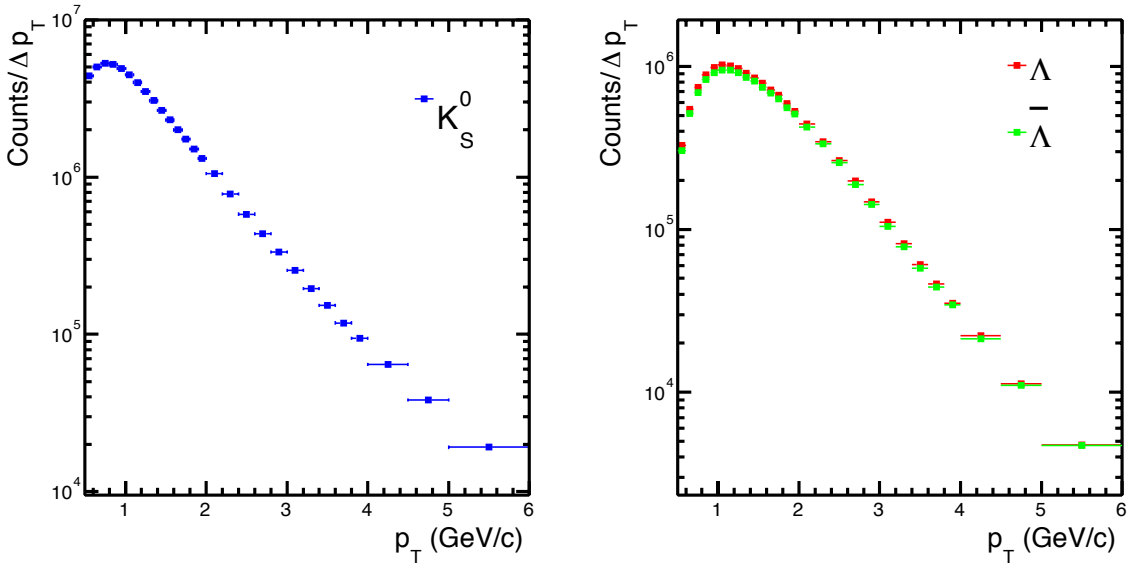

Figure 4.12: Λ, $\bar{\Lambda}$ (right) and K^0_S (left) transverse momentum spectra normalized by bin width Δp_T.

the transverse momentum spectrum shown in Figure 4.12. It is noted that in Figure 4.12 the p_T bin width ranges from 0.1 GeV/c below 2 GeV/c to 1 GeV/c above 5 GeV/c. To account for this bin asymmetry in the momentum spectrum we divide the candidate counts in each bin by the appropriate bin width.

4.4 Corrections to the raw p_T spectrum

The V^0s selected in the above sections are not all of the total V^0s created in the primary collision. One important study we need to perform is to find the ratio of how many particles were created in the primary collision to the ones that

were measured after selection cuts were applied, i.e finding the reconstruction efficiency of V^0s. There are several reasons why the total number of V^0s produced in the collision is not equal to the measured V^0s. First the probability of a V^0 that enters the acceptance of the TPC to be reconstructed is not 100%. This is due to some of the charged decay tracks possibly being swept out of the TPC acceptance by the magnetic field. The second reason is that some high p_T tracks (straighter tracks) may be going parallel to TPC sector boundaries. Another reason is that the topological cuts placed in the V^0 reconstruction take out some portion of the signal and reduce the reconstruction efficiency. A final important thing to consider is that the total V^0s detected are not all primary V^0s, they may be decay products of multi strange particles. We need a method, which call the feed down correction, to sample out this secondary portion from all V^0s detected. The following subsections address both the reconstruction efficiency and the feeddown correction.

4.4.1 Calculation of reconstruction efficiency of V^0s

The only way to determine the ratio of generated to reconstructed V^0s is to perform a Monte Carlo simulation based on a realistic event generator such as PYTHIA. Using the simulation we define the reconstruction efficiency for each p_T interval as:

$$\epsilon = \frac{\text{Number of detected associated } V^0\text{s after selection cuts}}{\text{Number of primary } V^0\text{s generated}} \tag{4.7}$$

The numerator of this fraction is determined using the same signal extraction procedure in simulated data than in real data, which minimizes systematic uncertainties. The denominator is simply computed by counting the respective V^0s generated in each momentum range in the the simulated events. These particles are not propagated through the detector elements. Note that it is necessary to define the primary particles in the calculation of efficiency. We use the convention by ALCE that is described in Chapter 4.1. For example, all $\Xi^{\pm}$ are primary particles. When it comes to Λ and $\bar{\Lambda}$ there is a significant contribution from Ξ decays, for example Ξ^+ decay into Λ and π^+ with a 99% probability. The reconstruction

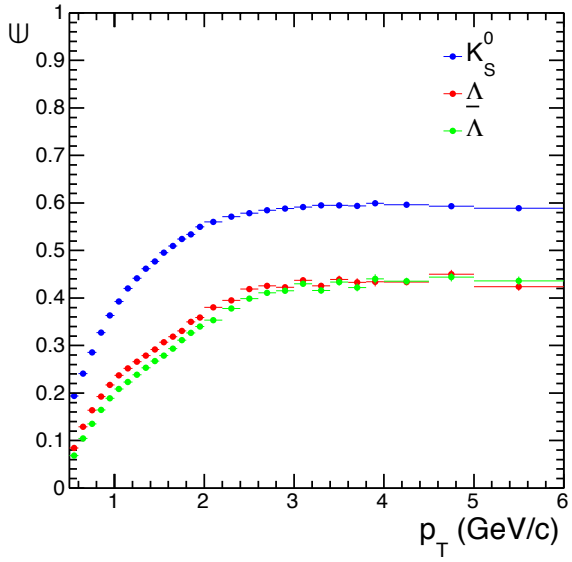

Figure 4.13: Λ, $\bar{\Lambda}$ and K^0_S detection efficiency after all selection cuts applied.

efficiency for all the strange hadrons analyzed in this work can be seen in Figure 4.13. This efficiency includes the probability of measuring a given decay channel

for a particular V^0 particle. Here, we note that for low transverse momentums efficiency is reduced due to the difficulty of detecting the associated mesons, which carry very little momentum.

4.4.2 Feeddown correction

The option of using the more traditional inclusive feeddown calculation is not available in this analysis, since no measurement of the Ξ^- and Ξ^0 production in association with jets and the underlying event is available.

To overcome this difficulty, we have investigated the use of a novel data-driven feed down correction based on the distance of closest approach (DCA) to the primary vertex of secondary and primary V^0s. The DCA distributions for these two contributions are different enough that a change of DCA selection in the analysis will result in the removal of a different fraction of each contribution. When varying the DCA selection, one can use the relative signal change observed in data to determine the fraction of secondaries present in the analysis via:

$$\left(\frac{\Delta S^{Data}}{S^{Data}}\right) = f_{prim}\left(\frac{\Delta S^{MC}_{prim}}{S^{MC}_{prim}}\right) + f_{sec}\left(\frac{\Delta S^{MC}_{sec}}{S_{sec}}\right) = \left(\frac{\Delta S^{MC}_{prim}}{S^{MC}_{prim}}\right) + f_{sec}\left[\left(\frac{\Delta S^{MC}_{sec}}{S_{sec}}\right) - \left(\frac{\Delta S^{MC}_{prim}}{S^{MC}_{prim}}\right)\right] \tag{4.8}$$

where S^{Data} is the total signal observed in data, $S^{MC}_{prim/sec}$ are the primary and secondary signals as seen in simulations, ΔS denotes, in all cases, the observed signal variation when changing the DCA selection, and $f_{prim/sec}$ is the fraction of primary

and secondary V^0s in the real data, where $f_{prim}+ f_{sec}$=1. As a benchmark, the inclusive[1] f_{sec} computed with this method compares favorably with the fraction of secondaries computed with a more traditional approach that utilizes a feeddown matrix and a Ξ measurement, as can be seen in Figure 4.14.

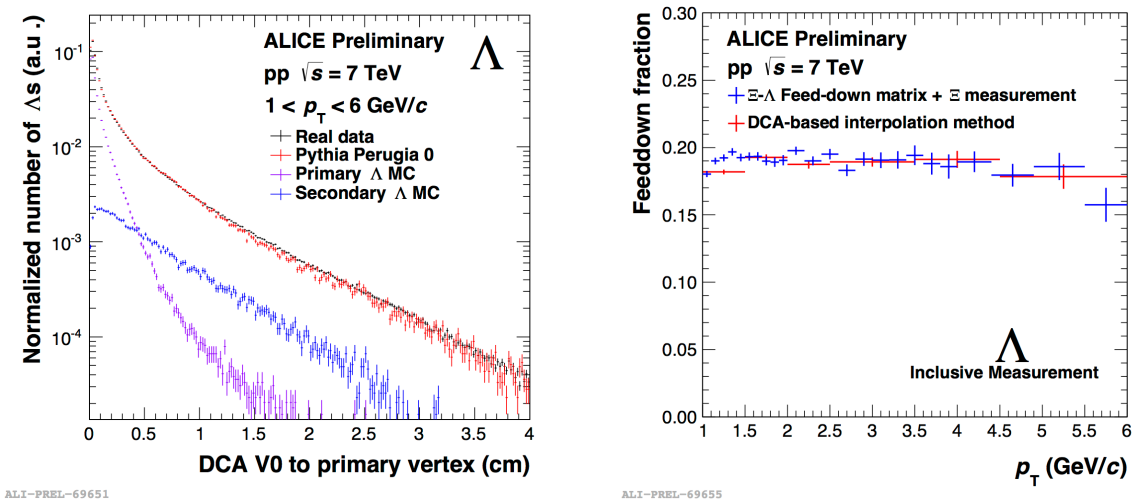

Figure 4.14: Estimation of the feeddown fraction of Λs from Ξ^- and Ξ^0 using a scaling method based on the DCA to the primary vertex.

Here, the left panel shows the distributions of DCA to the primary vertex of Λs in real data (black) and reconstructed MC data (red). The other two distributions are primary (magenta) and secondary (blue) Λs, respectively. Only Λs from Ξ^- and Ξ^0 were considered as secondary. The right panel shows the feeddown fractions from the more standard Ξ measurement with feeddown matrix

[1]Total Λ yields from the near side, away side and underlying event.

(blue) and the scaling method based on the DCA to primary vertex (red). This result is encouraging, since the DCA-based interpolation method has the advantage that one can determine a feeddown fraction in each region (near and away side, underlying event) separately. Work is currently ongoing to finalize these yields, which includes incorporating the associated particle efficiency corrections as well as performing track splitting studies.

Chapter 5

Di-hadron correlation technique in hadronic and heavy-ion collisions

The general idea behind the di-hadron (two-particle) correlation analysis [153, 154, 155, 156, 157] is to investigate the angular relationship between produced particles in a hadronic or heavy-ion collision by sampling produced particles via pairs of particles. This distribution of pairs of particles is given as a function of azimuthal angular and pseudorapidity separation. One of the most important applications in a two-particle correlation analysis is to study the jet-like phenomena in high energy pp and nuclear collisions, which allows us to quantify the small amount of initial hard scattered parton fragments, which are accompanied by more abundant low momentum particles from soft parton interaction (underlying physics). The production mechanism of hard partonic fragments is well understood in pQCD calculations and known as hard QCD. On the other hand,

the underlying physics components are not well understood. The main particle production mechanisms in underlying physics are multiple particles interactions [158], initial and final state radiation [159] and beam detector interactions. These components act as a combinatorial background and mask some important details of parton fragmentation, thus it is important to have a better control and understanding of these processes to fine tune final results of hadronic collisions and some of the characteristic parameters of Monte Carlo event generates. The situation is more complicated in nuclear collisions where event-by-event jet reconstruction algorithms fail to disentangle flow and non flow components from each other. The main advantage of two-particle correlations in jet-like analysis is that one does not need to reconstruct jets on an event-by event basis, but rather can study jets by means of summing over many events. The other important advantage of two-particle correlations is that one can easily tag identified particles in the analysis, which allows one to investigate quark fragmentation functions, particle ratios in the jet and underlying event regions, etc.

5.1 Particle identified di-hadron correlation analysis

To construct identified particle pairs (PID correlation) we first define a special reference particle called the trigger particle in a given transverse momentum interval a< p_T^{Trig} <b. The trigger particle is a non-identified charged particle. The relative distribution of other particles is measured with respect to the trigger particle. These particles are called associated particles. Associated particles have

certain momentum interval with the condition $p_T^{Associate} < p_T^{Trig}$. The associated particles considered in this analysis are the V^0s reconstructed in Chapter 4. To achieve a good statistical base we combine the Λ and $\bar{\Lambda}$ particles. Each pair of particles is used only once for the correlation function. Figure 5.1 shows a schematic representation of particle distributions in a hadronic collision. The left figure shows the azimuthal distribution and right figure shows the distribution in the XY plane. The red arrow is for the trigger particle and green is for the associated particles. The cone shaped particle cluster formed near the trigger particle is called the near-side jet. Directly opposite to the near-side jet with an azimuth difference of π is the away-side jet. Once all the kinematics and track cuts are applied to the trigger particles and associated particles we construct particle pairs as follows. The angular and psudorapidity separation of each pair is calculated by the relative difference with respect to the trigger particle.

$$\Delta\phi = \phi^{Trigger} - \phi^{V^0}$$

$$\Delta\eta = \eta^{Trigger} - \eta^{V^0}$$

The above two separations are added to a two dimensional correlation distribution and the process repeats on the next pair in the same-event until all pairs were considered. Then the next event is analyzed in the same fashion. After the correlation pairs have been determined for all trigger particles, there number is normalized by the total number of trigger particles. This per-trigger normalization of the correlation function scales the total hadron production by the number of hard scatterings of the events. One can relate this to the scaling of R_{AA} by number of binary collisions (N_{bin}) in heavy-ion collisions. The p_T range of the

accepted trigger particles play an important role in the correlation analysis and the physical interpretation of the measurement.

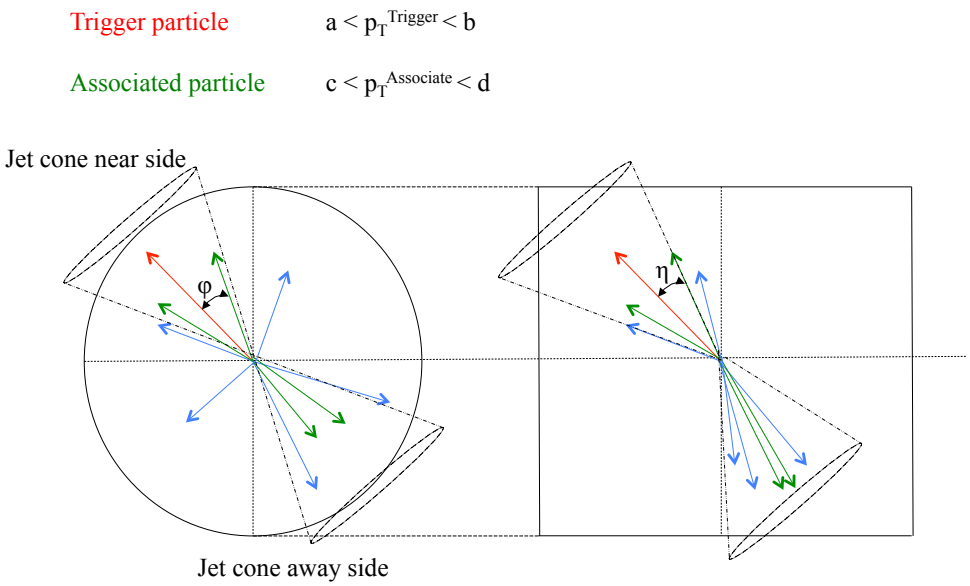

Figure 5.1: Schematic representation of particle distributions in a hadronic collision. The left figure shows the azimuthal distribution and the right figure shows the XY plane distribution. The red arrow is for the trigger particle and green is the associated particle. Note that particles are clustered around the trigger particle in what is known as a jet.

One should always attempt to select trigger particles come from the leading fragments of high p_T partons, which form a jet. We can achieve this by selecting the highest p_T trigger particle of the event, called the leading particle [160].

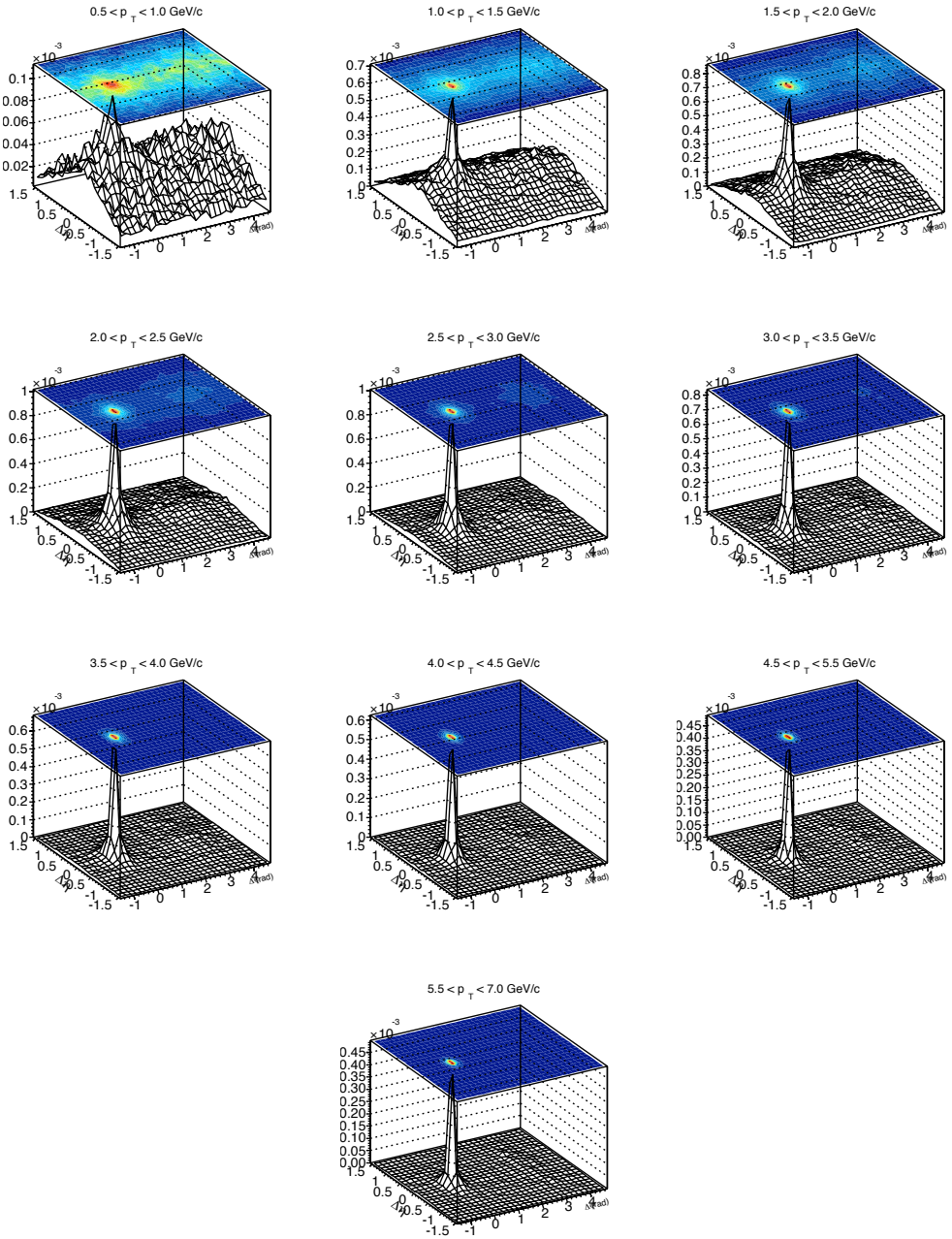

Figure 5.2: Same-event distributions for the K^0_S with $0.5 < p_T < 7$ GeV/c associated with a leading particle in $5 < p_T < 10$ GeV/c.

Figure 5.2 shows the two dimensional $\Delta\eta$, $\Delta\phi$ correlation in a pp collisions for the same-event distribution with K^0_S as the associated particle with appropriately sub binned transverse momentum of 0.5-7 GeV/c; the leading particle is fixed at $5 < p_T < 10$ GeV/c. The peak at $\Delta\eta$, $\Delta\phi$=0,0 is the near-side jet peak. One of the striking features of the two dimensional $\Delta\eta$, $\Delta\phi$ correlation distribution is the underlying structure due to the acceptance of the detector. This is the triangular shape beyond the peak position. The origin of the acceptance effect will be explained in section 5.1.1. Thus, the acceptance effect needs to be removed from the same-event distribution to recover the relevant physics signals. We follow a special procedure called event mixing to remove the acceptance effect. In the following subsections we describe the cause and how to remove the acceptance effect using mixed-event technique.

5.1.1 Acceptance effect

The acceptance effect is solely due to the finite pseudo-rapidity (η) coverage of the main tracking detector of the experiment. In ALICE the coverage ranges -0.9< η <0.9, and any trigger particle or associated particle has to be detected in this range. In Figure 5.3 we try to illustrate the effect of the finite η range of ALICE TPC. It shows how any particle pair in η translates to $\Delta\eta$. Imagine a trigger particle in η^{Trig}=-0.9 (red arrow on eta axis), and the associated particle can be found in any range between -0.9< $\eta^{Associate}$ <0.9. Then $\Delta\eta_{Max}$=-0.9-(-0.9)=0 and $\Delta\eta_{Min}$=-0.9-0.9=-1.8, which is shown in the red window of the $\Delta\eta$ distribution. Now imagine a trigger particle in η^{Trig}=0.9 (blue arrow in eta axis),

where yet again the associated particle can be found form any range between -0.9< $\eta^{Associate}$ <0.9, now $\Delta\eta_{Max}$=0.9-(-0.9)=1.8 and $\Delta\eta_{Min}$=0.9-0.9=0, which is shown in the blue window of the $\Delta\eta$ distribution. These limits are the maximum and minimum of the $\Delta\eta$ that fulfills the above trigger condition. Now consider a different position of a trigger particle, η^{Trig}=-0.45 (green arrow in eta axis) with the same associated particle interval of (-0.9< $\eta^{Associate}$ <0.9), but now the $\Delta\eta_{Max}$=-0.45-(-0.9)=0.45 and $\Delta\eta_{Min}$=-0.45-0.9=-1.35, as shown in the green window in the $\Delta\eta$ distribution. Next consider a trigger particle with η^{Trig}=0.45 (purple arrow in eta axis) with still the same associated particle interval has a $\Delta\eta_{Max}$=0.45-(-0.9)=1.35 and $\Delta\eta_{Min}$=0.45-0.9=-0.45 as shown in the purple window in the $\Delta\eta$ distribution. We can continue this for all trigger parcels until η^{Trig}=0, at which the maximum and minimum limits will produce a triangular shape in the $\Delta\eta$ axis. This triangular shape is the underlying correlation visible in the same-event distribution in Figure 5.2. One can now simply state that acceptance effect reflects the probability of finding a certain particle pair in a given region of the $\Delta\eta$,$\Delta\phi$ phase space. The effect of the acceptance depends on the eta-range of the central track of the experiment. ATLAS and CMS at CERN have a triangular shape in the range of $\Delta\eta_{Max}$ = 4 and $\Delta\eta_{Min}$ = -4; whereas the PHOBOS experiment at RHICH only has a range of $\Delta\eta_{Max}$ =2 to $\Delta\eta_{Min}$ = -4.

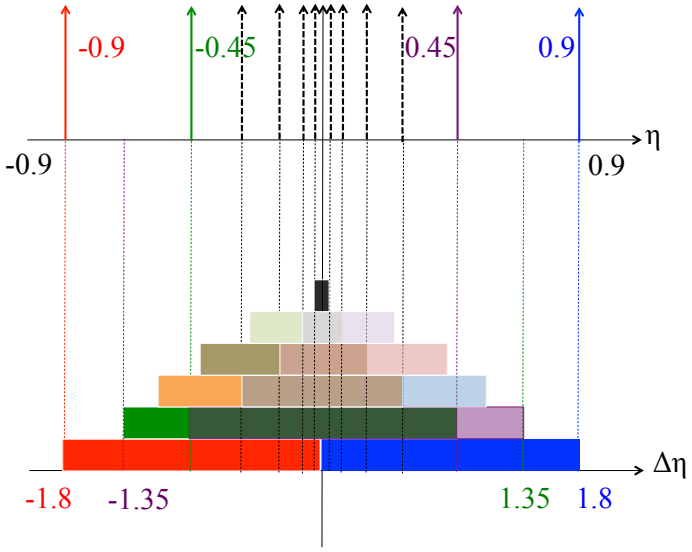

Figure 5.3: Representation of the acceptance effect due finite η of ALICE TPC.

5.1.2 Mixed-event technique

To reproduce the acceptance effect above we use a technique called event mixing. The main logic behind the event mixing technique is to construct uncorrelated pairs from specially selected different events. Those pairs still carry the acceptance effect by maulding the radial and azimuthal conditions from each event but since the pairs formed from particles of different events where no physics is contained in the correlation function.

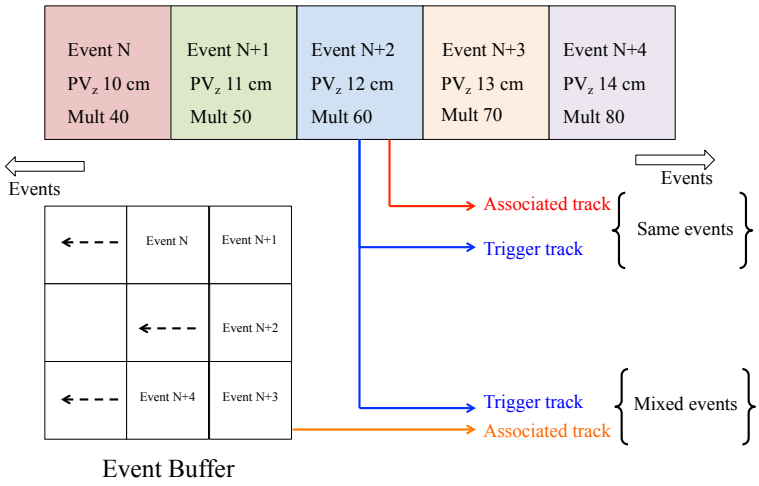

Figure 5.4: Schematic representation of event flow in the mixed-event pool.

The procedure followed to construct correlation pairs from mixed events is shown in Figure 5.4. The events shown in ...,N,N+1,N+2.. represents the regular events or same-events (SE) in a ROOT TTree object. PV_Z is the primary vertex z position and Mult is the multiplicity of the event. The blue arrow represents the trigger track and red arrow is for the associated track in SE. We continue this procedure for each event from N=0 to N=270X10^6. To reproduce the acceptance effects well we make sure to select events with similar multiplicity and PV_Z position. Therefore if any two events have a primary vertex difference of $|\Delta PV_Z|$<1cm and multiplicity difference of |ΔMult|<10 we build an event pool with those two events. The above procedure was continued until 50,000 such events are cached into the event pool. To reduce the computational time we only store the η,ϕ and p_T information of selected tracks in the event pool. A decision has to be made

whether trigger or associated particle should be stored in the event pool. In most analyses trigger particles are stored in the event pool because of their limited numbers compared with the associated tracks, which will cause less memory consumption when running the event mixing loop. As discussed in the previous section our analysis uses charged trigger particles and V^0s as the associated particles. Since V^0s are relatively rare compared with the charged tracks we build our event pool with the track information of the associated V^0s. To get a good statistical sample of mixed events (ME) we mix one event with five events in the event pool. Once the event pool is ready we get trigger tracks in the regular events and associated tracks from the event pool. Figure 5.5 shows the two particle correlation structure using the mixed-event technique. One should note that it is important to determine how to normalize the mixed-event distribution. As explained earlier the acceptance effect shows the probability of finding a certain particle pair in a given region of a $\Delta\eta$,$\Delta\phi$ phase space. So we need to find the point where the probability of finding an associated particle w.r.t a trigger particle is maximum. If the trigger particle is in the acceptance at $\Delta\phi = \Delta\eta = 0$ then the associated particle is also in the same direction and in the acceptance, thus we should normalize the mixed-event distribution to one (maximum probability) at $\Delta\phi$,$\Delta\eta = 0,0$.

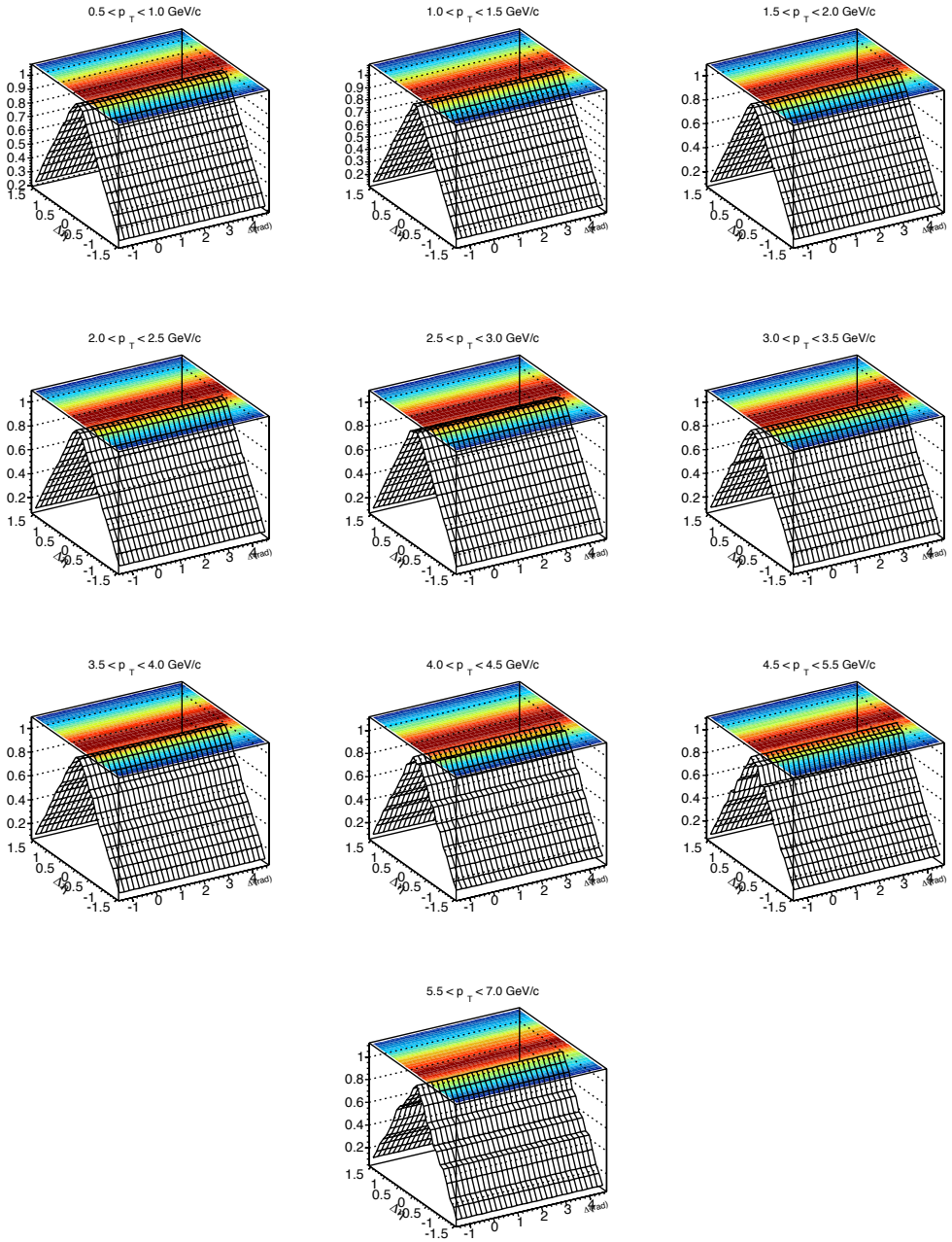

Figure 5.5: Normalized mixed-event distributions for the K^0_S in $0.5 < p_T < 7$ GeV/c associated with a leading particle in $5 < p_T < 10$ GeV/c.

5.2 Definition of the correlation function

The main correlation function in this analysis is constructed to extract the associated per trigger yield as a function of the $\Delta\phi$ and $\Delta\eta$. This can be shown mathematically in the following equation.

$$\frac{d^2N}{d\Delta\phi d\Delta\eta}(\Delta\phi,\Delta\eta) = \frac{1}{N_{Trig}}\frac{dN_{Assoc}}{d\Delta\phi d\Delta\eta} \tag{5.1}$$

To remove the acceptance effect we simply divide the same-event distribution by the normalized mixed-event distribution. Now one can write the correlation function as:

$$\frac{1}{N_{Trig}}\frac{dN_{Assoc}}{d\Delta\phi d\Delta\eta} = \frac{S(\Delta\phi,\Delta\eta)}{B(\Delta\phi,\Delta\eta)} \tag{5.2}$$

Where S($\Delta\phi,\Delta\eta$) and B($\Delta\phi,\Delta\eta$) are defined as:

$$S(\Delta\phi,\Delta\eta) = \frac{1}{N_{Trig}}\frac{dN^{SE}_{Assoc}}{d\Delta\phi d\Delta\eta} \tag{5.3}$$

$$B(\Delta\phi,\Delta\eta) = \frac{1}{\beta(0,0)}\frac{dN^{ME}_{Assoc}}{d\Delta\phi d\Delta\eta} \tag{5.4}$$

Here $\beta(0,0)$ is the scale factor, which normalizes the mixed-event distribution to unity at $\Delta\phi$,$\Delta\eta$ = 0,0. Examples of an acceptance corrected $\Delta\phi$,$\Delta\eta$ correlation function for K^0_S and Λ+$\bar{\Lambda}$ are shown in Figure 7.3 and 5.7. A clear localized peak is visible in the region of $\Delta\phi$,$\Delta\eta$ = 0,0 that corresponds with the same-side peak and the away-side jet peak is elongated in $\Delta\eta$ due to the shift of parton center-of-mass system (cms) with respect to the cms of the collision. Now one can simply select regions in $\Delta\eta$ and project in $\Delta\phi$ to extract particle yields, peak widths, etc.

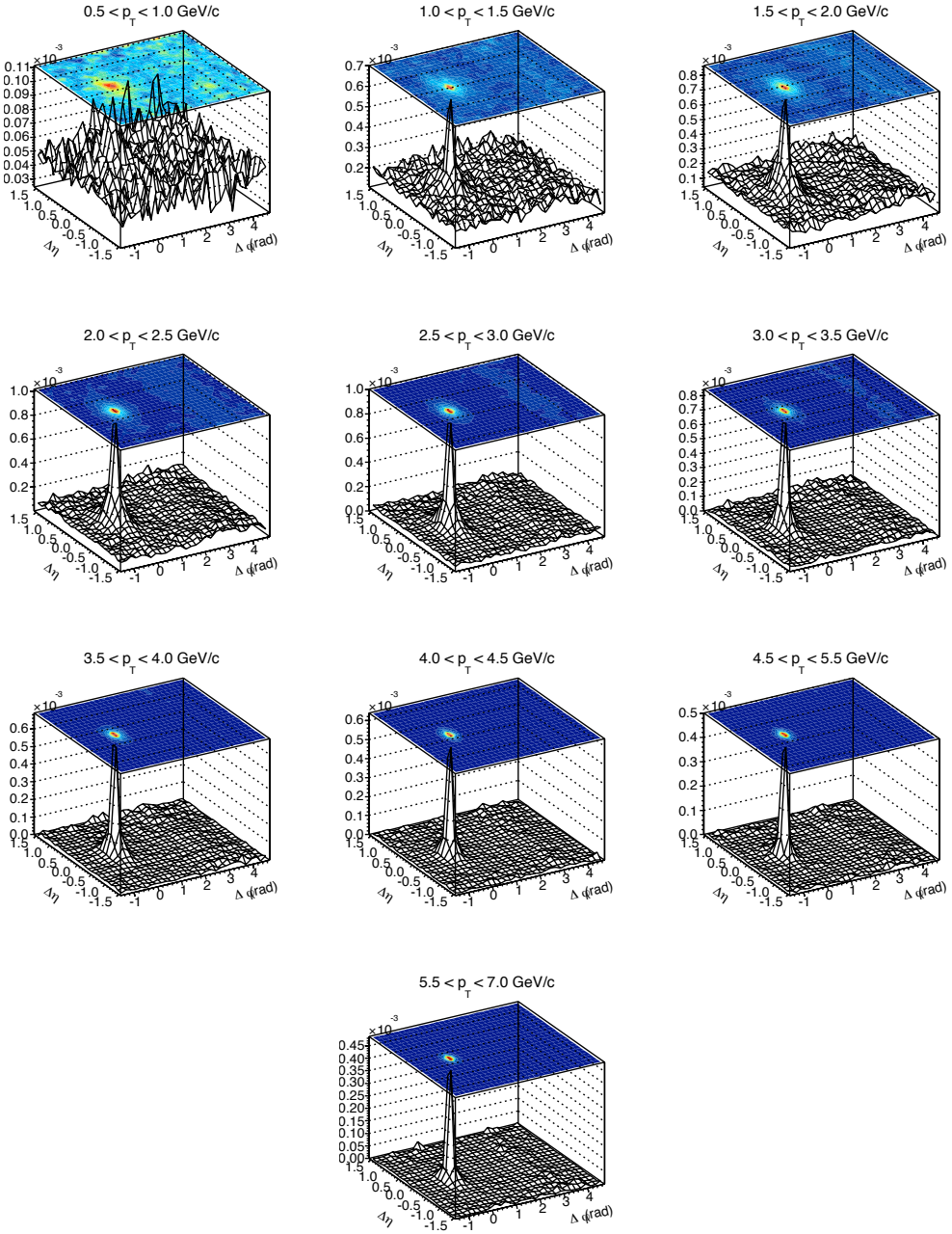

Figure 5.6: Acceptance corrected two dimensional $\Delta\eta$,$\Delta\phi$ correlation structures for K^0_S in ten transverse momentum intervals.

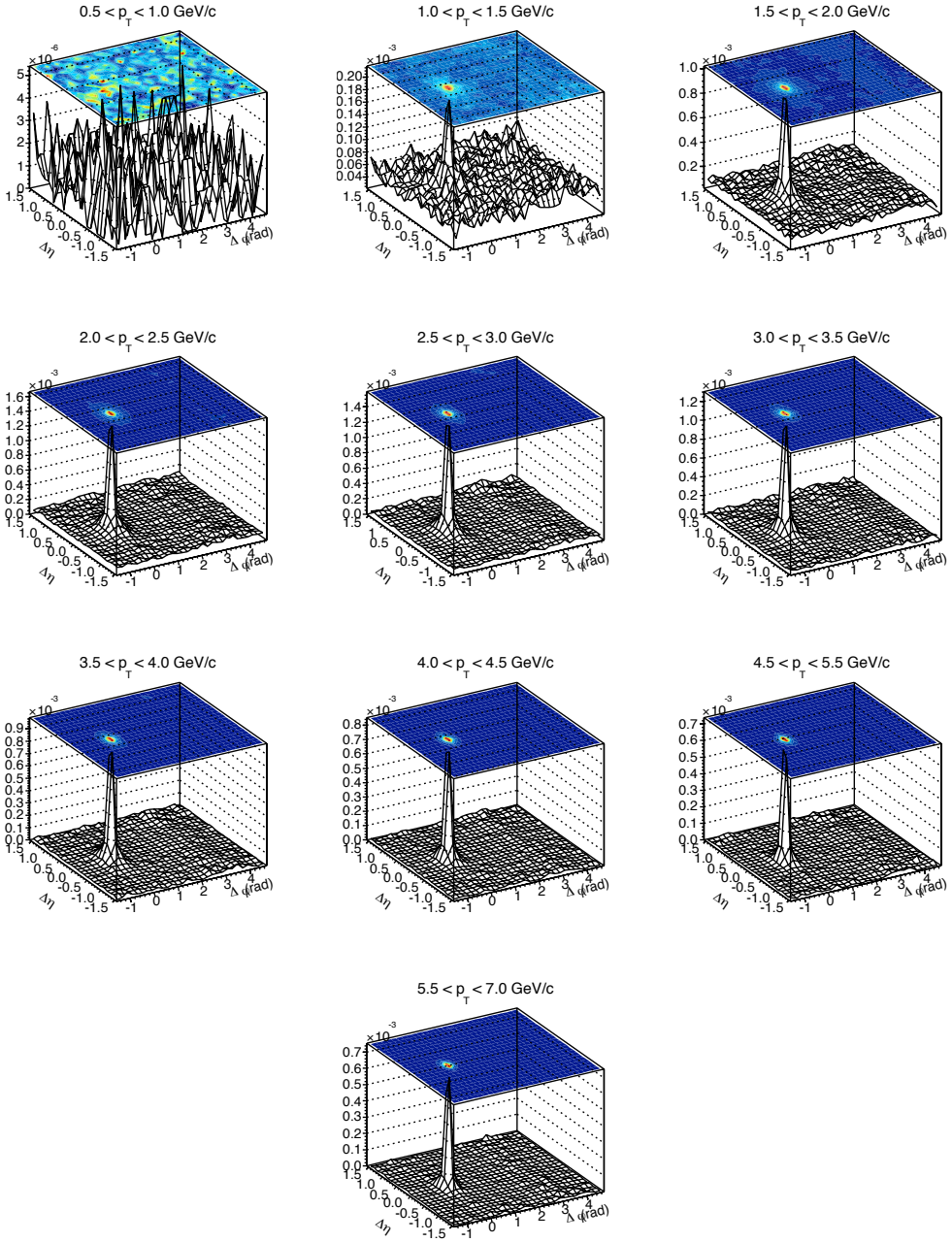

Figure 5.7: Acceptance corrected two dimensional $\Delta\eta$,$\Delta\phi$ correlation structures for Λ+$\bar{\Lambda}$ in ten transverse momentum intervals.

5.2.1 Definition of the jet region and underlying event

A projected one dimensional correlation function leads to an azimuthal correlation function, which is defined as:

$$\frac{dN}{d\Delta\phi} = \frac{1}{N_{Trig}} \frac{dN_{Assoc}}{d\Delta\phi} \tag{5.5}$$

Example of azimuthal correlations as a function of $\Delta\phi$ are shown in Figure 5.8. Since the limits of azimuth in the ALICE TPC ($0< \phi < 2\pi$) are periodic in ϕ, the difference in $\Delta\phi$ is always equal to 2π. To better visualize the back-to-back di-jets in $\Delta\phi$=0 and $\Delta\phi$=π we artificially set the limits of $\Delta\phi$ to [-π/2,3π/2]. If $\Delta\phi$ of any pair is less than the -π/2 we calculate a new $\Delta\phi_{New}$=$\Delta\phi$+2π. If $\Delta\phi$ of any pair is greater than 3π/2,$\Delta\phi_{New}$=$\Delta\phi$-2π. This ensures that all pairs considered are well inside the limits [-π/2,3π/2]. Note that the near-side peak is clearly visible at $\Delta\phi$=0 and the elongated away-side peak is visible at $\Delta\phi$=π.

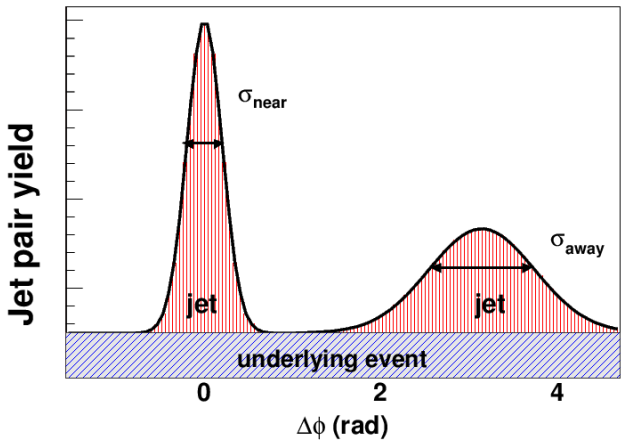

Figure 5.8: Different regions of the correlation function. Narrow near-side and broad away-side with an underlying region are shown.

Figure 5.9 shows the projection of the acceptance corrected correlation function in $|\Delta\eta|$ <1 to $\Delta\phi$ for K^0_S (left) and Λ+$\bar{\Lambda}$ (right).

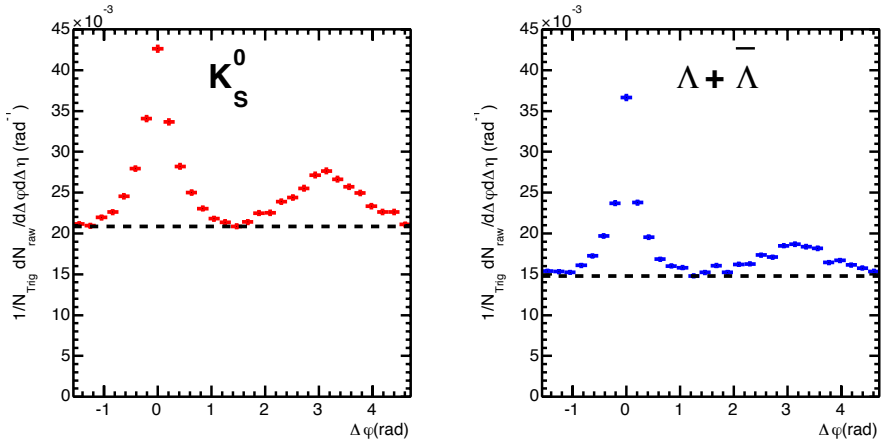

Figure 5.9: Projection of the acceptance corrected correlation function in $|\Delta\eta|$ <1 to $\Delta\phi$. Left figure is for the K^0_S and right is for the Λ+$\bar{\Lambda}$. Dashed line represents the combinatorial background.

One important observation is that there is still an uncorrelated background over the whole $\Delta\phi$ range beyond two jet peaks, which is roughly shown by the dashed line in the correlation distribution. This uncorrelated background is the underling event (UE) activity [161, 162]. As we know the two jet regions are due to the fragmentation of high p_T patrons (hard QCD) and the UE is due to the multi-parton interaction, initial and final state radiation, etc. To separate true jet yields in correlation functions a combinatoric background must be subtracted, using a constant offset. In many previous analyses the method of zero yield at minimum (ZYAM) has been used to quantify jet yields [163]. The determination

of the underlying event (background source) from this offset is one of the most important steps in this analysis.

5.3 Underlying event subtraction

Once the offset is determined as the minimum of the correlation function we assume that the jets on the near- and the away-side are separated by the offset and there are no jet-like associated correlations observed in this region between the peaks. This method is called the ZYAM. Now we subtract this uniformly distributed underlying event from the correlation data points and obtain the pure jet contributions that is shown in Figure 5.10. Note that now the minimum yield in the distribution is zero.

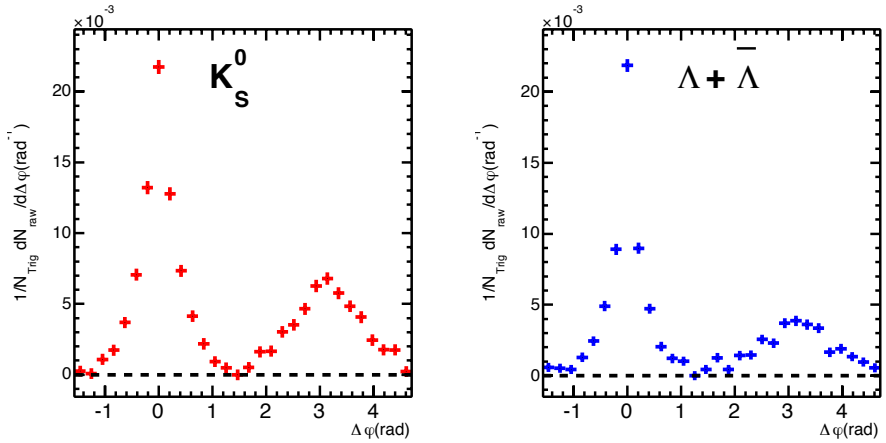

Figure 5.10: UE subtracted correlation function for the K^0_S (left) and for the Λ+$\bar{\Lambda}$ (right).

Now we can quantify the jet regions and UE region separately in $\Delta\phi$ as

- near-side region $-\pi/2 < \Delta\phi < \pi/2$
- away-side region $\pi/2 < \Delta\phi < 3\pi/2$
- Underlying event is the common pedestal over the full range of $-\pi/2 < \Delta\phi < 3\pi/2$

5.4 Extracting the correlation observables

Two of the most important observables we are extracting from the correlation functions as a function of transverse momentum evolution are:

- Per trigger yield in the uniformly distributed combinatorial background (Underlying event)
- near-side and away-side per trigger yields after subtracting the underlying event

Furthermore the $\Delta\phi$,$\Delta\eta$ widths of each correlation distribution can be extracted and the particle dependence of the size of the jet cone can be calculated as a function of transverse momentum. The widths are related to the radius of the jet cone by $\Delta r = \sqrt{\Delta\phi^2 + \Delta\eta^2}$.

5.4.1 Explain the correlation structure using different fit functions

To extract several important correlation observables we propose two fit functions to model the data points. The goodness of the fit is determined through a residual method, which will be described in Chapter 7.5. As describe earlier, since the correlation distribution is periodic in $\Delta\phi$=0 and $\Delta\phi$=π, the proposed fit functions are also chosen to be periodic in $\Delta\phi$. Fits using the function start with preset initial values for the free parameters and initiate several fits before converging to the chi-square minimized values. To minimize the chi-square we use the default TMinuit routine available in ROOT [164].

5.4.1.1 Double Gaussian for the near-side and single Gaussian for the away-side with a pedestal

The simplest fit function one can propose for the $\Delta\phi$ distribution is two Gaussian functions centered at $\Delta\phi$=0 and $\Delta\phi$=π to describe the peak regions with a constant liner function to describe the uniformly distributed combinatorial background (UE). One of the main disadvantages of this fit is that the Gaussian function centered at $\Delta\phi$=0 does not describe the tails at $\Delta\phi$=-1,1. To avoid this mismatch we introduce another independent Gaussian with a broader width and smaller amplitude than the previous one. Both near-side Gaussian functions are centered at $\Delta\phi$=0. Periodicity of the fit function is achieved via the condition $\Delta\phi$=$\Delta\phi\pm2n\pi$ where n=±1,±2,±3 for the near-side peak and n=±1/2,±3/2,±5/2

for the away-side peak. However, it was found that one Gaussian function is sufficient to describe the distribution of the away-side. The fit function in periodic form is given in Equation 5.6.

$$\begin{aligned}\frac{dN}{d\Delta\phi} = A_1 exp\left(-\frac{\Delta\phi^2}{2.\sigma_1^2}\right) + A_1 exp\left(-\frac{(\Delta\phi - 2.\pi)^2}{2.\sigma_1^2}\right) + \\ A_2 exp\left(-\frac{\Delta\phi^2}{2.\sigma_2^2}\right) + A_2 exp\left(-\frac{(\Delta\phi - 2.\pi)^2}{2.\sigma_2^2}\right) + \\ A_3 exp\left(-\frac{(\Delta\phi - \pi)^2}{2.\sigma_3^2}\right) + A_3 exp\left(-\frac{(\Delta\phi + \pi)^2}{2.\sigma_3^2}\right) + C\end{aligned} \tag{5.6}$$

Once the parameter values are calculated we can find some important observables such as

$$Y^{NS} = \frac{2.\pi}{N_{Trig}}(A_1.\sigma_1 + A_2.\sigma_2) \tag{5.7}$$

$$Y^{AS} = \frac{2.\pi}{N_{Trig}} A_3.\sigma_3 \tag{5.8}$$

$$Y^{UE} = \frac{a}{N_{Trig}} C \tag{5.9}$$

Figure 5.11 shows the different components of the Gaussian-based fit function for K^0_S (left) and $\Lambda + \bar{\Lambda}$ (right) in the momentum interval $1.5 < p_T < 2$ GeV/c. The black dashed line represent the sum of the fit function and the yellow line is the pedestal, magenta indicates the away-side jet. Pink and green Gaussians are the two fit functions that are needed to describe the near-side jet peak.

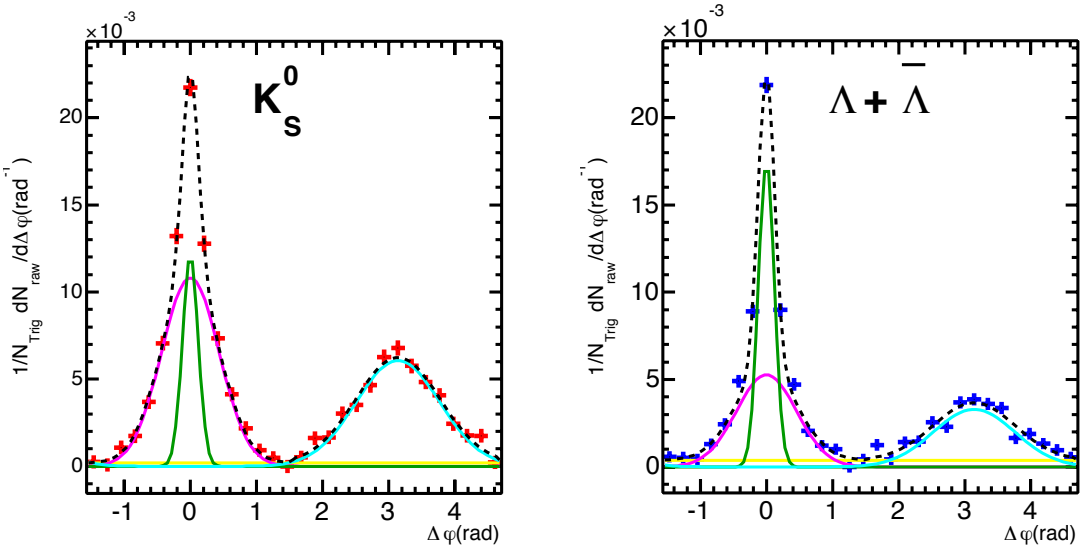

Figure 5.11: Two Gaussian functions for the near-side and single Gaussian function for the away-side fitted on top of the data points (K^0_S (left) and $\Lambda+\bar{\Lambda}$ (right) in momentum interval $1.5 < p_T < 2$ GeV/c). The uniform combinatorial background is modeled with a constant function.

5.4.1.2 Tsallis function for near and away-side with a pedestal

In the previous fit function we needed two Gaussians to describe the near-side peak. This can be avoided by using the q-Gaussian distribution for both the near-side and away-side [165, 166].

$$\frac{dN}{d\Delta\phi} = A_1\left(1-\beta_1(1-q_1)\Delta\phi^2\right)^{\frac{1}{1-q_1}} + A_1\left(1-\beta_1(1-q_1)(\Delta\phi-2.\pi)^2\right)^{\frac{1}{1-q_1}} + A_2\left(1-\beta_2(1-q_2)(\Delta\phi-\pi)^2\right)^{\frac{1}{1-q_2}} + A_2\left(1-\beta_2(1-q_2)(\Delta\phi+\pi)^2\right)^{\frac{1}{1-q_2}} + C \tag{5.10}$$

One of the striking features of the Tsallis function is its shape, which is dominated by a power law at large $\Delta\phi$, which will avoid the use of a second Gaussian described in the previous section. Thus we can use Tsallis to describe non Gaussian tails in the correlation function. In the limit of q→1 Tsallis behave as a Gaussian function and the σ value is given in terms of β as $\sigma = [2.\beta]^{-1/2}$. Figure 5.12 shows the Tsallis based fit function for K^0_S (left) and $\Lambda + \bar{\Lambda}$ (right) in momentum interval $1.5 < p_T < 2$ GeV/c.

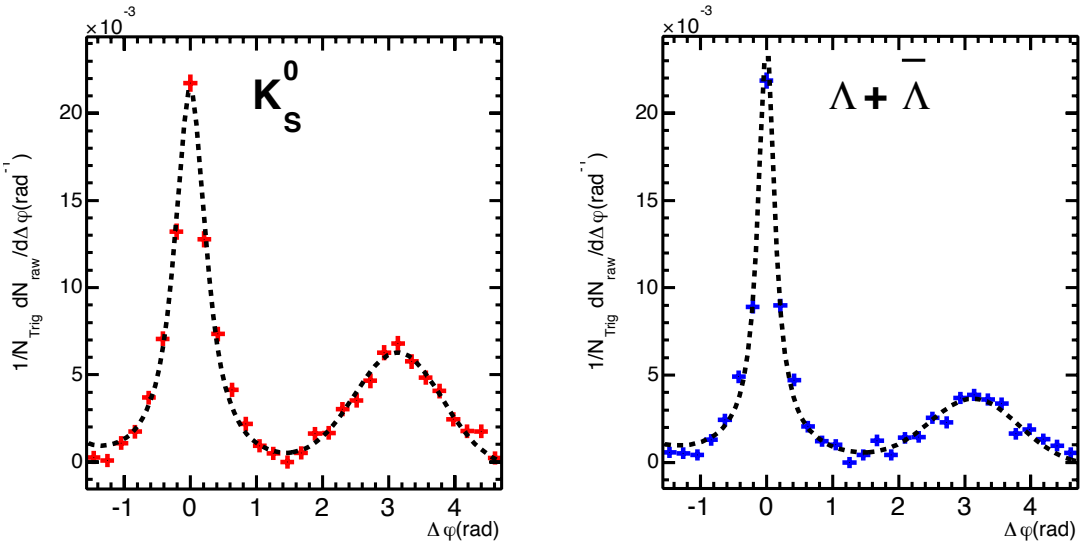

Figure 5.12: Single Tsallis function for the near-side and for the away-side fitted on top of the data points (K^0_S (left) and $\Lambda+\bar{\Lambda}$ (right) in momentum interval $1.5 < p_T < 2$ GeV/c). The uniform combinatorial background is modeled with a constant function.

Chapter 6

Systematic uncertainty study

Once we measure the $h^{\pm}$–V^0 correlations and extract the yields in different regions of the correlation function it is important to measure the stability of the final results by changing the parameters used in the analysis process. In a systematic study we are analyzing the change of the final result for a small change in analysis cuts and report the percentage change as a systematic uncertainty. In this section we will discuss how to calculate the systematic uncertainties and determine their main sources.

6.1 Different topological selections for V^0 decays

One of the most important systematics to consider is the stability of the extracted yields when the reconstruction cuts of the V^0 are changed. The selection of topological cuts mentioned in Chapter 4.2.1 have to follow a careful Quality Assurance

process, which is described here. First we need to apply the default topological cuts to reduce the combinatorial background while keeping as many of the signal candidates as possible. We first check the distributions of each selection cut in the signal and background region in a Monte Carlo simulation, where the reconstruction efficiency variations due to selection cuts can be easily controlled. As an example, Figure 6.1 shows the invariant mass on the y-axis and the respective topological cut on the x-axis. One can take the projections in the signal and background regions to observe the variations in the appropriate selection cut. Once the projections are taken, distributions of each cut for the signal and the background region are normalized by their number of entries and compared. Moreover the integral of the distributions as a function of the cut value is investigated to check the fraction of the signal and background removed for each value of the cut. During this process we keep the transverse momentum of the respective V^0 to be $0.5 < p_T^{V^0} < 12$ GeV/c and assume that the selection cuts are independent of the transverse momentum .The whole procedure can be explained as follows:

1. From the two dimensional histogram, plot and then fit (as described in Chapter 4.3.1) the invariant mass distribution on the y-axis and take the value of the σ and the mean (μ) of the peak distribution.

2. Cut the candidate V^0 in the y-axis, in a 6σ-wide region around μ, then plot the one dimensional projection of $[\mu\text{-}6\sigma,\mu\text{+}6\sigma]$ on the y-axis along the x-axis. This is the required distribution of the topological cut in the signal region.

3. Cut the background V^0 on the y-axis, in $[\mu\text{-}12\sigma,\mu\text{-}6\sigma]$ and $[\mu\text{+}6\sigma,\mu\text{+}12\sigma]$

regions and plot the one dimensional projections on the y-axis along the x-axis. This is the required distribution of the background region.

4. Normalize the distribution for each cut value to compare the signal and background regions.

5. Find the fraction of the signal and background removed for each cut value in the distributions. This plot is most useful when deciding the default and systematic cuts, since we can directly read the percentage of the signal or background removed for a particular value of the cut.

6. Repeat the procedure for K^0_S, Λ and $\bar{\Lambda}$.

In this section we only show the distributions and projections for K^0_S. The distributions and projections for Λ and $\bar{\Lambda}$ will be in Appendix D.

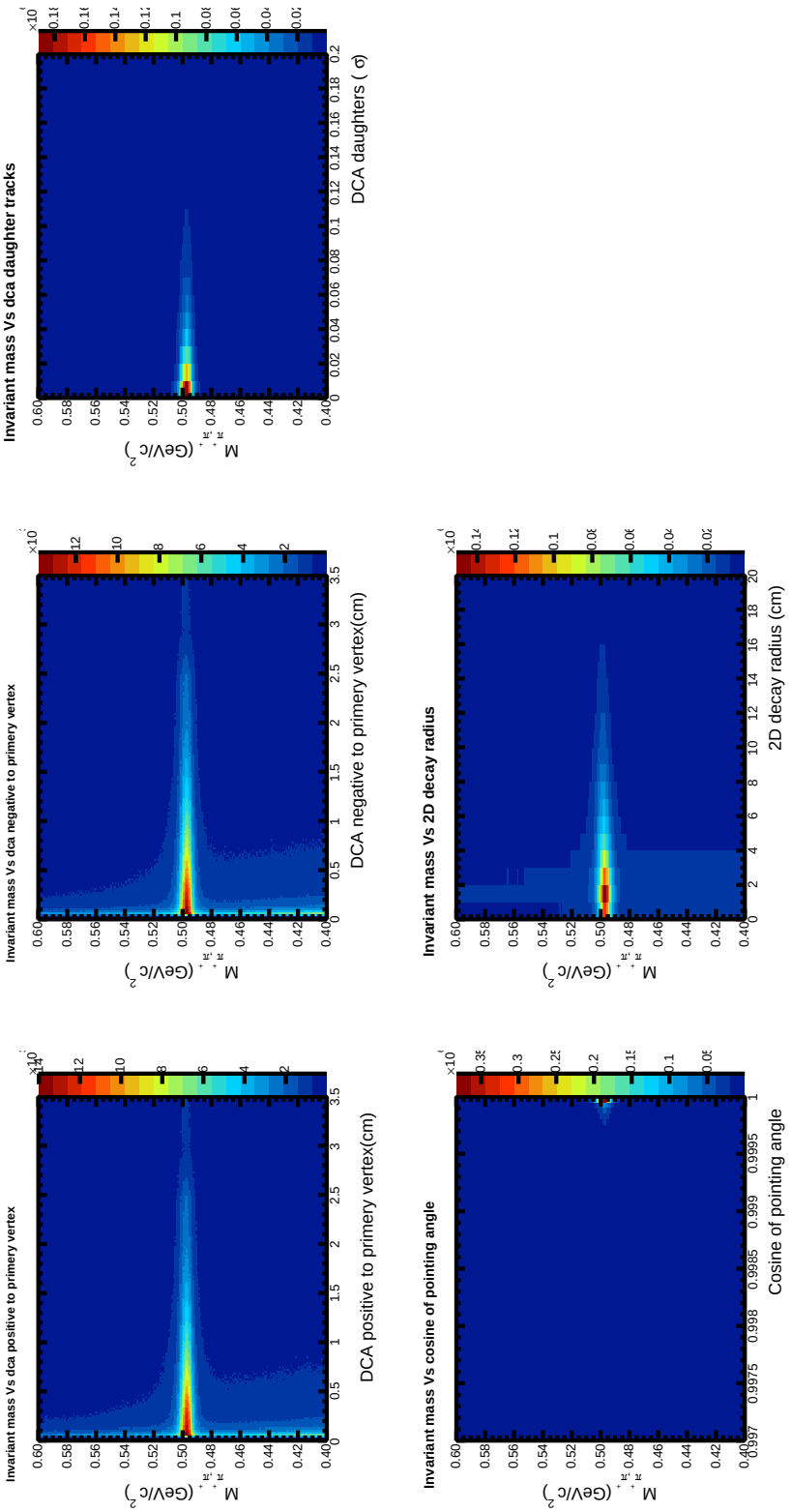

Figure 6.1: Two dimensional distribution of applied topological cuts vs invariant mass for K^0_S.

Distributions for each topological selection are shown in the following figures.

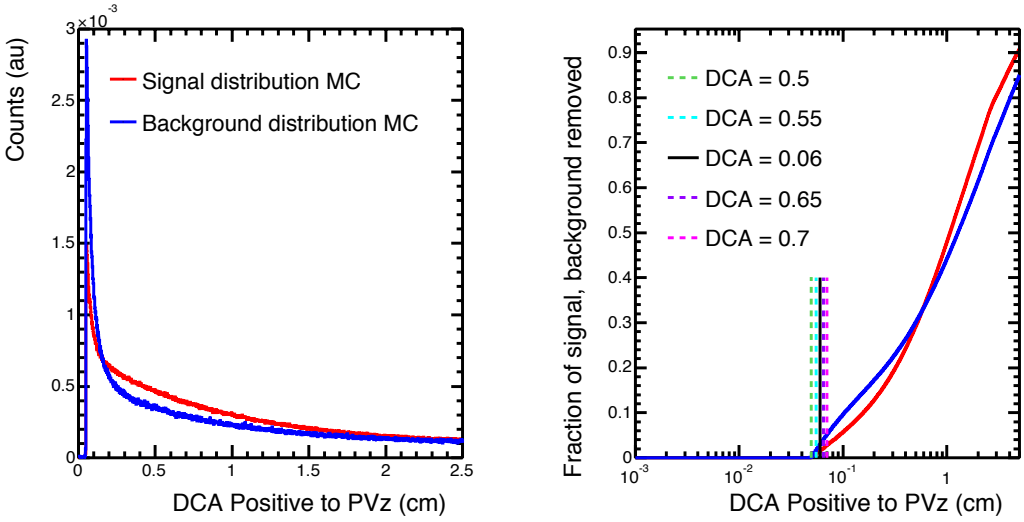

(a) DCA positive to PV_z.

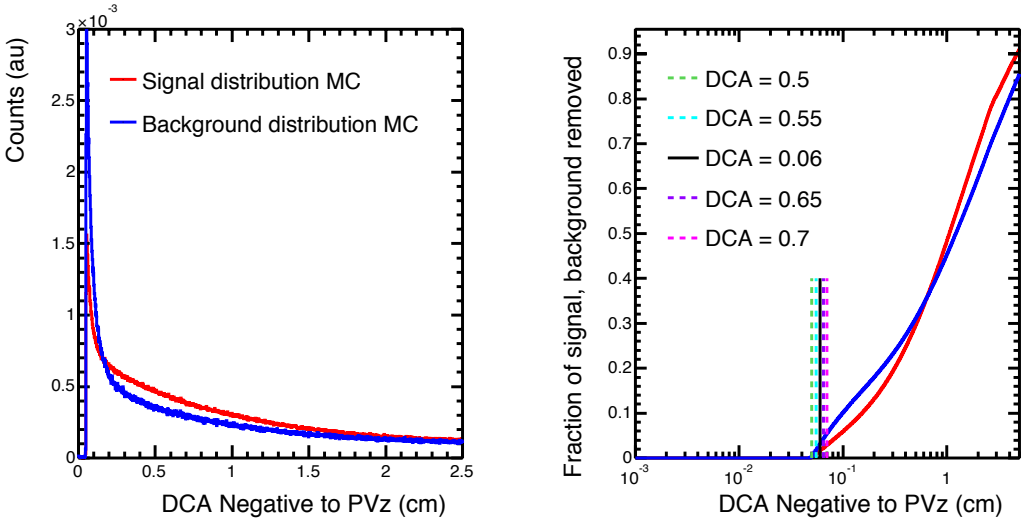

(b) DCA negative to PV_z.

Figure 6.2: DCA positive and negative to PV_z for K^0_S.

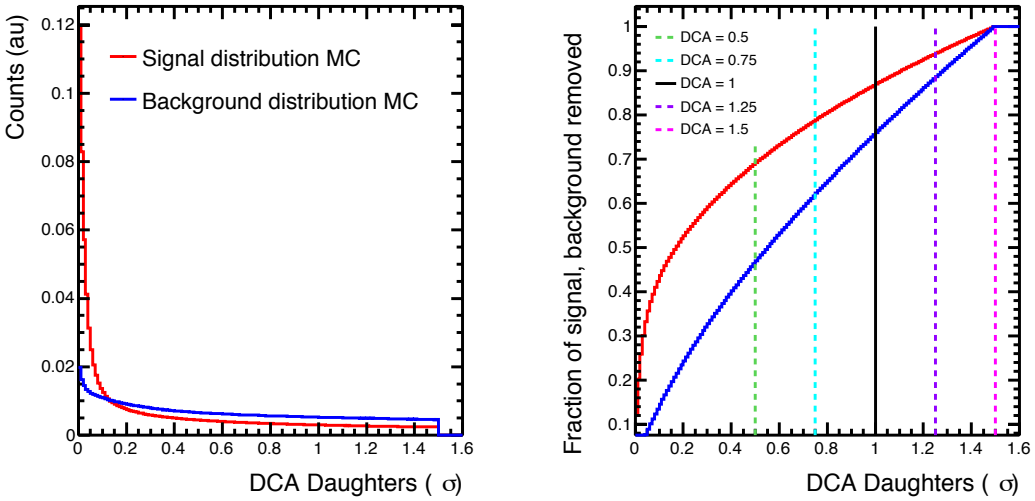

(a) DCA K^0_S daughters to PV_z.

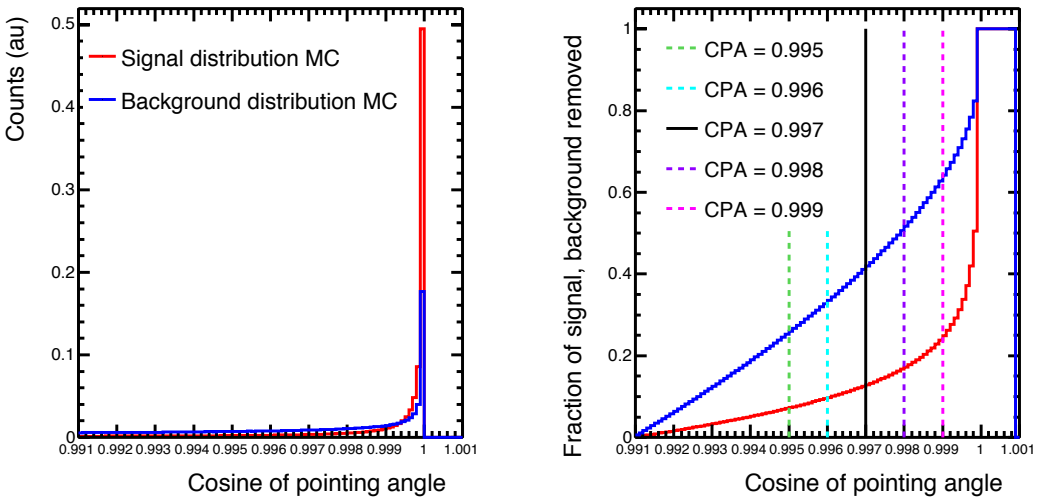

(b) DCA K^0_S cosine of pointing angle.

Figure 6.3: DCA daughters and cosine of pointing angle for K^0_S.

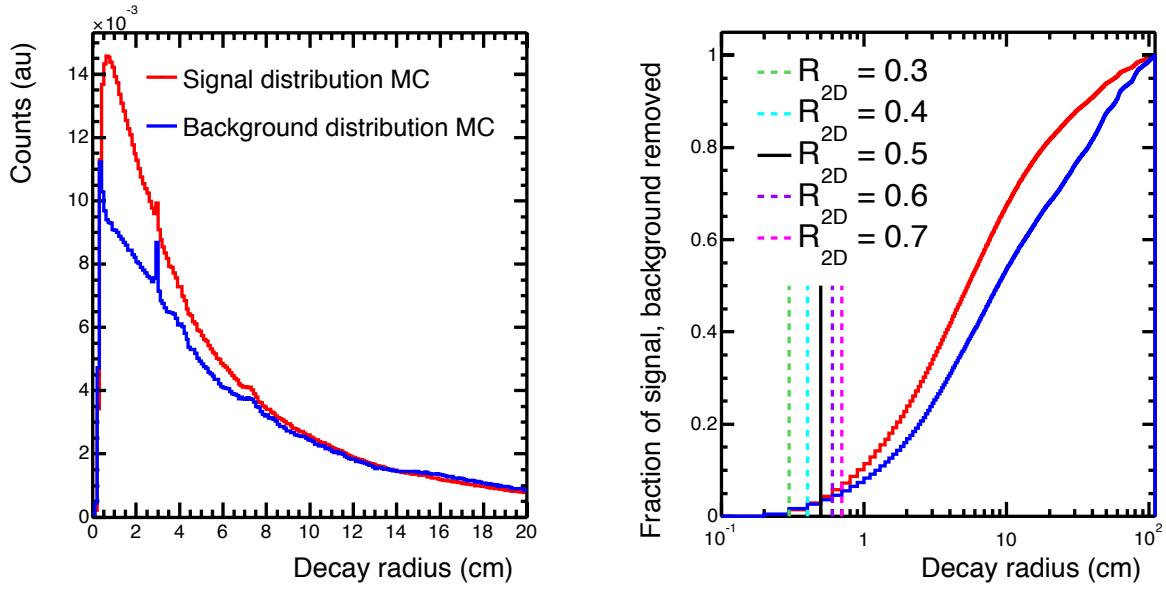

Figure 6.4: K^0_S decay radius.

In Figures 6.2-6.4 the left figure shows the normalized signal and background distributions, while the right figure is the fraction of candidates and backgrounds removed for each value of the cut. Red is for the signal region and blue is for the background region. The vertical dashed lines shows the default and systematic cuts selected in this analysis. Once the integral signal and combinatorial background distributions in Monte Carlo have been obtained we can select the nominal cuts as shown in Figures 6.2-6.4. The nominal selection cut value is selected only if it removes 5% of the signal or less for DCA positive and negative to PV_z and decay radius cut (removes 5% of the background). For DCA daughters to PV_z and for cosine of pointing angle we allowed the removal of 12% of the signal by removing 23% and 41% background respectively. For each topological

selection this is illustrated as the black solid line in the right panels of Figures 6.2-6.4. One special cut is the DCA between two daughter tracks. The integral distribution shows that the nominal cut removes 80% of the signal distribution, but this cut is a upper bound cut: therefore, we select all candidates below this nominal cut while the other four cuts are minimum bound cuts where we select all candidates greater than the nominal value. The other vertical lines show the cut values selected to investigate the systematic behavior of the final results. Each cut is tightened and loosened allowing the signal to change from less than 10% of the nominal cut values. The respective systematic cut values are shown in colored dashed lines. Once this QA procedure is done for K^0_S, Λ and $\bar{\Lambda}$ we need to check that the Monte Carlo distributions reproduced the real data distributions. This crosscheck is an important step in the analysis procedure. If incompatible fractions of signal are removed both in experimental data and in the MC for each of the cuts applied, it will bias the final results when applying the reconstruction efficiency correction. In Figures 6.5-6.7 we plot the respective Monte Carlo and real data distributions for signal region and background region. The left plot is for the signal region and the right plot is for the background region, respectively. The green line shows the Monte Carlo data while the black line shows the real data, in each plot colored dashed lines show the default and systematic selection cuts applied in the final analysis.

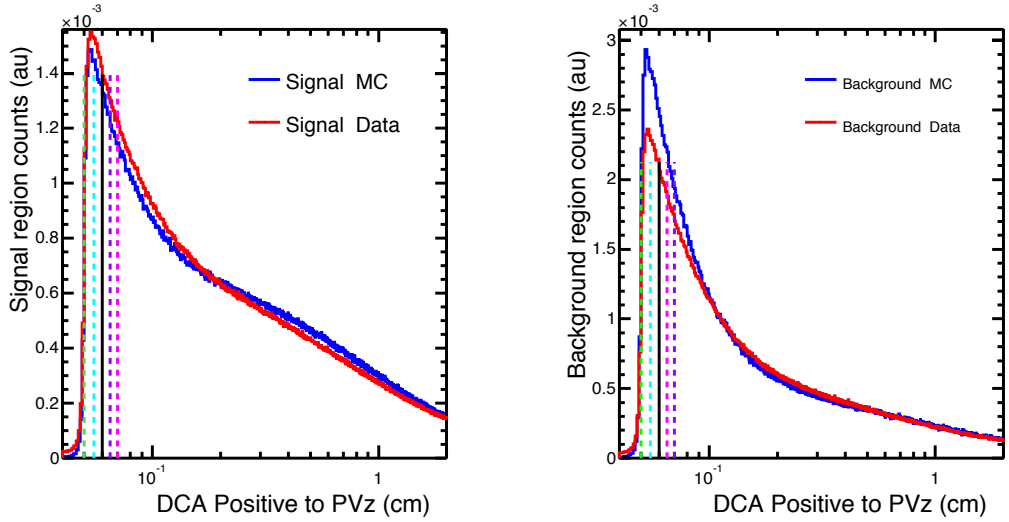

(a) DCA positive to PV_z for K^0_S real and MC data in signal (left) and background region (right).

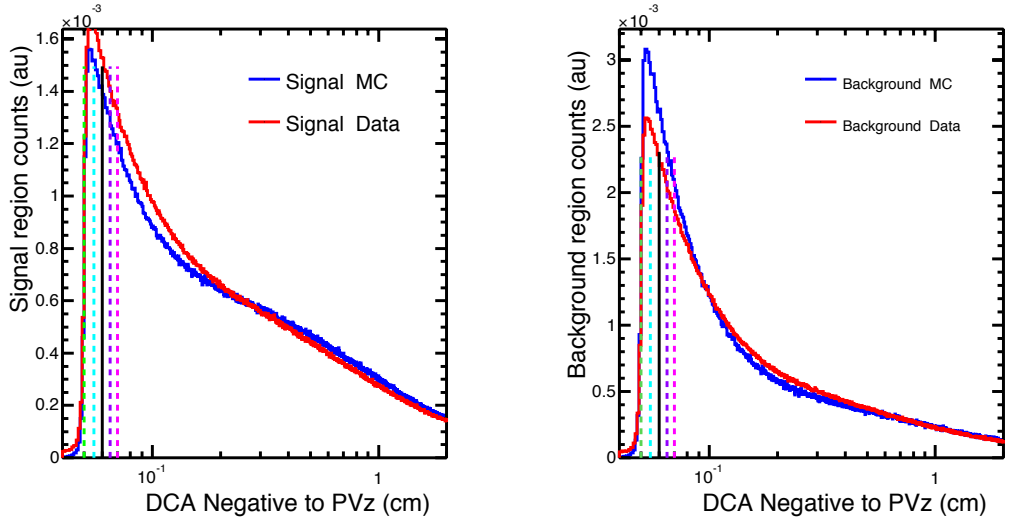

(b) DCA negative to PV_z for K^0_S real and MC data in signal (left) and background region (right).

Figure 6.5: DCA positive and negative to PV_z for K^0_S real and MC.

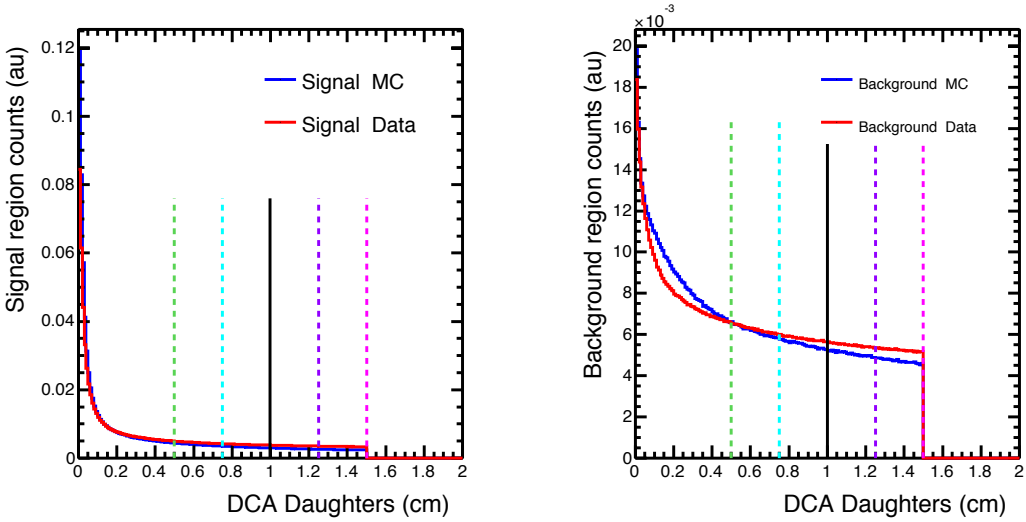

(a) DCA daughters for K^0_S real and MC data in signal (left) and background region (right).

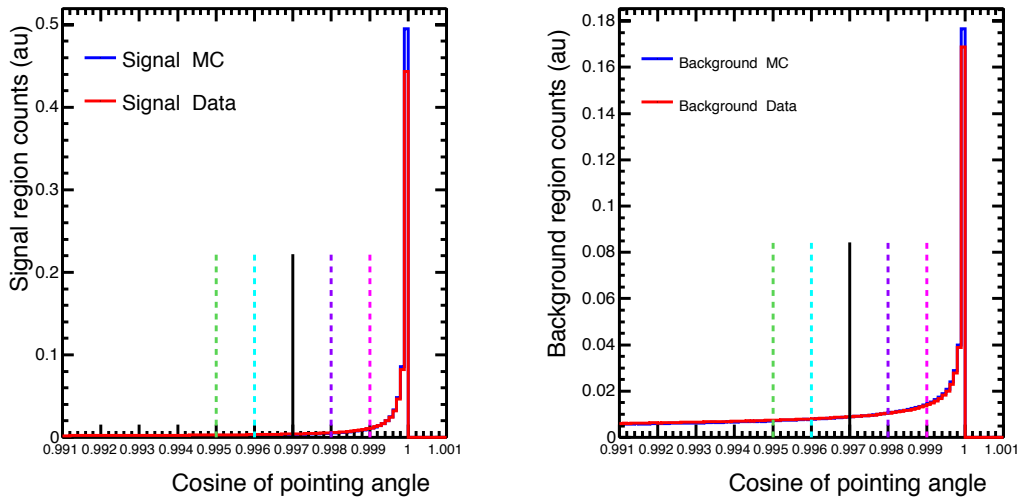

(b) Cosine of pointing angle for K^0_S real and MC data in signal (left) and background region (right).

Figure 6.6: DCA daughters and pointing angle for K^0_S real and MC.

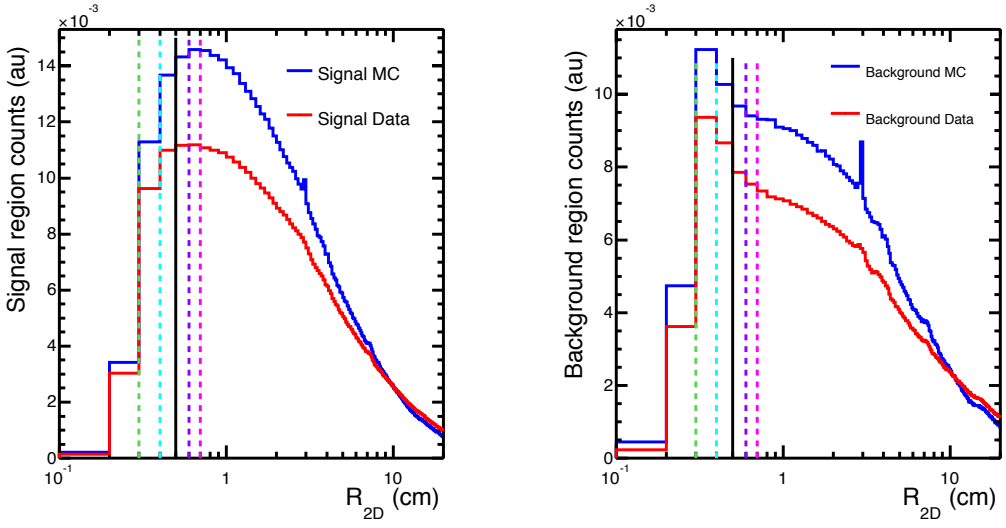

Figure 6.7: Decay radius for K^0_S real and MC data in signal (left) and background region (right).

Note that in the above plots we can infer that the simulation reasonably reproduces the observed behavior in the real data. It is obvious that none of the cuts were extremely restrictive. Once it is confirmed that the Monte Carlo reproduces the reconstructed data we regrouped our selection cuts into five groups ranging from very loose to very tight. In each group we consider the V^0 to be a candidate if, and only if, all five selection cuts have satisfied the logical AND condition. The five groups are shown in Table 6.1.

Selection	Very Loose	Loose	Default	Tight	Very Tight
Decay radius ($2D$) (cm)	> 0.3	> 0.4	> 0.5	> 0.6	> 0.7
Cosine of K^0_S	> 0.995	> 0.996	> 0.997	> 0.998	> 0.999
Cosine of $\Lambda, \bar{\Lambda}$	> 0.993	> 0.994	> 0.995	> 0.996	> 0.997
DCA V0 Daughters (σ)	< 1.5	< 1.25	< 1	< 0.75	< 0.5
DCA Negative to PVz (cm)	> 0.05	> 0.055	> 0.06	> 0.065	> 0.07
DCA Positive to PVz (cm)	> 0.05	> 0.055	> 0.06	> 0.065	> 0.07

Table 6.1: Different V0 selection cuts used for systematic study.

We expect that for very loose cuts, signal and reconstruction efficiency is higher than for loose cuts and for the tight cuts, etc. Finally for very tight cuts we should observe the minimum signal and reconstruction efficiency. This is shown in Figure 6.8 and 6.9 by comparing the invariant mass distribution and reconstruction efficiency for each group. Reconstruction efficiency is maximum in the 'Very Loose selection' and minimum in the 'Very Tight' selection.

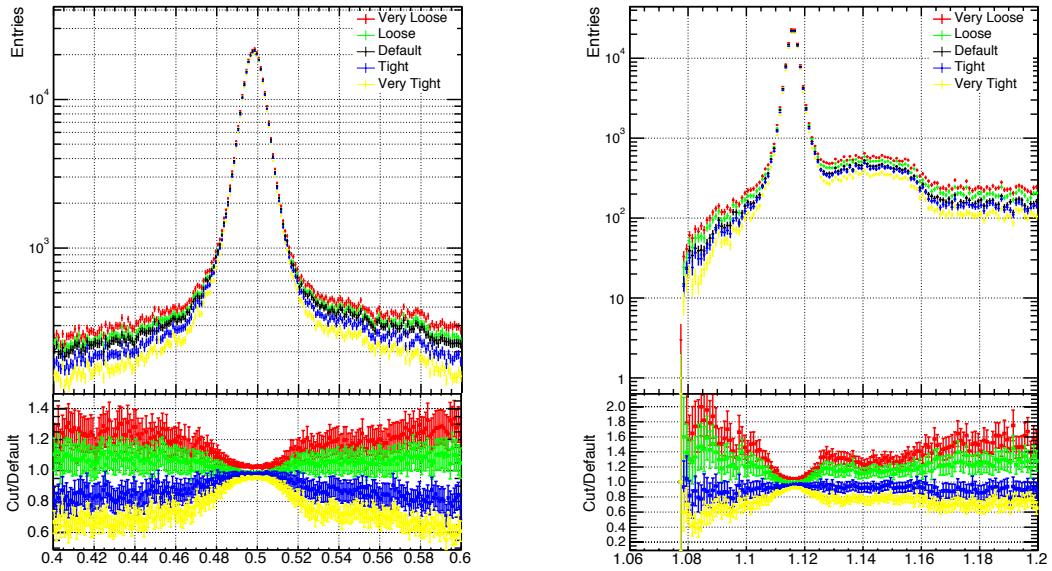

Figure 6.8: K^0_S and Λ mass variation due to different topological selections.

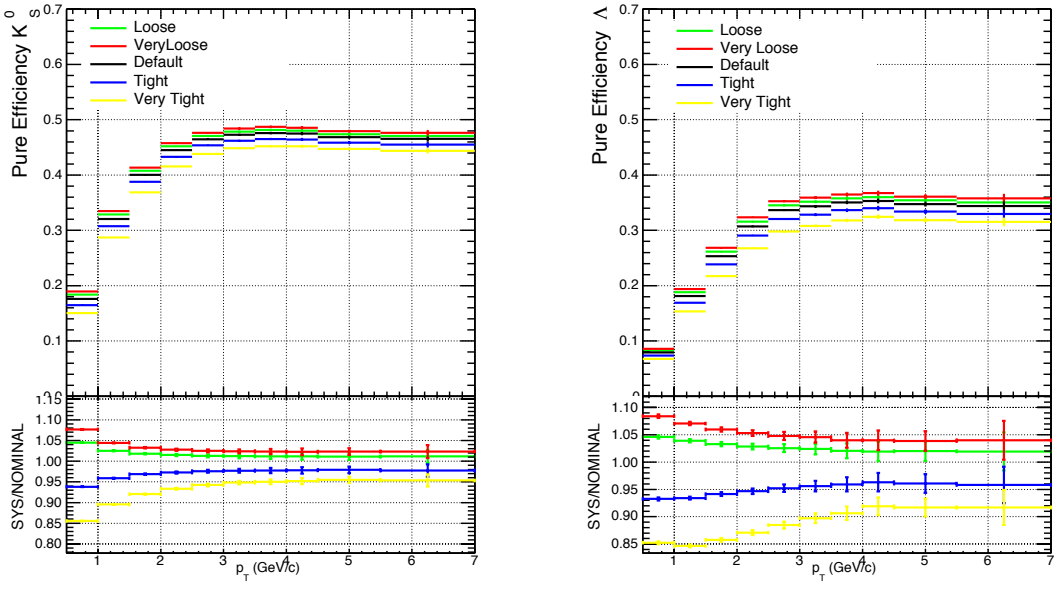

Figure 6.9: K^0_S and Λ reconstruction efficiency variation due to different topological selections.

To evaluate the systematic uncertainty due to topological selections, we must study how each of the points of our transverse momentum spectra in the near-, away-side and underlying region deviates, and then combine these variations to obtain the final systematic error. The procedure used for this task is explained in the following bullet points.

1. First we vary the values of each topological cut from very loose to very tight, keeping the other variables constant.

2. We recalculate the reconstruction efficiency for each systematic selection and obtain the corrected transverse momentum spectra in the near-, away-side and underlying region.

3. We observe how each point in our transverse momentum spectra in the near-, away-side and underlying region ranges from the default topological selection level.

4. We calculate the weighted standard deviation as the systematic uncertainty in each momentum bin based on the following equation 6.1.

$$\sigma = \sqrt{\frac{\sum_{i=1}^{4}(x_N - X_i)^2.X_i}{\sum_{i=1}^{4} X_i}} \tag{6.1}$$

   Where X_N is the default value and X_i is the systematic value in a given momentum bin.

5. Deviations calculated in the previous step were check for the statistical significance by using the Roger Barlow criterion as follows [167] :

$$\sigma_{RB} = (Y_{default} - Y_{sys})/\sqrt{|\sigma_{default} - \sigma_{sys}|} \geq 2 \tag{6.2}$$

Where $Y_{default}$ is the default yield and Y_{sys} is the yield after a particular systematic variation in a given momentum bin and $\sigma_{default}$ is the default statistical error and σ_{sys} is the statistical error after a particular systematic variation in a given momentum bin. If the calculated Roger Barlow sigma (σ_{RB}) is less than 2 we ignore that cut by assuming the relative change is not solely a systematic effect, but also a statistical effect.

In the following Figures 6.10-6.12 we show the corrected spectra in each region for different topological cut set and the relative change in the per trigger yields for K^0_S (right) and $\Lambda + \bar{\Lambda}$ (left).

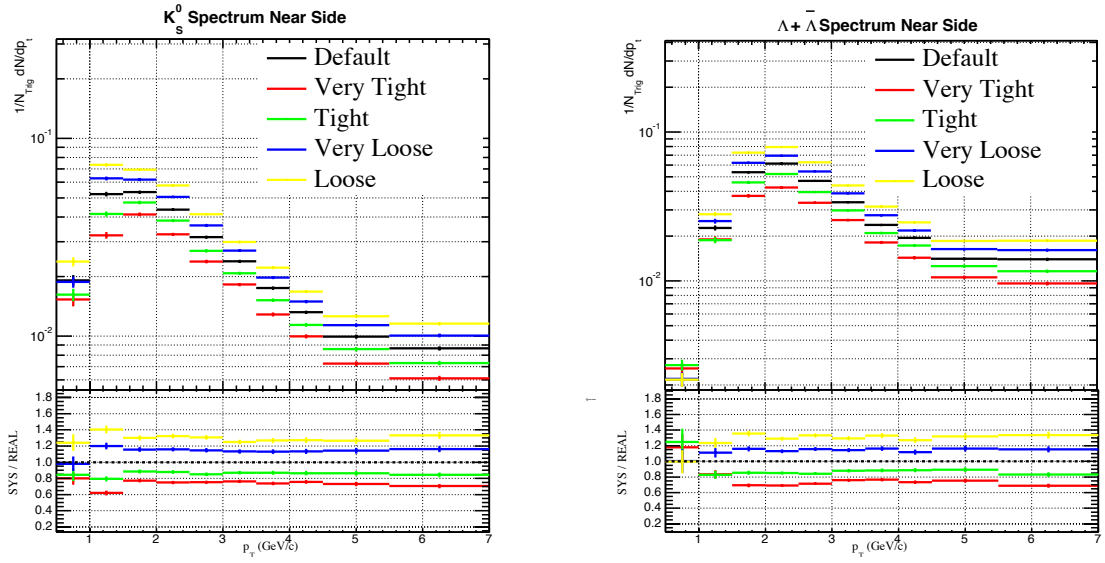

Figure 6.10: K^0_S and Λ+$\bar{\Lambda}$ corrected p_T near side spectrum for different topological selections.

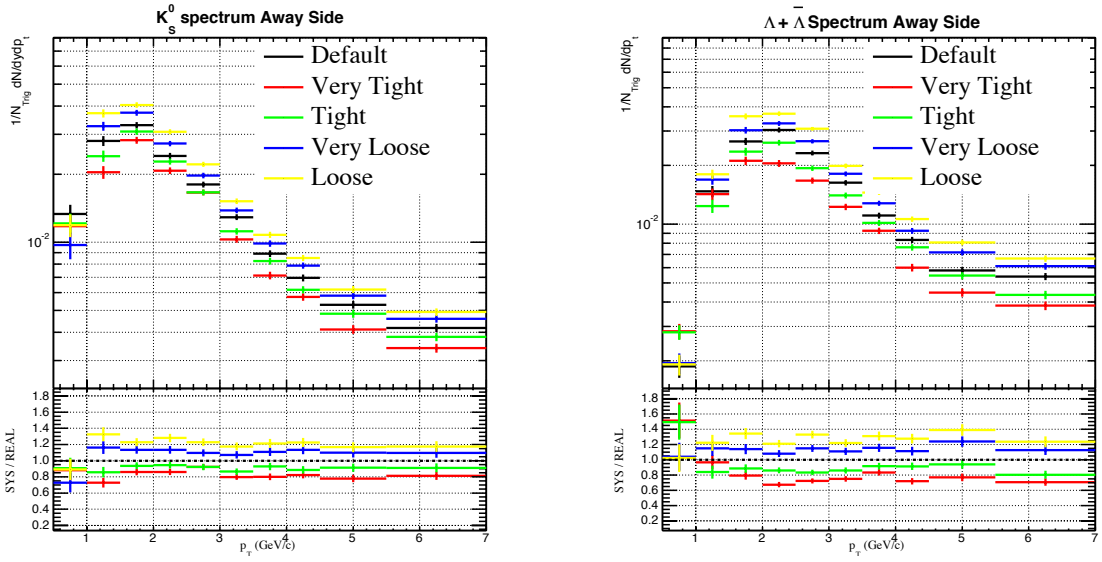

Figure 6.11: K^0_S and $\Lambda + \bar{\Lambda}$ corrected p_T away side spectrum for different topological selections.

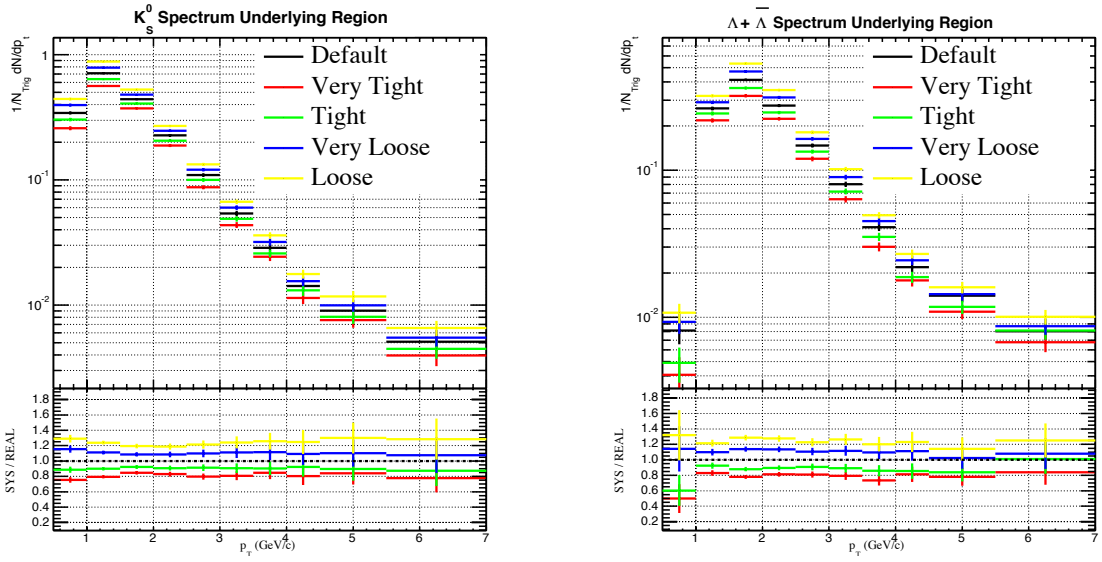

Figure 6.12: K^0_S and $\Lambda + \bar{\Lambda}$ corrected p_T underlying region spectrum for different topological selections.

In this section we detailed the whole procedure for estimating the systematic uncertainty for different topological cuts. In the following we describe only the selection cut variations for the other systematic sources by following all of the above steps one by one, and only the final point-by-point systematic uncertainties are reported in Figures 6.17-6.19.

6.2 Other sources of systematic uncertainty

As explain in Chapter 4, there are other selection cuts we used to remove the combinatorial background. In the following sections we describe the stability of the final results when changing these selection cuts.

6.2.1 TPC number of crossed rows and ratio of crossed rows over findable clusters

When selecting daughter tracks of V^0 decays we chose trajectories that have at least 70 detection points in the TPC. As shown on the right hand side of Figure 6.13 variations in the TPC operating voltage can affect the signal in TPC pads, which ultimately leads to variations between data and Monte Carlo. Thus we use a very loose cut of 70 clusters out of 160 total pads available. By allowing the TPC cluster count to vary between 60 and 80 we determined a systematic uncertainty that changes the signal from the default value by a few percent. Similarly, we tightened the ratio between crossed rows over the findable clusters to 0.85 and

0.75 from the default value of 0.8. Figure 6.13 shows the data and Monte Carlo comparison of TPC number of crossed rows (right) and ratio of crossed rows over findable clusters (left).

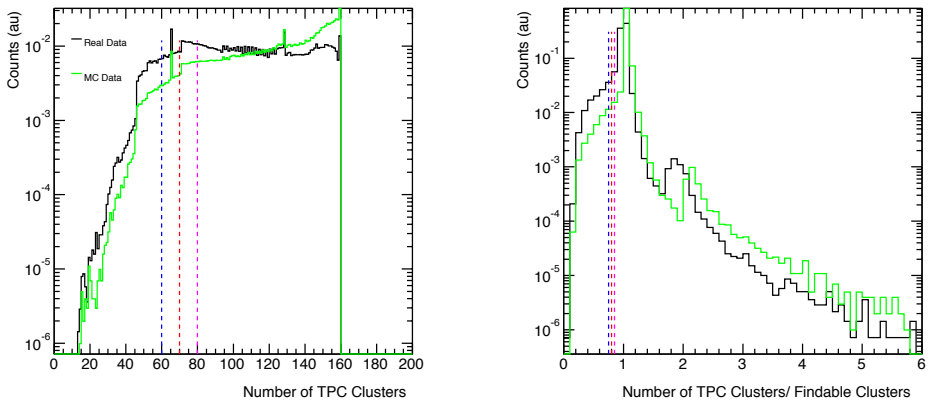

Figure 6.13: Data and Monte Carlo comparison of TPC number of crossed raws (right) and ratio of crossed rows over findable clusters (left).

6.2.2 Identification of daughter particles by an energy loss cut in TPC

For all studied particles (K^0_S, Λ and $\bar{\Lambda}$) a TPC energy loss of cut of 5σ was used for the identification of daughter particles. As explained in the Chapter 4.2.2 this is one of the most valuable cuts, which keeps around 97% of the signal while removing a significant percentage of combinatorial background. Thus It is important to test the effects of a 4σ and 6σ energy loss cut in the TPC. For K^0_S and $\Lambda + \bar{\Lambda}$ in the three different regions we found that the maximum uncertainty is less than

5% for all experimental data points measured. Figure 6.14 shows the TPC signal for Λ (right) and $\bar{\Lambda}$ (left) with a 4σ energy loss cut for all $\pi^+, \pi^-, \bar{p}$ and p. Figure 6.15 shows the TPC signal for Λ (right) and $\bar{\Lambda}$ (left) with a 6σ band kept along all $\pi^+, \pi^-, \bar{p}$ and p.

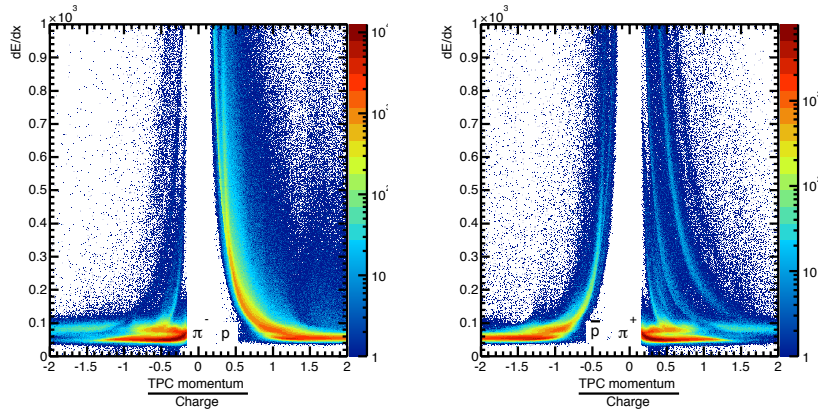

Figure 6.14: TPC signal for Λ (right) and $\bar{\Lambda}$ (left) daughters with 4σ cut.

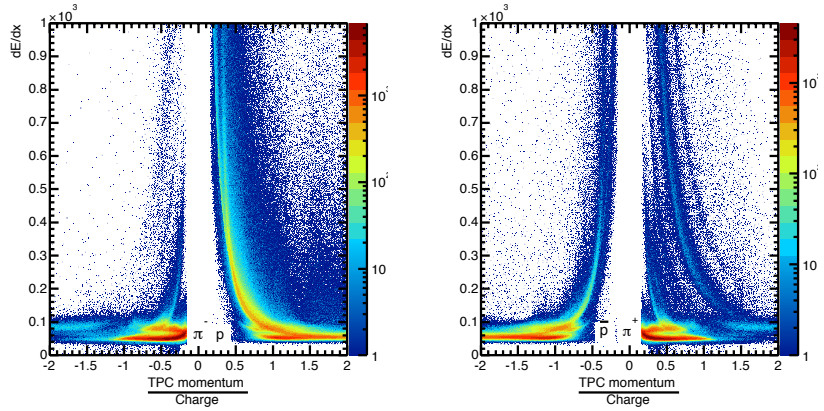

Figure 6.15: TPC signal for Λ (right) and $\bar{\Lambda}$ (left) daughters with 6σ cut.

In both cases the calculated signal loss and gain compared with the default 5σ cut is around 10%.

6.2.3 Systematic uncertainty due to proper lifetime selection

In order to check the stability of the analysis due to the $c\tau$ selection, we redid the analysis for K^0_S for $c\tau < 30$ cm, < 10 cm and for Λ and $\bar{\Lambda}$ with $c\tau < 40$ cm, < 20 cm. The distribution of the proper life time is an exponential and can be written in the particle rest frame with the decay constant λ;

$$Y = Y_0 exp(-\lambda \frac{c\tau}{c\tau_0}) \tag{6.3}$$

Here Y_0 is the initial particle yield and Y is the yield after a proper time τ and τ_0 is the proper life time of the particle in its rest frame. Before selecting the cuts for systematics it is important to check the $c\tau$ distributions for the real and Monte Carlo data as shown in Figure 6.16, where the left figure shows the $c\tau$ distribution for K^0_S and the right figure is for the Λ. It is noted from the figures that the MC reproduced the data well.

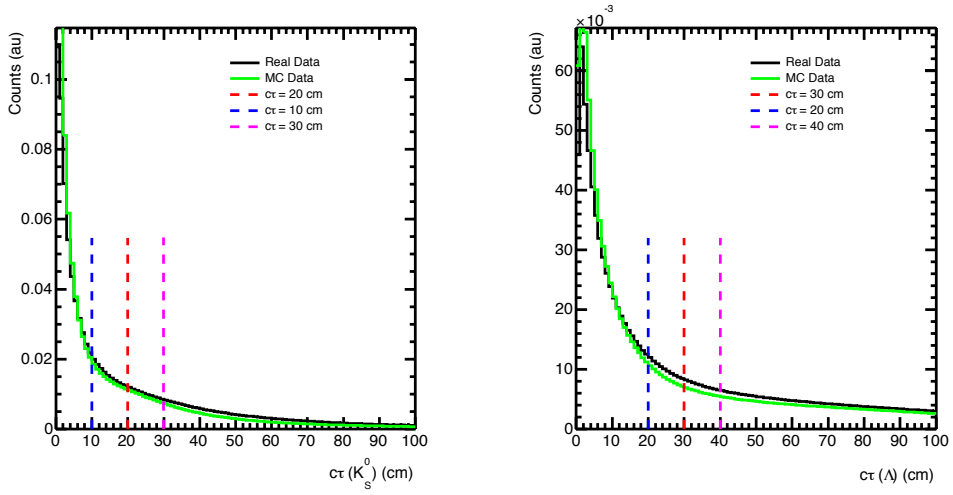

Figure 6.16: $c\tau$ distributions for the real and Monte Carlo data for K^0_S (right) and for the Λ (left).

6.2.4 Systematic uncertainty due to signal extraction

The invariant mass cut for the V^0 candidate is by default μ-6σ and μ+6σ. To check the stability we change the signal extraction region from 6σ to 5σ and 7σ. This leads to a systematic uncertainty of less than 5% in all p_T bins considered.

6.3 Summary of the point-by-point uncertainties in p_T

Once all systematic uncertainties have been evaluated, we need to combine them to calculate the final uncertainty in a given bin. The addition of the systematic uncertainties is performed on a bin-by-bin basis in quadrature where

$$\sigma_{Final} = \sqrt{\sigma_1^2 + \sigma_2^2 + \sigma_3^2 + \sigma_4^2 + ..} \tag{6.4}$$

One of the main assumption we make throughout the systematic uncertainty estimation is that the final results of each cut variation are uncorrelated with each other. This will simplify the calculation of final point-by-point systematic uncertainty in all three regions of the correlation function. If one samples enough statistics it is possible to make the final calculation without that assumption and taking into account the full covariance matrix. Figures 6.17, 6.18 and 6.19 report the final point-by-point systematic uncertainty for all three regions for the K^0_S and $\Lambda + \bar{\Lambda}$ transverse momentum spectra.

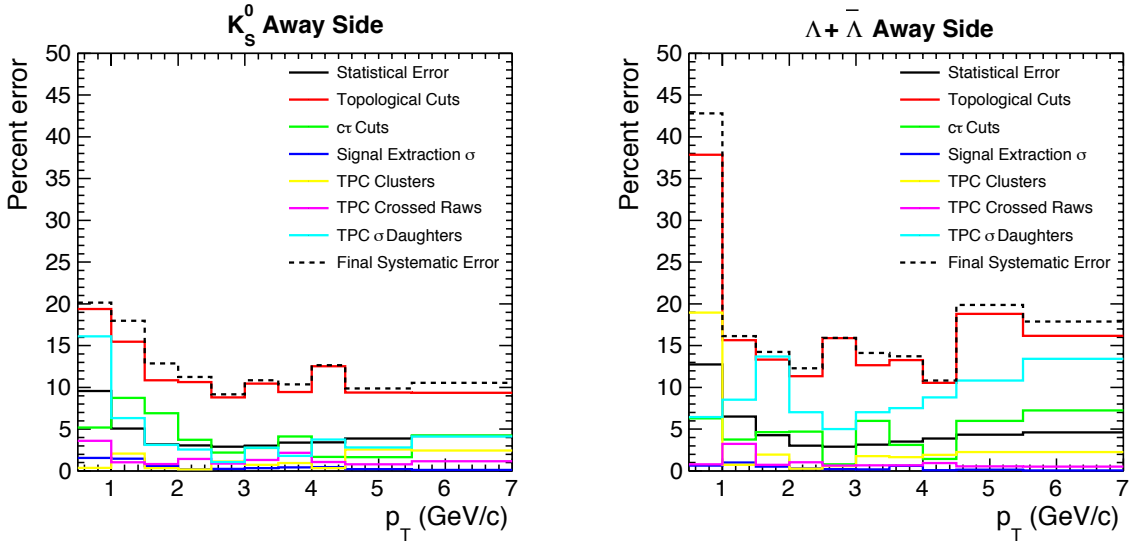

Figure 6.17: K^0_S and $\Lambda + \bar{\Lambda}$ final systematic and statistical uncertainties for away side.

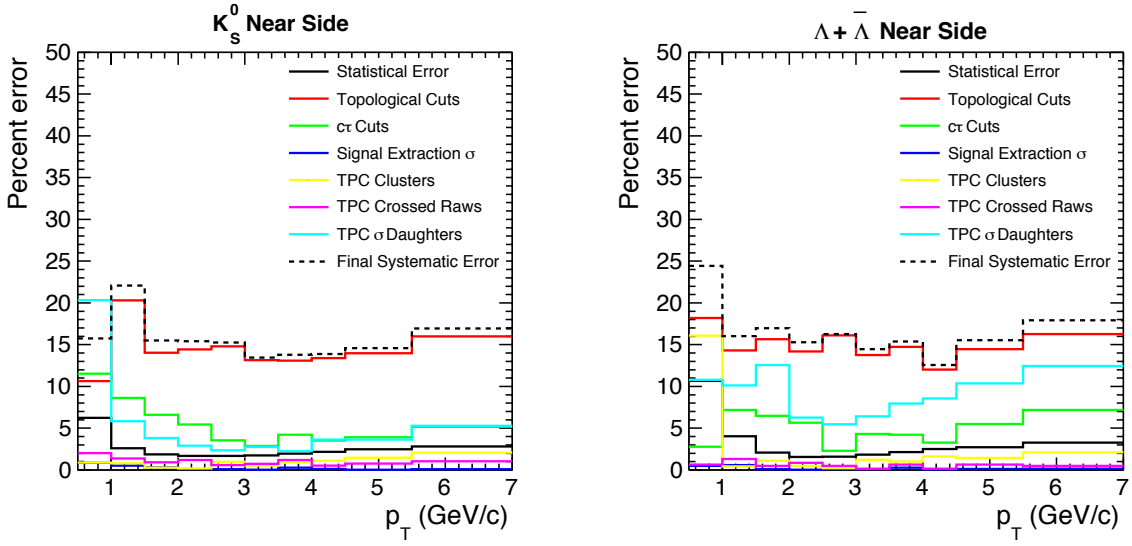

Figure 6.18: K^0_S and $\Lambda + \bar{\Lambda}$ final systematic and statistical uncertainties for near side.

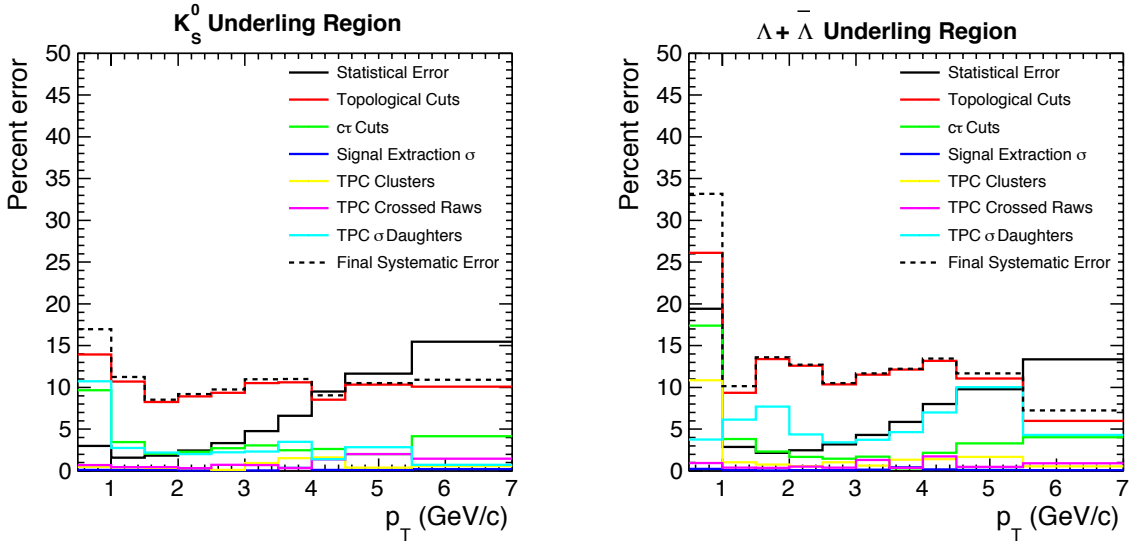

Figure 6.19: K^0_S and $\Lambda + \bar{\Lambda}$ final systematic and statistical uncertainties for underlying region.

Chapter 7

Interpretation of Results

Using the methods described in Chapters 4 and 5 on reconstruction and two particle correlations of associated V^0 particles along with the systematic uncertainties explored in Chapter 6, this chapter will summarize the final results of this analysis. One of the main goals was to characterize V^0 particle production rates in jets and the underlying event in pp collisions. The motivation for this analysis is based on the observation of a significant Λ/K^0_S ratio enhancement in Pb+Pb collisions at intermediate p_T with respect to pp collisions [168]. This Λ/K^0_S enhancement is one of the key observables of QGP formation. Even though no QGP is formed in pp collisions it is important to study the Λ/K^0_S ratio in regions dominated by the hard quark fragmentation process and areas which are influenced by the underling event activity. These results can be used as a baseline of comparison with heavy-ion results and to tune parameters in Monte Carlo event generators, specifically in the underlying event region [169, 170]. More recently the ALICE

collaboration found a significant Λ/K^0_S enhancement at intermediate p_T in p+Pb collisions with respect to pp collisions [171]. Therefore, disentangling the particle production in jet and underlying event structures is an important cross reference.

7.1 Current studies of V^0 production in jets

An alternative method to determine V^0 in jets is already being investigated in ALICE using p+Pb collisions. In that analysis full jet events were reconstructed with an anti-K_T jet algorithm and one counts the V^0s in a defined jet cone with a radius of R=0.4 (0.3, 0.2) cm. If any V^0 satisfied the condition $\Delta R_{jet-V^0} < R_{Jet}$, then the V^0 is considered to be produced inside the jet cone. Here ΔR_{jet-V^0} is the distance between the V^0 and jet axis in η-ϕ plane and R_{Jet} is the radius of the jet cone.

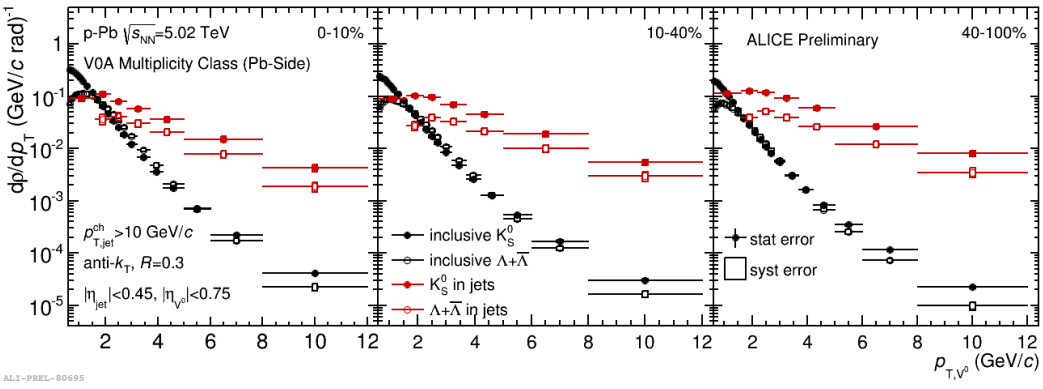

Figure 7.1: p_T spectrum of K^0_S and $\Lambda+\overline{\Lambda}$ in jets in pPb collisions.

Figure 7.1 shows the p_T differential density of K^0_S and Λ ($\overline{\Lambda}$) in jets with

$p_{T,jet}$ >10GeV/c in pPb collisions, with R_{jet}=0.3. It is obvious that the V^0 spectra in jets have a different momentum distribution compared with the inclusive spectra.

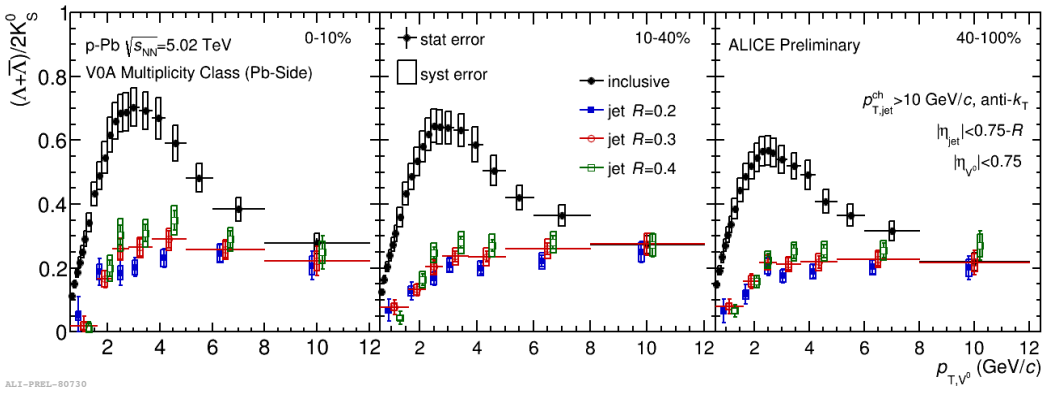

Figure 7.2: Λ/K^0_S ratio in $p_{T,jet}$ >10 GeV/c in three V0A multiplicity classes in pPb collisions.

Figure 7.2 shows the Λ/K^0_S ratio in $p_{T,jet}$ >10 GeV/c in three multiplicity classes in pPb collisions. Jets are reconstructed with the same procedure as described in the Figure 7.1 . In all three cases the Λ/K^0_S ratios in jets are significantly lower than the inclusive ratio. This suggests that the Λ production in jets is significantly lower in the fragmentation process and potentially larger in soft processes, which mimics the inclusive process more. Another key observable is that the Λ/K^0_S ratio in jet regions is not dependent in the multiplicity of the considered events. This means the particle production in jets is not influenced by the energy density of the initial collision.

7.2 $h^{\pm}$-V^0 correlations and V^0 production in jets

The experimental approach in our study is more simple than the one explained in the previous section because it does not require the full jet reconstruction on an event by event basis. Rather we select the highest leading charged track of the event and observe the angular and pseudorapidity distribution of V^0s with respect to the leading track. This type of analysis becomes really effective in Pb+Pb collisions where full jet reconstruction takes lots of computer time and has difficulties disentangling flow and non flow. Figure 7.3 shows the one dimensional azimuthal correlation structures for different p_T intervals of K^0_S particles. The y-axis is $1/N_{Trig}dN/d\Delta\phi$ and the x-axis is $\Delta\phi$. The y-axis represents the 'per trigger' yield for a given $\Delta\phi$ bin after acceptance correction and underlying event subtraction. The prominent peak shape structure at $\Delta\eta,\Delta\phi$=0,0 is due to the clustering of K^0_S around the leading track. This peak is the near-side jet peak. Directly opposite to the near-side jet peak at $\Delta\phi=\pi$ is the away-side jet. It is elongated in $\Delta\eta$ due to momentum conservation. Figure 7.4 shows the one dimensional azimuthal correlation structures for different p_T intervals of $\Lambda+\bar{\Lambda}$ particles in the same leading track momentum interval. An important observation for both particle species is the smooth evolution of the near-side jet peak when increasing the transverse momentum of the associated V^0.

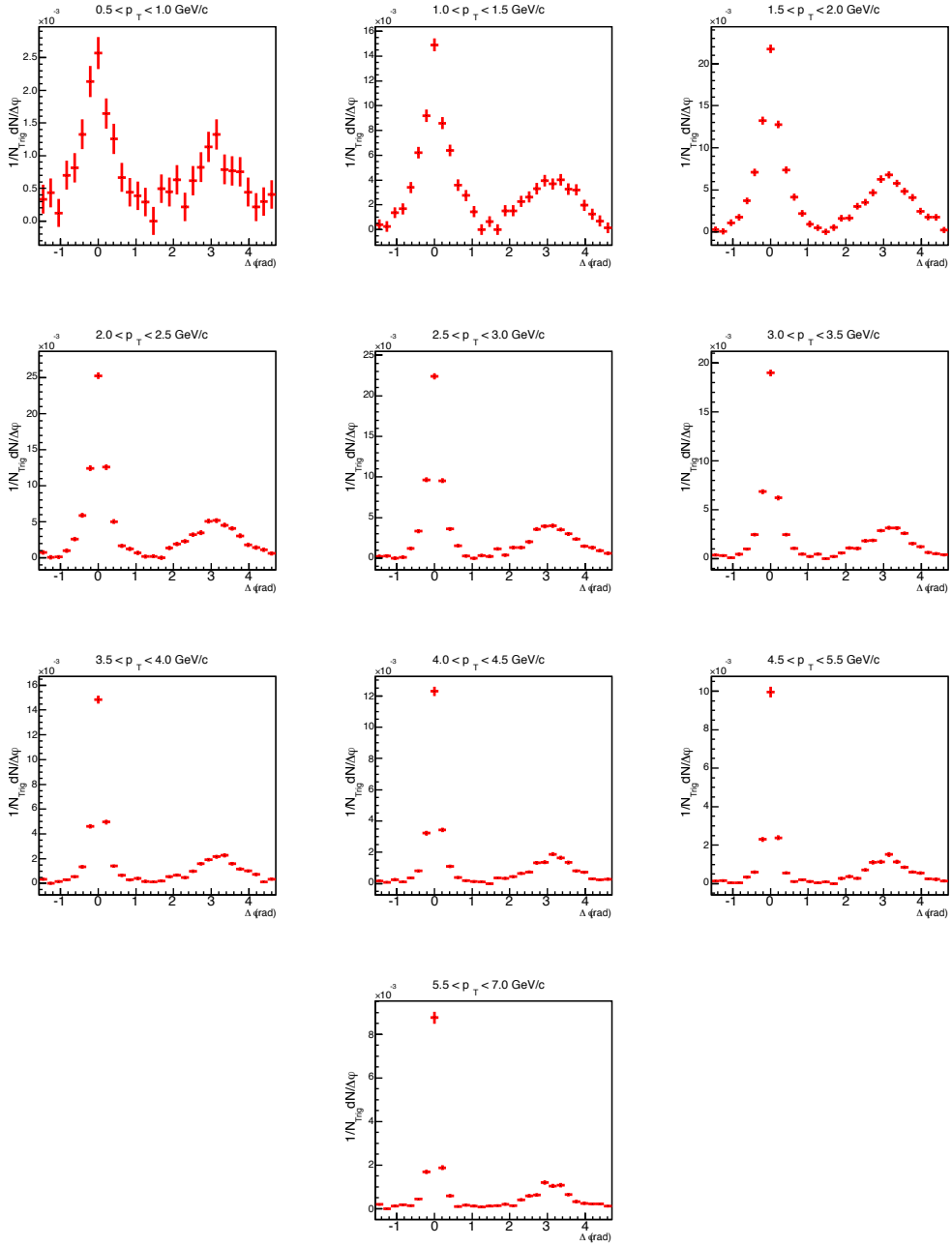

Figure 7.3: One dimensional $\Delta\phi$ correlation structures for K^0_S in ten transverse momentum intervals.

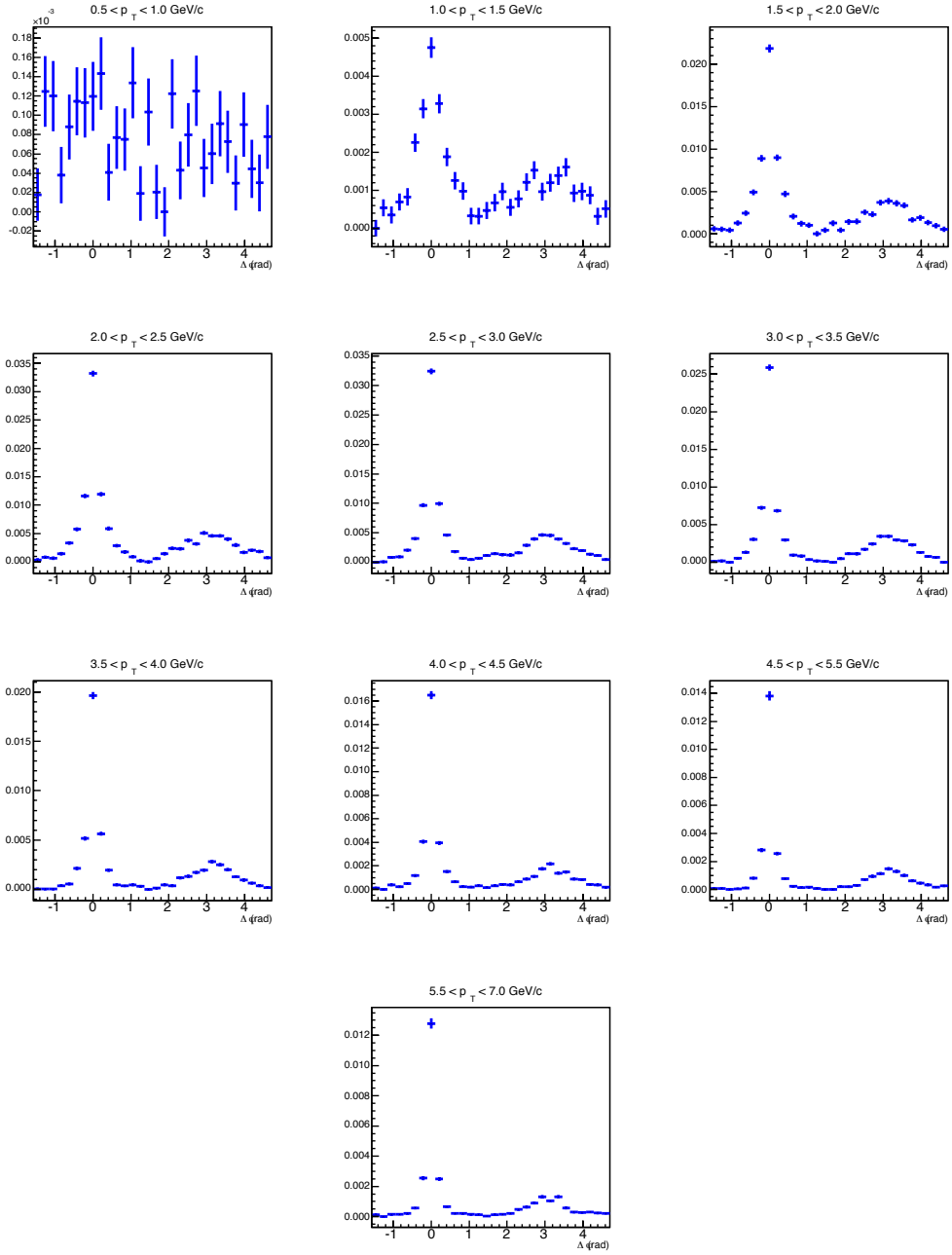

Figure 7.4: One dimensional $\Delta\phi$ correlation structures for Λ+$\bar{\Lambda}$ in ten transverse momentum intervals.

7.3 Gaussian based model fit function to investigate the correlation observables

As explained in Chapter 5.4 we first used a four component fit function to describe the one-dimensional $\Delta\phi$ projections of the two-dimensional $\Delta\eta, \Delta\phi$ correlation structures. This fit function includes two Gaussians to describe the near-side jet peak and one Gaussian to describe the away-side jet peak and a zeroth order polynomial to describe the background pedestal. Figure 7.5 shows the one dimensional $\Delta\phi$ projections in $|\Delta\eta|$ <1 for ten different transverse momentum bins of K^0_S, fitted with the fit function described in Chapter 5.4.1. Each separate component of the fit function is shown in different colors. The contributions from different fit components were illustrated in Figure 5.4.1 in Chapter 5. As one can see in Figure 7.5 a single Gaussian (pink) is not sufficient to describe the near-side jet peak. A narrow Gaussian (green) is required to successfully match the data. The double Gaussian fit is shown in red. Figure 7.6 shows the one dimensional $\Delta\phi$ projections in $|\Delta\eta|$ <1 for ten different transverse momentum bins of $\Lambda+\bar{\Lambda}$. Figures 7.7 and 7.8 shows the one dimensional $\Delta\eta$ projections for ten different momentum bins fitted with a near-side gaussian centered at $\Delta\eta$ =0 with a pedestal for K^0_S and $\Lambda+\bar{\Lambda}$.

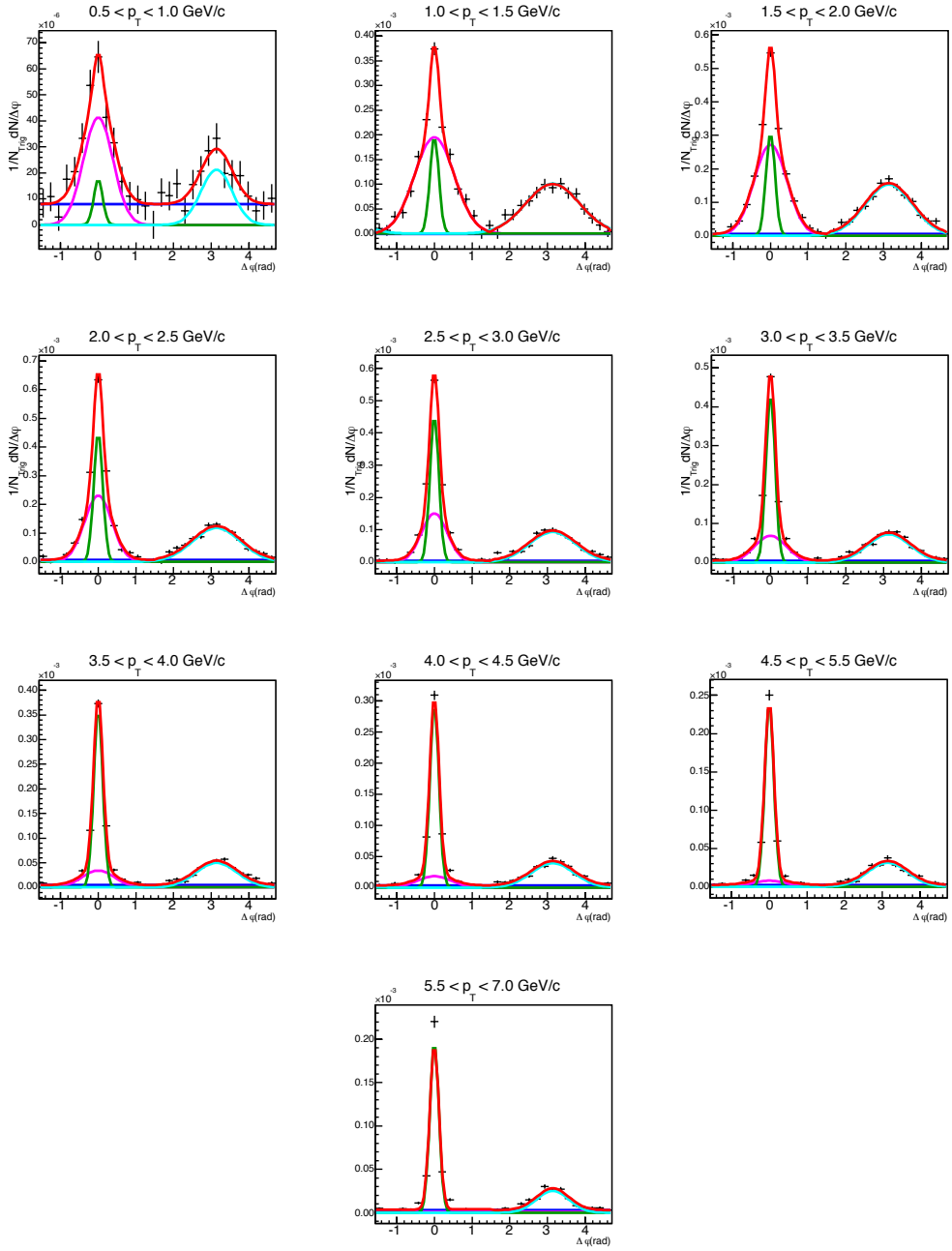

Figure 7.5: One dimensional $\Delta\phi$ projections for K^0_S in ten different momentum bins fitted with two near-side gaussians and one away-side gaussian with a pedestal.

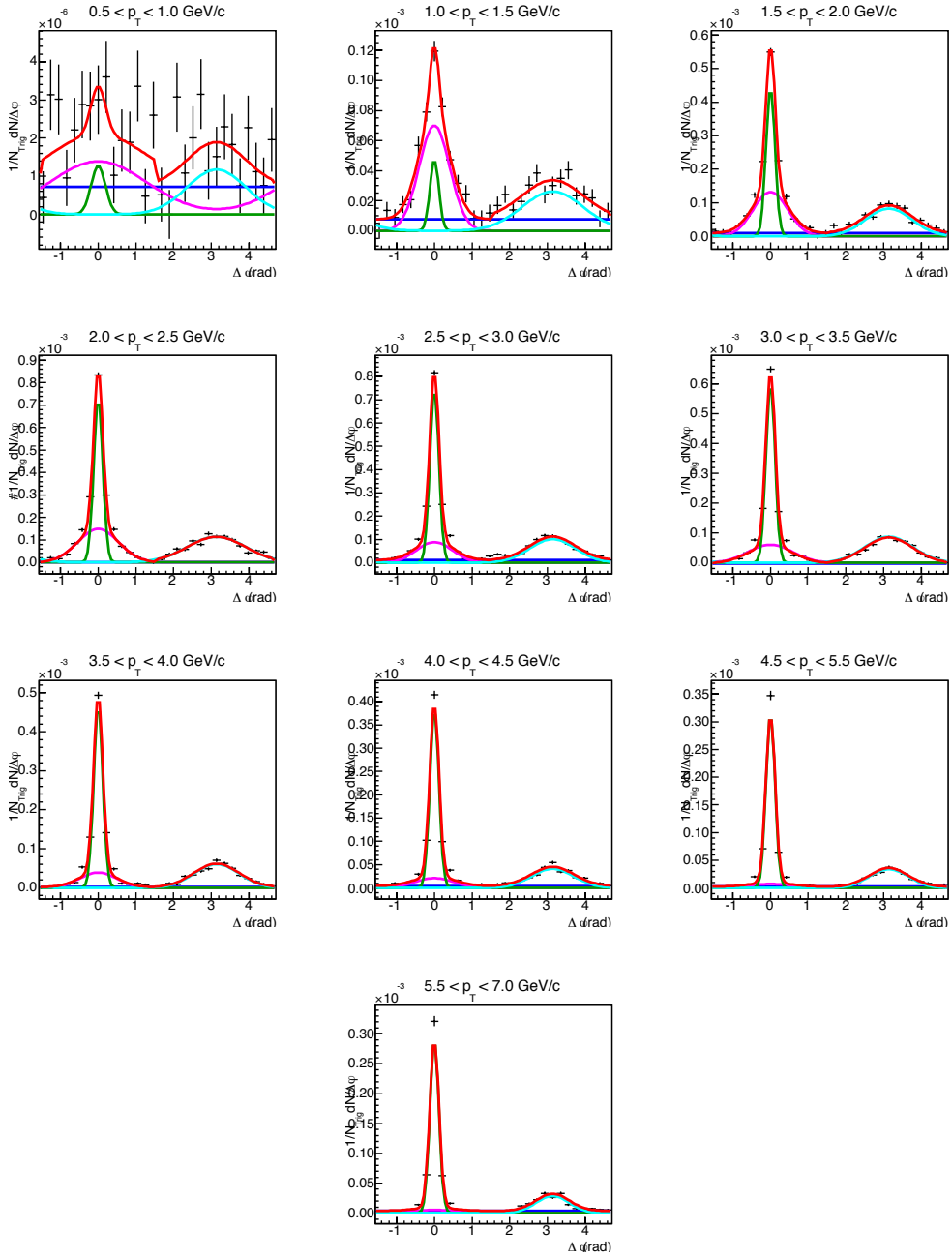

Figure 7.6: One dimensional $\Delta\phi$ projections for Λ+$\bar{\Lambda}$ in ten different momentum bins fitted with two near-side gaussians and one away-side gaussian with a pedestal.

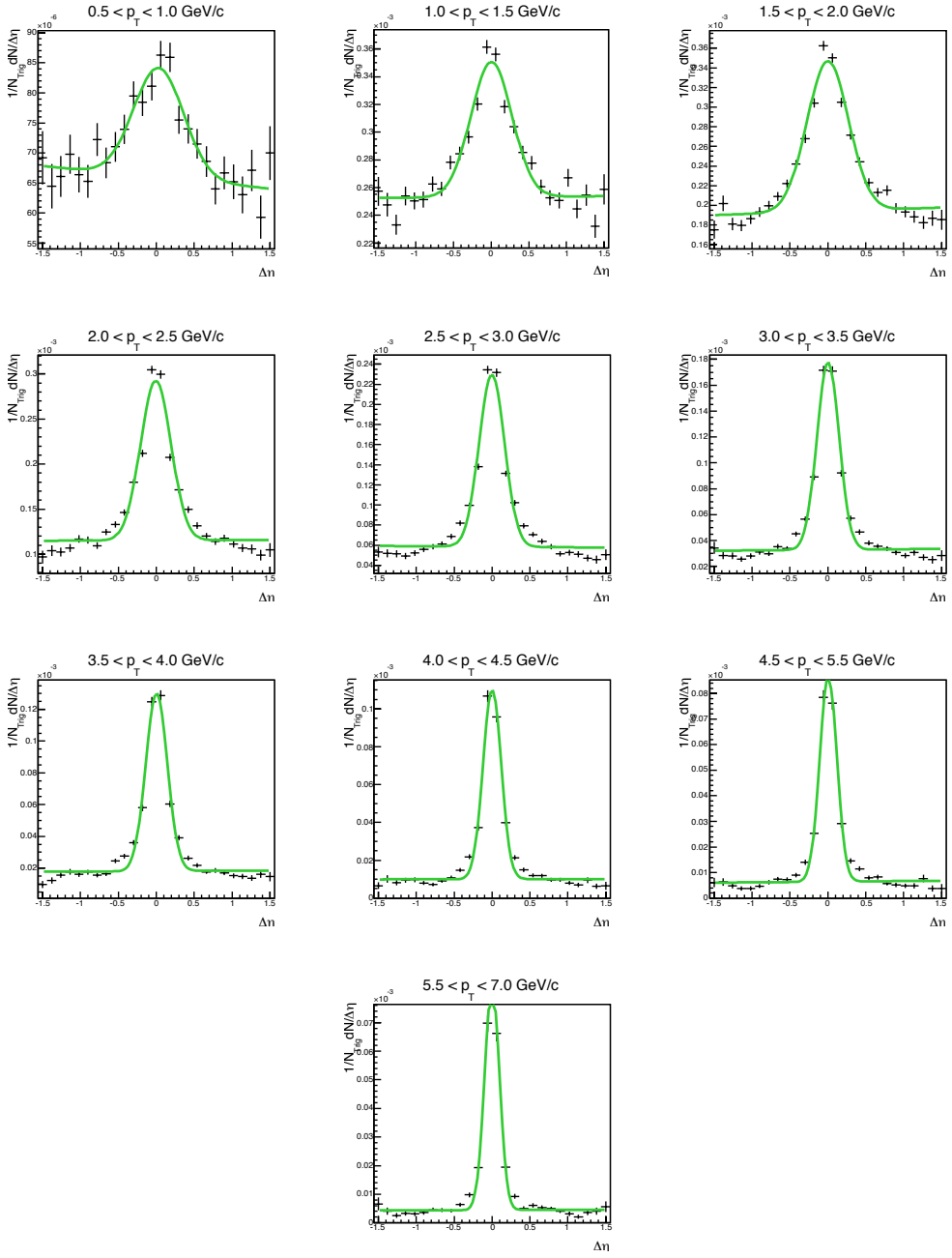

Figure 7.7: One dimensional $\Delta\eta$ projections for K^0_S in ten different momentum bins fitted with a near-side gaussian centered at $\Delta\eta$ =0 with a pedestal.

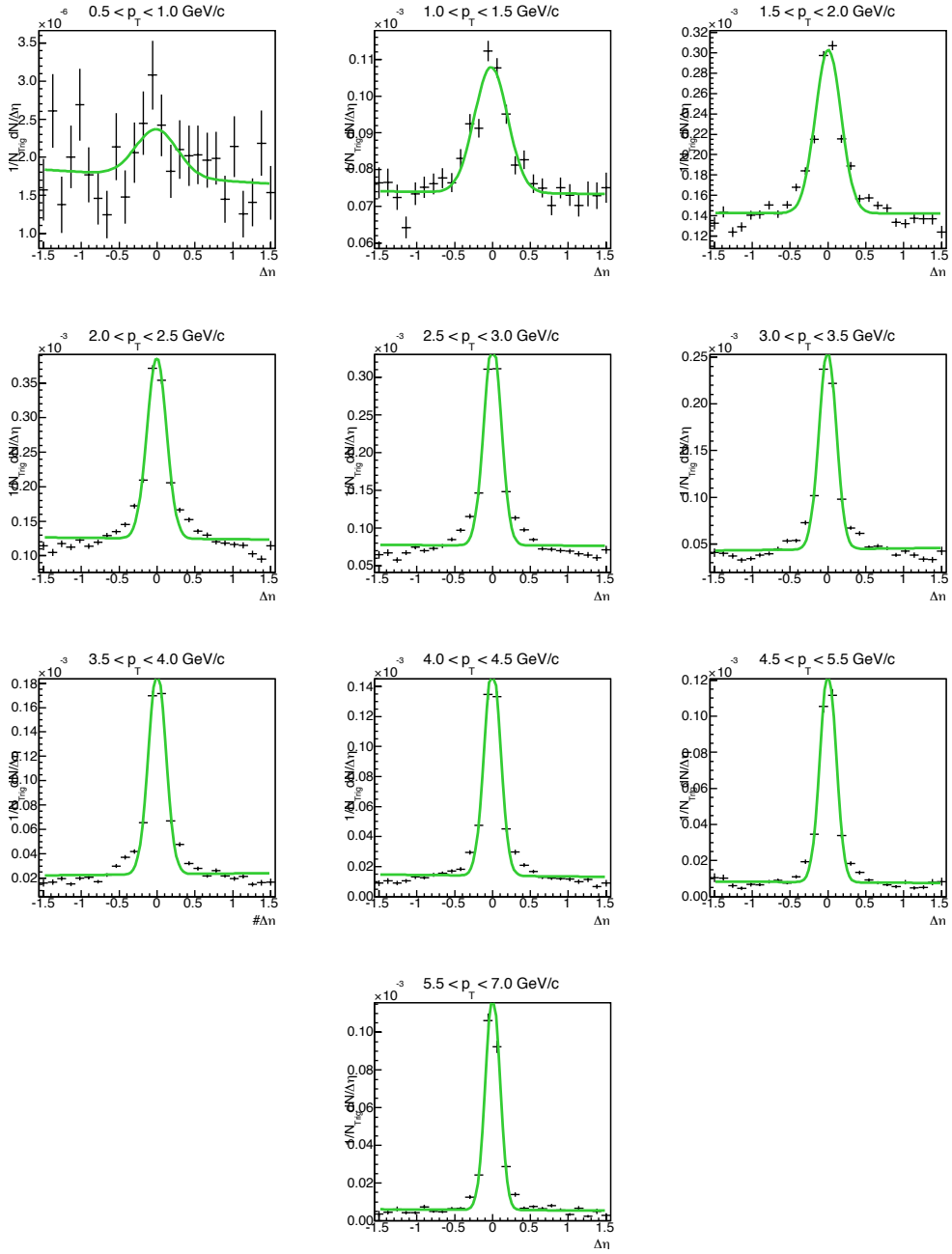

Figure 7.8: One dimensional $\Delta\eta$ projections for Λ+$\bar{\Lambda}$ in ten different momentum bins fitted with a near-side gaussian centered at $\Delta\eta$ =0 with a pedestal.

We can now investigate the fit parameter evolution as a function of associated particle transverse momentum. In Figure 7.9 we show the near-side $\Delta\eta$ (right) and $\Delta\phi$ (left) Gaussian width evolution in different p_T intervals for K^0_S and Λ+$\bar{\Lambda}$. The main observation is the narrowing of $\Delta\phi$ and $\Delta\eta$ width with increasing p_T. At intermidiate p_T a clear difference of $\Delta\phi$ and $\Delta\eta$ can be observed for baryons and mesons. The $\Delta\eta$ width for $p_T > 3$ GeV/c for both particles will become equal for baryons and mesons, but $\Delta\phi$ and $\Delta\eta$ never converge to a common width for any particle.

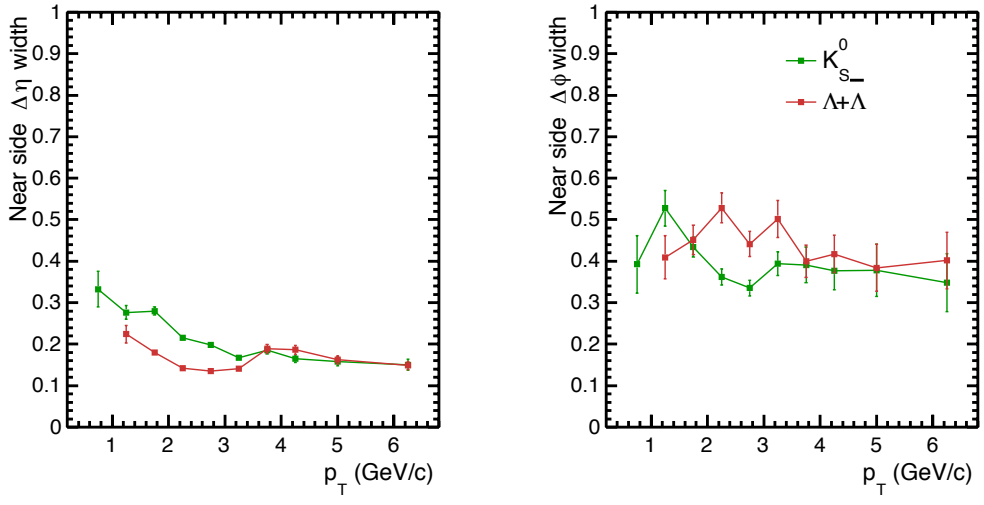

Figure 7.9: near-side $\Delta\eta$ (right) and $\Delta\phi$ (left) gaussian width evolution in different p_T intervals of K^0_S and Λ+$\bar{\Lambda}$.

Another conclusion from this near-side $\Delta\eta$ and $\Delta\phi$ parameter evolution is that both K^0_S and Λ+$\bar{\Lambda}$ are highly correlated with the leading charged track at hight p_T (p_T >3 GeV/c) in the jet fragmentation process, which occurs in a narrow $\Delta\eta$x$\Delta\phi$

space. Figure 7.10 shows the away-side $\Delta\phi$ Gaussian width evolution for different p_T intervals of K^0_S and Λ+$\bar{\Lambda}$. For both particles it is observed that the width is decreasing and both particles share the same $\Delta\phi$ width, which at high p_T is consistent with the same-side $\Delta\phi$ width.

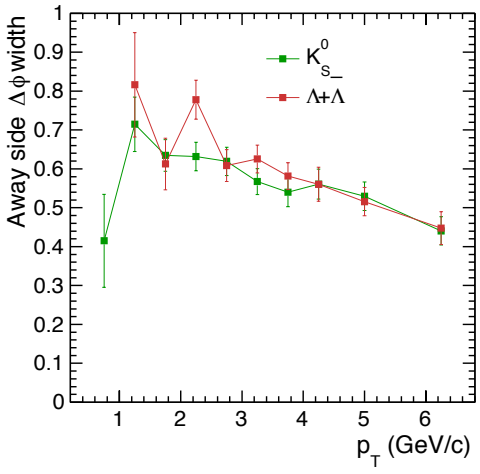

Figure 7.10: away-side $\Delta\phi$ gaussian width evolution in different p_T intervals of K^0_S and Λ+$\bar{\Lambda}$.

Another important parameter is the Gaussian amplitude evolution in different p_T intervals of K^0_S and Λ+$\bar{\Lambda}$. This will gives us a hint about K^0_S and Λ+$\bar{\Lambda}$ yield produced in the near-side and away-side jets in a fragmentation process. Figure 7.11 shows this Gaussian amplitude evolution for near and away-side for both particles. At $p_T < 3$ GeV/c we can see that in near and away-side K^0_S production dominates over the Λ+$\bar{\Lambda}$, but for $p_T > 3$ GeV/c both amplitudes tend to be equal. The origin of the Gaussian, used to explain the tail-like behavior, is unknown and further investigations will be important to understated the nature of particle

distributions close to near-side jet peak.

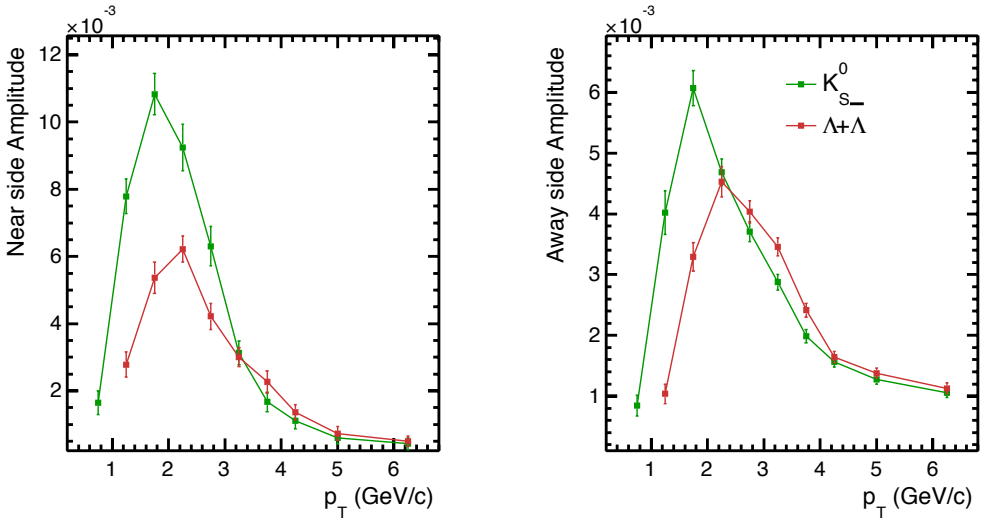

Figure 7.11: near-side gaussian amplitude (right) and away-side gaussian amplitude (left) evolution in associated p_T intervals of K^0_S and Λ+$\bar{\Lambda}$.

Figure 7.12 shows the variation of ΔR ($\sqrt{\Delta\eta^2 + \Delta\phi^2}$) in associated momentum bins. In this plot data points were fitted with a zero degree polynomial, which is the green dashed line for K^0_S and red dashed line for Λ+$\bar{\Lambda}$. The parameter values obtained for ΔR for both particles from the fit are 0.437532±0.010293 (stat) and 0.477685±0.0141614 (stat) for K^0_S and Λ+$\bar{\Lambda}$ respectively. We can conclude from this that the Λ+$\bar{\Lambda}$ production radius tends to be slightly higher than the K^0_S radius, but both are in good agreement with the nominal jet cone radius used for full jet reconstruction in other analysis in ALICE.

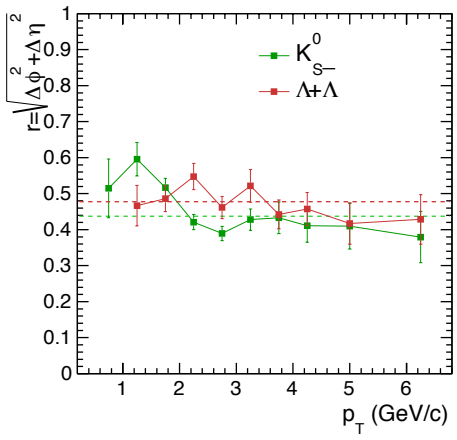

Figure 7.12: Estimation of the near-side jet cone radius for K^0_S and $\Lambda+\bar{\Lambda}$.

7.4 Tsallis-based model fit function to investigate the correlation observables

In our second approach to interpret the data we used a three component fit function, with only one component for the near-side jet peak. This fit function includes a Tsallis (Q-Gaussian) distribution [172, 173] to describe the near-side jet peak and a Tsallis to explain the away-side jet peak as well as a zeroth order polynomial to describe the pedestal. The functional form and number of parameters used were explained in detail in Chapter 5.4.1.2. The two most important parameters of a Q-Gaussian distribution are β and q. The β parameter controls the width of the distribution, small β values signal larger widths and larger β values signal small widths. The q parameter controls the tail-like behavior away from

the peak position. Lower values of q will signal a large non-Gaussian tail in the distribution while higher values of q will favor a tail-like behavior near the peak position. When q→1, the Q-Gaussian distribution becomes a Gaussian distribution. This is illustrated graphically for three different q values (1,1.5, 2), where each q value has four different β values (0.1,1,10 and 100) in Figure 7.13. Black curves represent the Gaussian distributions and corresponding β values, which gives a hint of how close we are to the peak position.

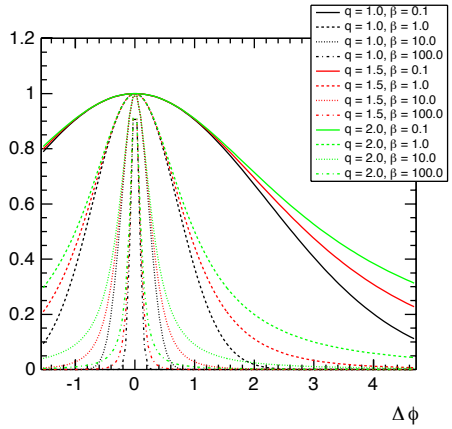

Figure 7.13: Q-Gaussian distributions for four different β values in q=1, 1.5, 2.

From the previous fit results we infer a very narrow behavior of the near-side jet peak, thus selecting larger beta values and q values greater than one can be used to explain the data distribution of near-side. Ultimately q=1.5 and β=10 minimize the χ^2 for the near-side fit. Figure 7.14 and 7.15 shows the final fit results in ten different associated momentum bins using the Q-Gaussian distribution for K^0_S and Λ+$\bar{\Lambda}$.

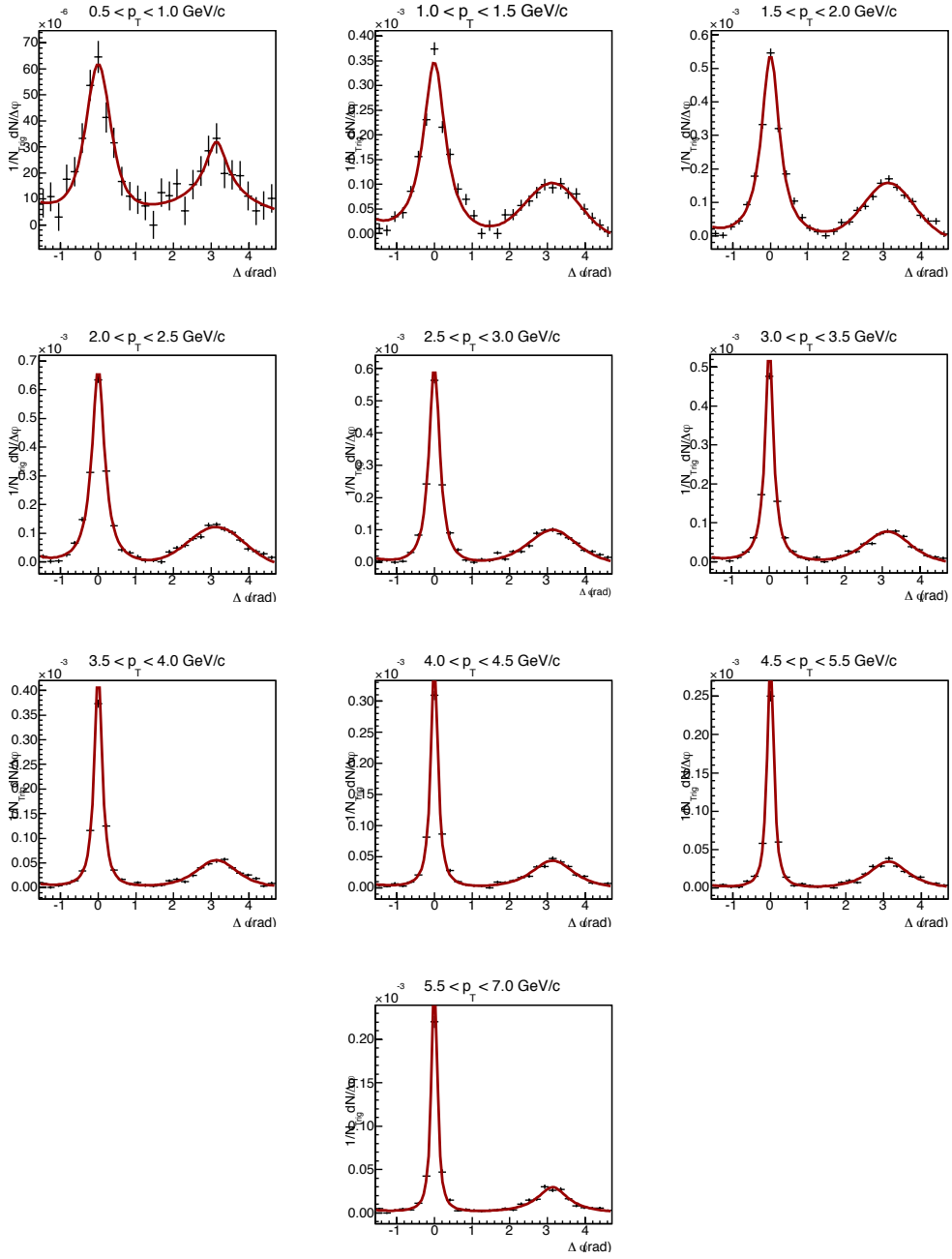

Figure 7.14: One dimensional $\Delta\phi$ projections for K^0_S in ten different bins fitted with two Tsallis functions for the near and away side with a pedestal distribution for the uncorrelated background.

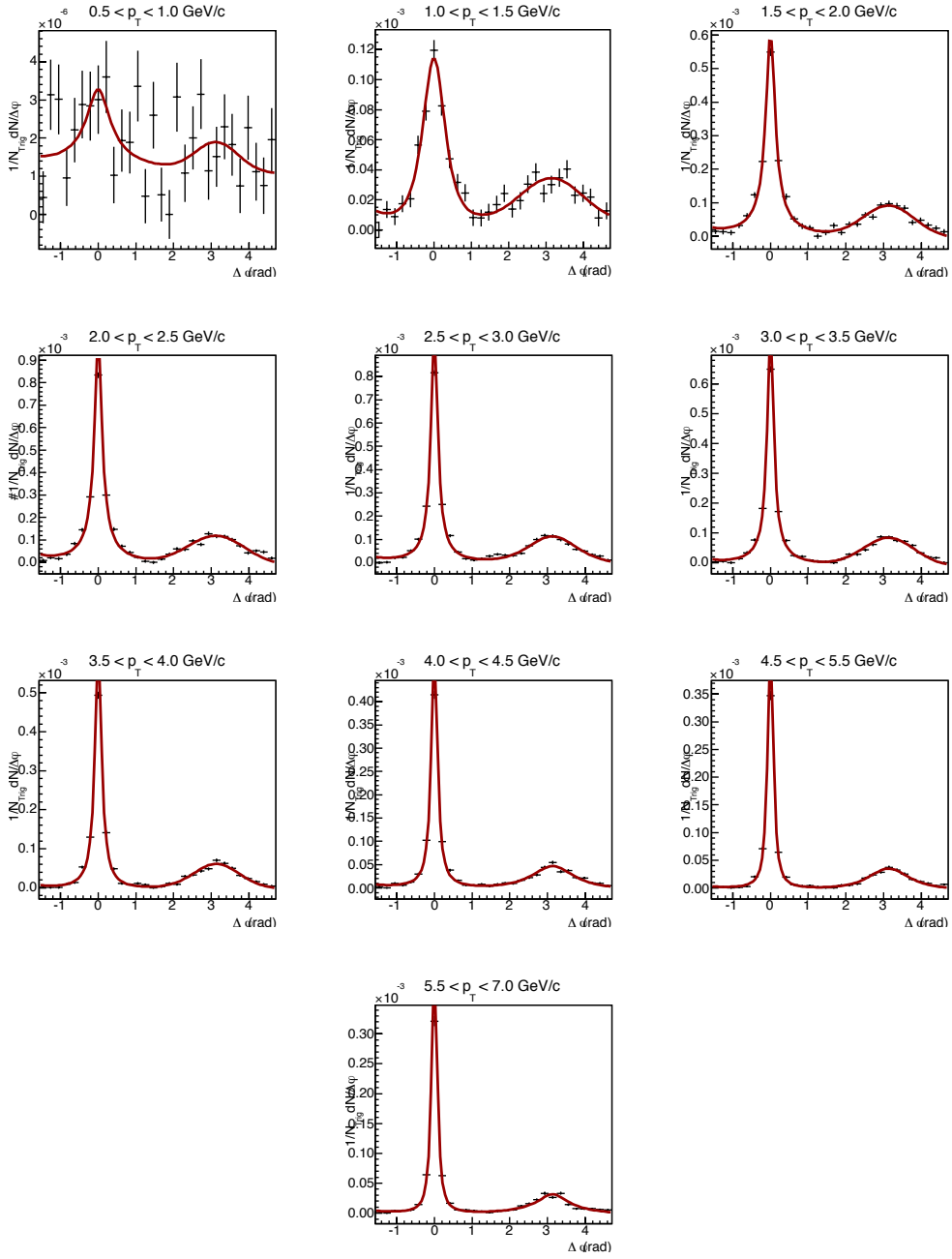

Figure 7.15: One dimensional $\Delta\phi$ projections for Λ+$\bar{\Lambda}$ in ten different bins fitted with two Tsallis functions for the near and away side with a pedestal distribution for the uncorrelated background.

As one can see for both particle species the near-side jet peak is well explained with a single fit component. Figure 7.16 shows the near- and away-side β values for K^0_S and Λ+$\bar{\Lambda}$. β values on the near-side are much larger than the away-side, which suggest the hadronisation of V^0 is more like to occur near the leading particle. Moreover K^0_S and Λ+$\bar{\Lambda}$ production are well separated in near-side region for $p_T < 3$ GeV/c while on the away-side for all p_T intervals the width distribution of baryons and mesons are comparable.

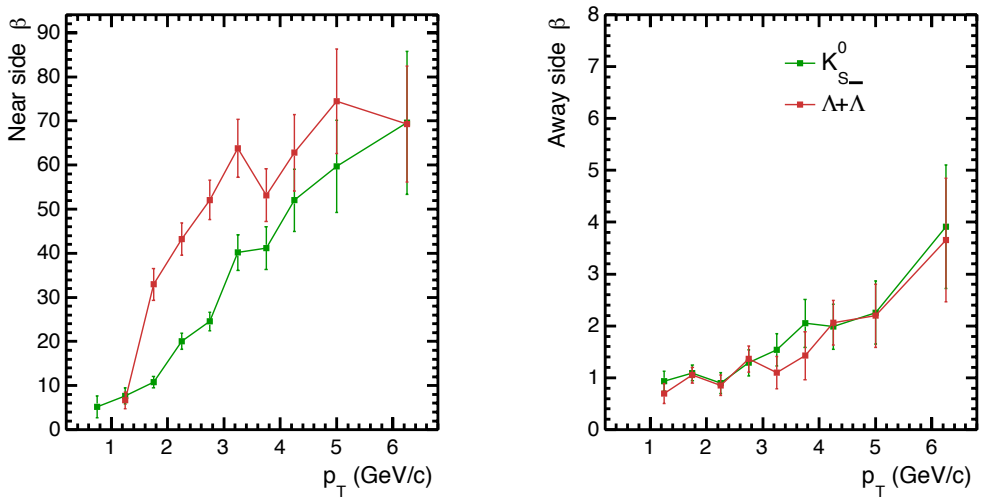

Figure 7.16: near-side (right) and away-side (left) β values for K^0_S and Λ+$\bar{\Lambda}$.

Figure 7.17 shows the near- and away-side q values for K^0_S and Λ+$\bar{\Lambda}$. On the near-side we can see a significant deviation from q=1 that suggests that the distribution is not a Gaussian. For the away-side we fit the q values for K^0_S (green) and Λ+$\bar{\Lambda}$ (red) with a zero degree polynomial and found the parameter is equal to one. This suggests a more Gaussian like distribution on the away-side.

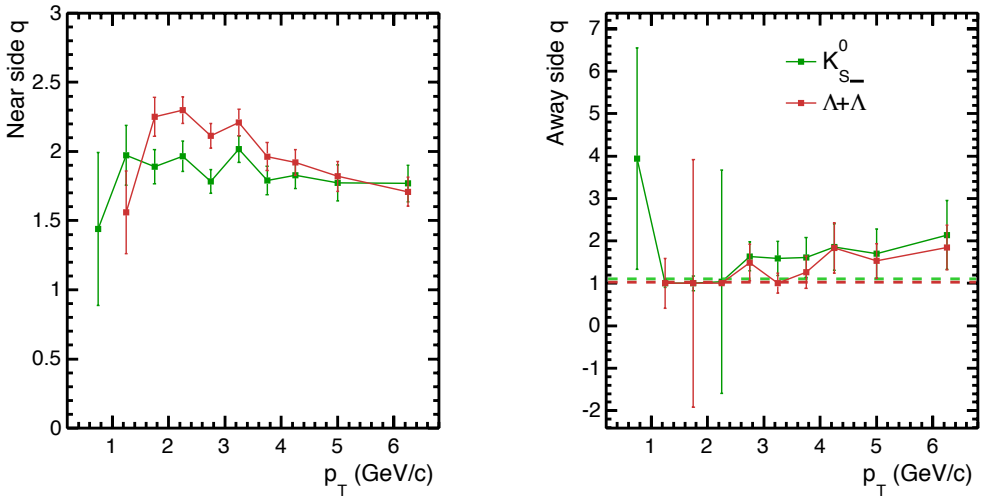

Figure 7.17: near-side (right) and away-side (left) q values for K^0_S and Λ+$\bar{\Lambda}$.

7.5 Fit quality determination

The overall quality of the fit can be determined from the residual of the data points and the fit for each associated p_T interval. The residual distribution considered in this analysis is given in Eq 7.1,

$$R(\Delta\phi) = \frac{D(\Delta\phi, p_T) - F(\Delta\phi, p_T)}{\sigma_{(\Delta\phi, p_T)}} \tag{7.1}$$

where $D(\Delta\phi) = 1/N_{Trig} dN/dp_T$ and $\sigma_{(\Delta\phi, p_T)}$ is the statistical error associated in each $\Delta\phi$ bin. If we observe any positive value for $R(\Delta\phi)$ it suggests that the fit underestimates our data points where any negative value for $R(\Delta\phi)$ suggests an overestimation of the data points by the fit.

7.5.1 Fit quality of the four-component fit

Figure 7.18 shows the $R(\Delta\phi)$ distribution for the Gaussian fit function for K^0_S (left) and $\Lambda+\bar{\Lambda}$ (right) in all associated p_T intervals. The x-axis shows the $(\Delta\phi)$ and y-axis shows the associated p_T, the value of $R(\Delta\phi)$ is given by the colors in the palette. A clear deviation from $R(\Delta\phi)$=0 can be observed besides the near-side jet peak. This overestimation signifies the difficulty of using a single Gaussian to explain the tail-like distribution of the near-side jet peak.

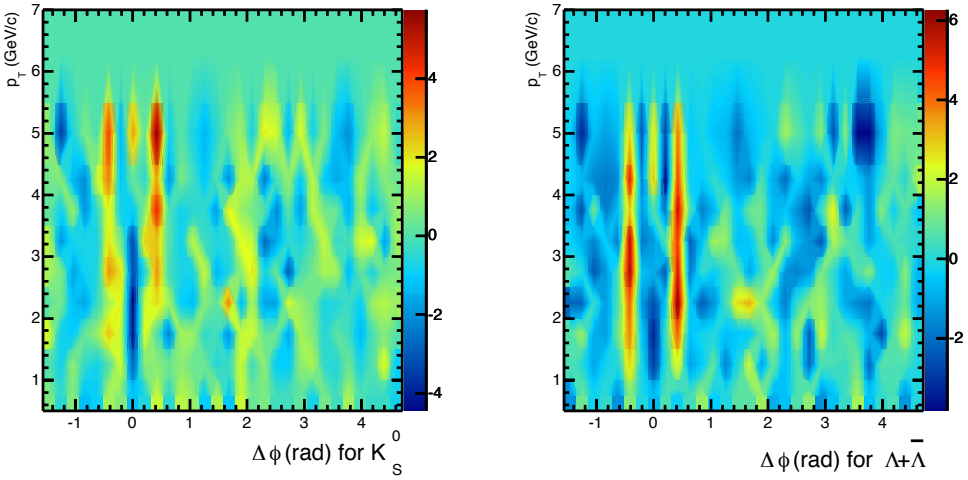

Figure 7.18: $R(\Delta\phi)$ distribution for the Gaussian fit function for K^0_S (left) and $\Lambda+\bar{\Lambda}$(right) in all associated p_T intervals.

Inclusion of the second Gaussian demands a good description of the peak distribution near $\Delta\phi \approx 0$.

7.5.2 Fit quality of the three-component fit

Figure 7.19 shows the $R(\Delta\phi)$ distribution for the Tsallis fit for K^0_S (left) and $\Lambda+\bar{\Lambda}$ (right) in all associated p_T intervals. From this $R(\Delta\phi)$ distributions we can conclude that Tsallis fit functions describes the tail regions around the near-side peak, but a strong overestimation of the data is seen for $\Delta\phi \approx 0$ for both K^0_S and $\Lambda+\bar{\Lambda}$ that is also obvious from Figures 7.14 and 7.15.

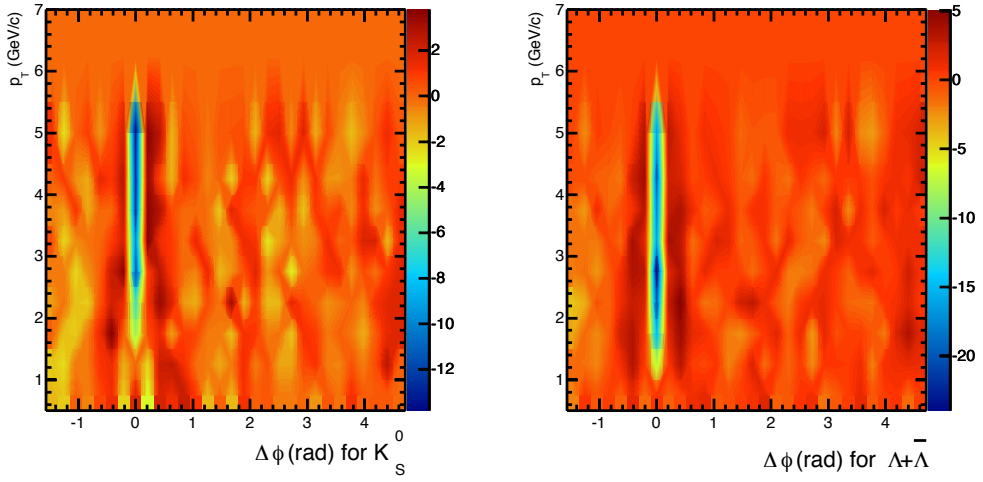

Figure 7.19: $R(\Delta\phi)$ distribution for the Tsallis fit functions for K^0_S (left) and $\Lambda+\bar{\Lambda}$ (right) in all associated p_T intervals.

Comparing the two fit functions, $R(\Delta\phi)$ for three component fit function ranges from -20 to +5 while the four component fit function range from -4 to +6. Thus, the three component fit function varies about three times more than the four component fit function, which suggest that the introduction of the extra component increases the overall quality of the fit.

7.6 V^0 transverse momentum spectra and comparisons with simulation predictions

Once we have measured the transverse momentum distributions in three different regions (near, away-side and underling event) as described in Chapter 5.6, for K^0_S and Λ+$\bar{\Lambda}$, it is important to determine whether the available Monte Carlo models are able to describe the associated yields. Most of the pp interactions at high energy collisions are biased towards the soft regime ($p_T < 2$ GeV/c), which has large cross-sections, about 50 mb at 7 TeV. The physics of the soft interactions is not well understood by pQCD calculations, which can successfully explain the hard processes such as jets and $W^{\pm}$ production. For this purpose, we use the PYTHIA MC event generator version 6.4 [174]. We chose the PYTHIA event generator because it is the most frequently updated package and therefore well suited to analyze the data collected at the LHC energies. This MC event generator has a significant number of free parameters, which directly link to certain physics approximations. The PYTHIA event simulator incorporates various aspects of the theory of QCD , and is based on Leading Order (LO) QCD interactions [175]. PYTHIA also uses higher order calculations in order to explain the parton radiation mechanism in the initial and final states of the collision. Several important stages of a PYTHIA event are outlined bellow.

- The distribution of the partons inside the initial hadrons are modeled by the Parton Distribution Functions (PDF) described in Chapter 1.6.2. Initially two partons from incoming hadrons are allowed to undergo a hard

scattering. During these hard scatterings short lived force carriers such as $W^{\pm}$ and Z^0 are produced and decay in to their daughters.

- The initial accelerated partons have both color and charge and therefor generate bremsstrahlung radiation. These initial emissions are known as Initial State Radiation (ISR). In PYTHIA, ISR are modeled by space-like parotn showers. Similarly, outgoing partons emit Final State Radiation (FSR) that is modeled by time-like parton showers.

- Other than the initial hard scattering partons there are other partons inside the hadron and they also can scatter and may produce more partons. This process is called Multiple Parton Interaction (MPI).

- All outgoing partons should be confined inside a hadron. This process is known as hadronization. PYTHIA uses Lund string fragmentation to model hadronization. This model is capable of calculating the transition from a multi-parton system to a bound state state hadron using string fragmentation.

Here we specifically use PYTHIA 6 Perugia-0 tune to test the V^0 production associated with the high p_T leading particle. Figure 7.20 shows the corrected extracted yields in the near, away side and underling event region for the K^0_S mesons. The black curve in all three panels corresponds with the minimum bias K^0_S measurement. The first panel compares the hard near-side spectra with the inclusive spectra, a clear difference between the hard component and soft component is visible and similar trend was observed in Figure 7.1. Similarly the second panel

compares the hard away-side spectra with inclusive spectra where same difference can be observed for hard and soft part. Finally third panel compares the soft underlying event spectra with inclusive spectra, where the gradients show the similar particle production mechanisms for both regions. In all three panels the green curve is the MC prediction for the near-, away-side and underlying event regions. The meson production in the near-side jet is well described by the Monte Carlo model while the meson production on the away-side region and the underling event region is underestimated by PYTHIA Perugia-0, which suggests that further parameter tuning in the MC model is necessary.

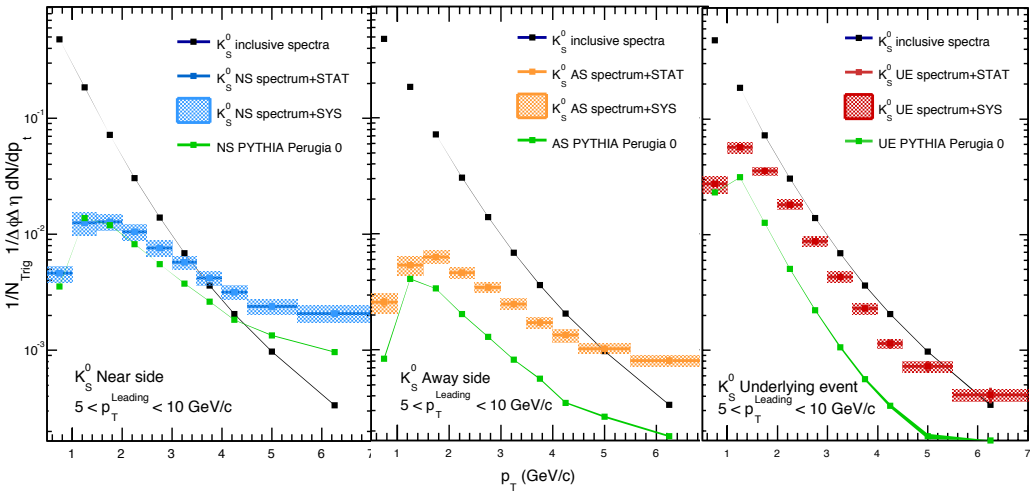

Figure 7.20: Efficiency corrected K^0_S production spectrum in different region compared with PYTHIA Perugia-0 and inclusive production.

Figure 7.21 shows the corrected extracted yields in the near, away side and underling event region for the Λ+$\bar{\Lambda}$ baryons. The black curve in all three panels

corresponds with the minimum bias Λ+$\bar{\Lambda}$ measurement. The first panel compares the hard near-side spectra with the inclusive spectra, where a clear difference between the hard component and soft component is visible. The second panel compares the hard away-side spectra with inclusive spectra, where same difference can be observed between the hard and soft parts. Finally, the third panel compares the soft underlying event spectra with the inclusive spectra, where the gradients show the similar particle production mechanisms for both regions. An important observation is that the baryon production in the underlying event is closer to the minimum bias events than for the meson. This may hint to the fact that the baryon to meson anomaly in Pb+Pb collisions is due to the increase of non-pQCD phenomena, such as hydrodynamic flow. In all three panels the green curve is the MC prediction for the near, away side and underlying event regions. The other important conclusion is that the baryon production in all regions is clearly underestimated by PYTHAI Perugia 0, which suggest that the MC generators have problems with hadronizing the three quark state compared with the quark-antiquark state.

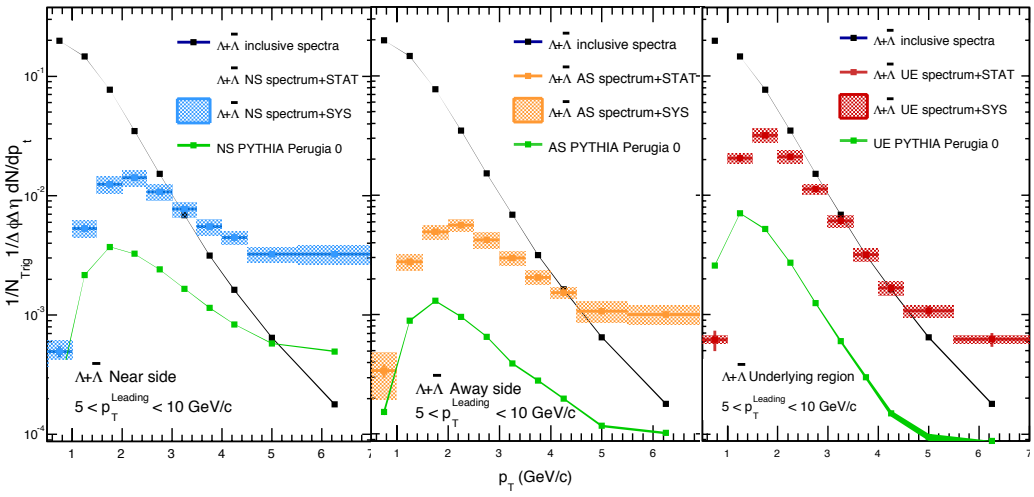

Figure 7.21: Efficiency corrected Λ+$\bar{\Lambda}$ production spectrum in different region compared with PYTHIA Perugia-0 and inclusive production.

7.7 Multiplicity dependence of $h^{\pm}$-V^0 correlations

In this section we try to link the results discussed in previous sections to the question of QGP formation. As explained in Chapter 1, QGP formation occurs only in high energy density heavy-ion collisions. The main purpose of the pp collisions is to use their results as a baseline for the comparison with heavy-ion results. The high luminosity of the LHC at 7 TeV provides physicist with tools to explore a whole new aspect of pp collisions, namely high multiplicity events. These rare events can be selected through different trigger acquisition techniques. In 2010

the CMS collaboration published a result showing a prominent ridge-like structure in high multiplicity pp collisions [176], which is not visible in minimum bias pp collisions. Figure 7.22 shows the two CMS particle correlation functions for 7 TeV pp minimum bias events (left) and high multiplicity (Ntrk>110) events (right). In minimum bias events the long range $\Delta\eta$ structure is not visible while in events with more than 110 charged particles a prominent ridge like structure is visible.

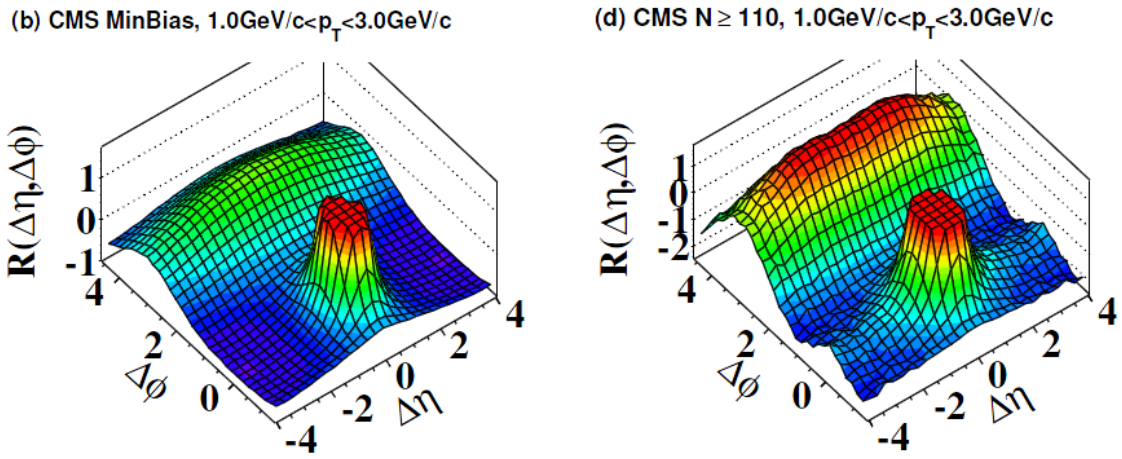

Figure 7.22: Two particle correlation functions for 7 TeV pp minimum bias events (left) and high multiplicity (Ntrk>110) events (right).

ALICE also tried to measure the same two particle correlation in high multiplicity events, but the limited acceptance in TPC (-1< η <1) is not sufficient compared with CMS (-4< $\Delta\eta$ <-2 and 2< $\Delta\eta$ <4) to explore the ridge. In this thesis we try to investigate the $h^{\pm}$-V^0 correlations in six different multiplicity classes. Figure 7.23 shows the total multiplicity distribution after the ALICE minimum

bias trigger and a 10 cm primary vertex cut have been applied to each event. The colors indicate the selected multiplicity bins starting from 50 charged tracks per event. When performing measurements in high-multiplicity proton-proton collisions, pileup may become an issue, as it is highly probable that a high-multiplicity event is due to the piling up of two interactions. To minimize this effect each event is individually tested for any pileup effects as described in Chapter 3.3.2. A track is selected if the $|\eta| < 0.9$ and minimum p_T is 0.15 MeV/c. Table 7.1 summarizes the final event count in each multiplicity class after all event and track selection cuts.

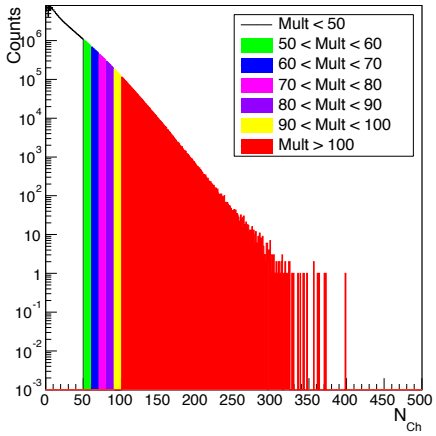

Figure 7.23: Multiplicity intervals after minimum bias trigger and 10cm primary vertex cut.

Multiplicity Class	Number of events
50 < Mult < 60	7854547
60 < Mult <70	5210120
70 < Mult < 80	3391514
80 < Mult < 90	2172087
90 < Mult < 100	1367876
100 < Mult	2323205

Table 7.1: Number of events analyzed in each multiplicity class after event and track selection cuts.

Once we confirmed the selected multiplicity classes we repeat the $h^{\pm}$-V^0 correlation analysis in each multiplicity bin and extract the correlation structures and associated yields in the three regions for K^0_S and Λ+$\bar{\Lambda}$. Figure 7.24 shows the one dimensional $\Delta\phi$ correlation function for K^0_S in ten different momentum bins for each multiplicity class. A clear difference in correlation structures is observed for different multiplicities, which suggests that the underlying physics we are probing is different in low multiplicity events versus high multiplicity events. The same difference is observed in Figure 7.25 for Λ+$\bar{\Lambda}$ in six multiplicity classes. The key observation is that the higher the event multiplicity the larger the amplitude of the near-side peak. Due to the limited number of statistics we were not able to successfully fit the correlation function and no efficiency correction was applied.

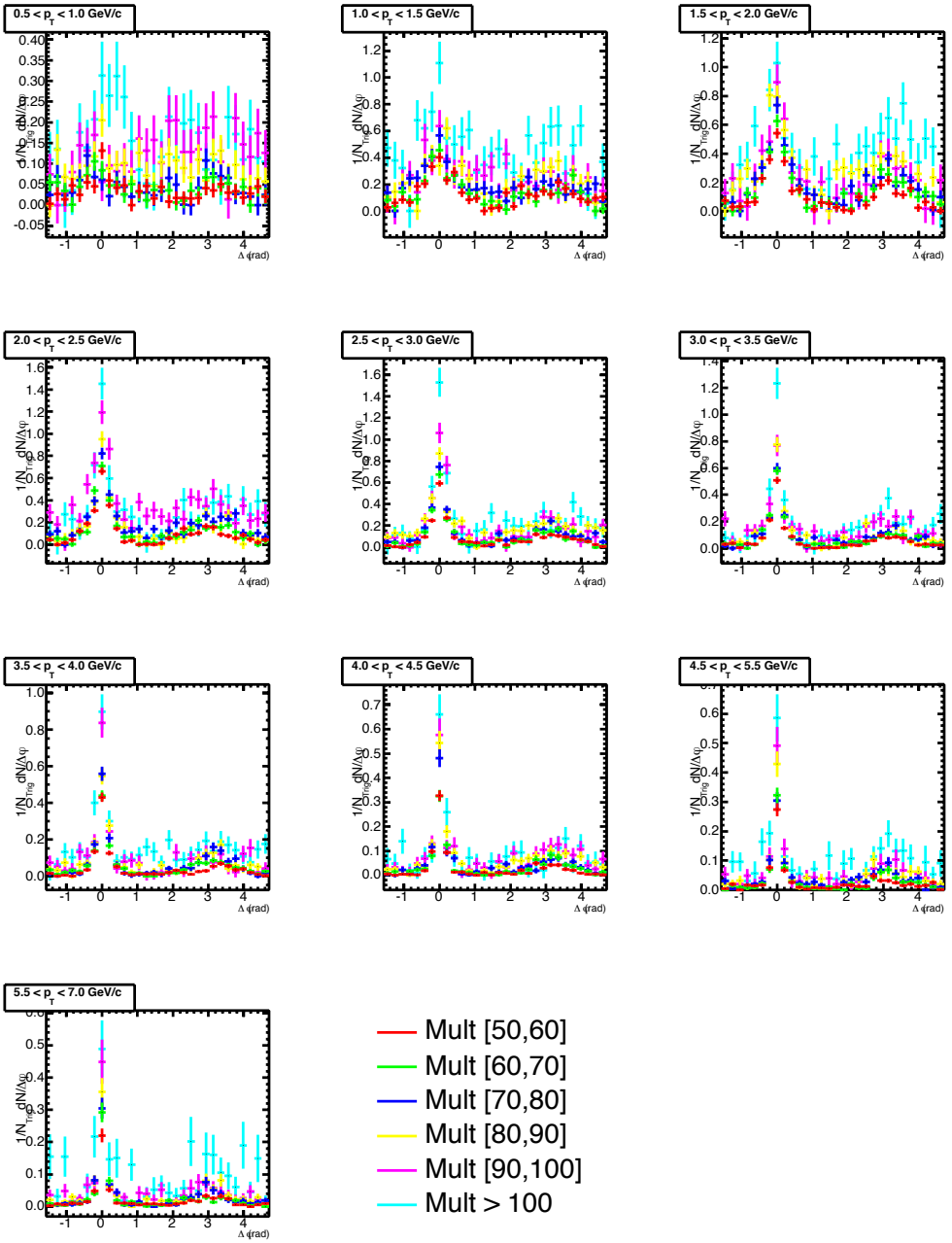

Figure 7.24: One dimensional $\Delta\phi$ projections for K^0_S in ten different momentum bins for each multiplicity class.

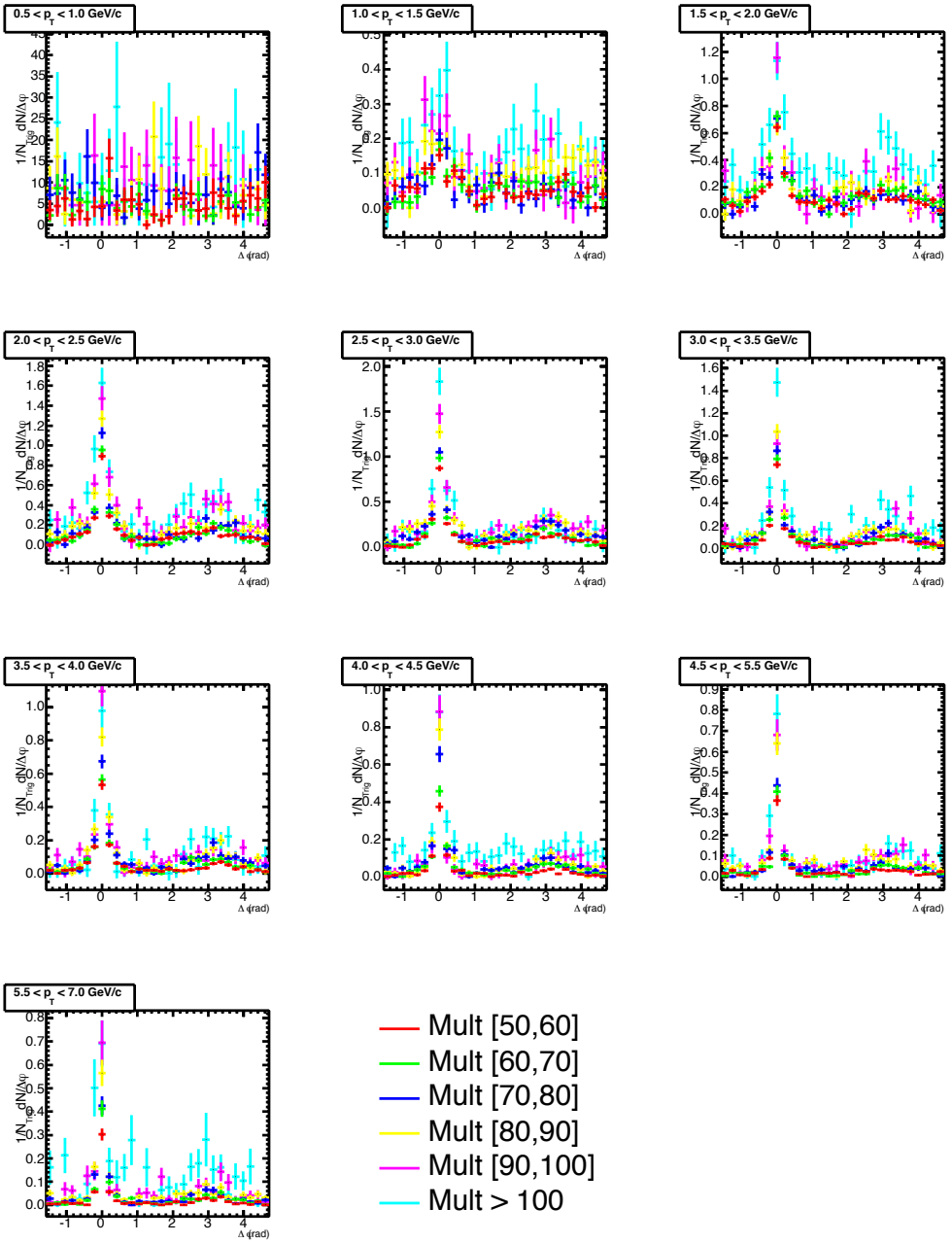

Figure 7.25: One dimensional $\Delta\phi$ projections for Λ+$\bar{\Lambda}$ in ten different momentum bins for each multiplicity class.

Figure 7.26 shows the uncorrected yields in the three different regions for the associated K^0_S particles. If one assumes a first order efficiency correction, where for each multiplicity class the reconstruction efficiency is almost equal, this result suggests that more mesons are produced in high density events. The smooth line shows the limits of the highest and lowest multiplicities. In the jet cone the difference is larger than in the underling event, suggesting that meson production in high multiplicity events is predominantly from the hard fragmentation process.

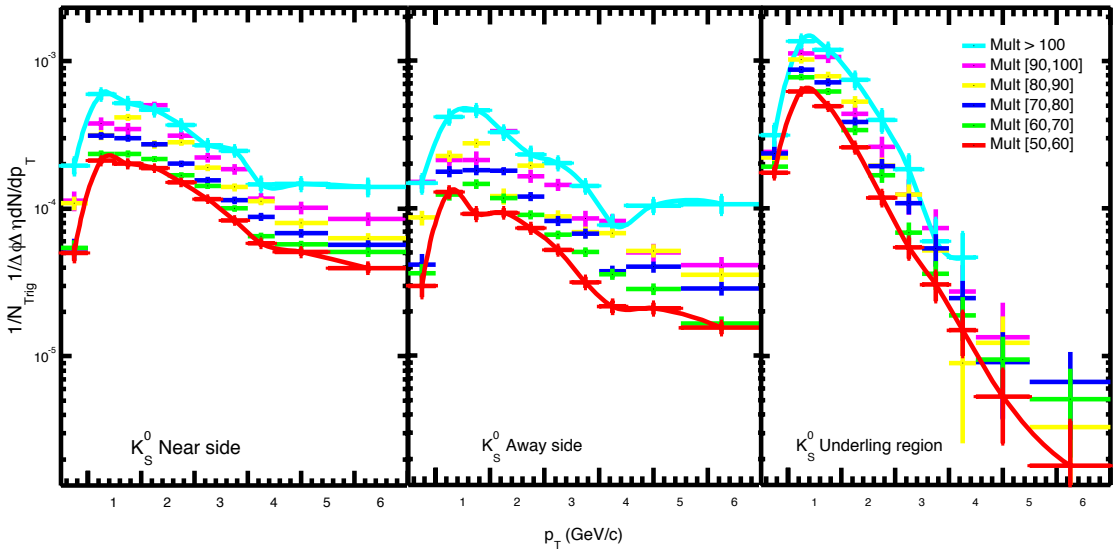

Figure 7.26: Uncorrected p_T spectrum of K^0_S in selected multiplicity events for near, away side and underlying region.

This observation is also in agreement with the results obtained in the centrality evolution studies of V^0 production in Pb+Pb collisions. In more central collisions the multiplicity is higher. Figure 7.27 shows the uncorrected yields extracted

in the three different regions for associated Λ+$\bar{\Lambda}$ particles. A clear difference in extracted yields is visible for different multiplicity classes. The same conclusions as for meson can also be drawn for the baryon production. In other words the relative enhancement of baryons and mesons in high multiplicity pp events comes from an enhanced hard fragmentation, even at moderate p_T ($p_T > 1$ GeV/c). This is surprising since MPI supposed to play a large role in this momentum range.

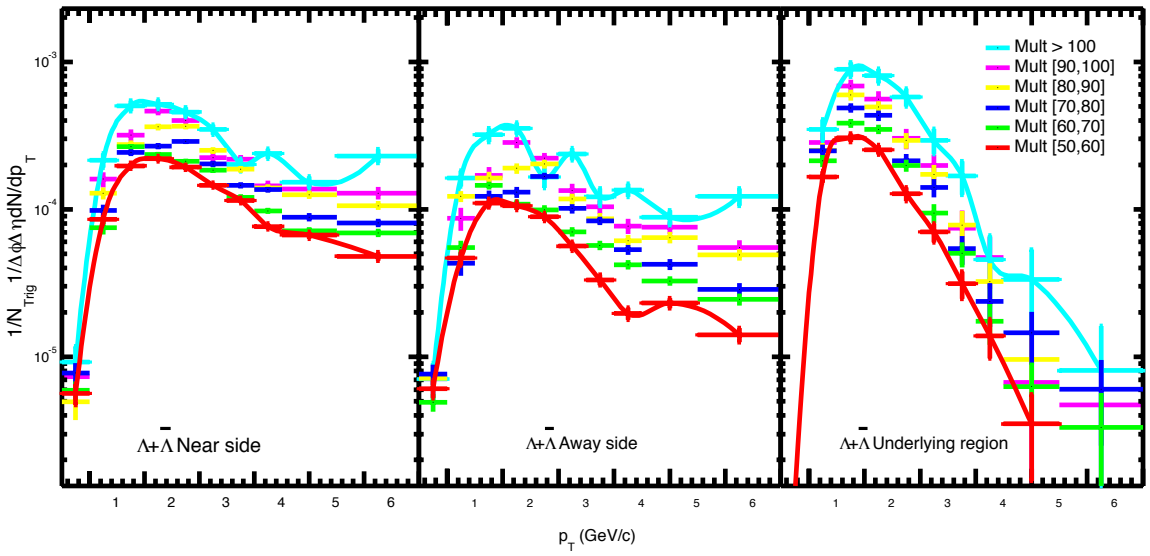

Figure 7.27: Uncorrected p_T spectrum of Λ+$\bar{\Lambda}$ in selected multiplicity events for near, away side and underlying region.

To investigate any baryon to meson anomaly we extracted the Λ+$\bar{\Lambda}/2K^0_S$ ratio in different associated momentum intervals as a function of multiplicity in three different regions. The observed results are shown in Figure 7.28 for the near-side, away-side and underlying event region. For both jet regions we see a nearly

unchanged baryon to meson ration in all transverse momentum intervals. The underlying region shows a baryon to meson ratio enhancement in high multiplicity events in the intermediate transverse momentum region. This suggest that the baryon production mechanism is more favorable in the underlying event than the quark fragmentation process in jets.

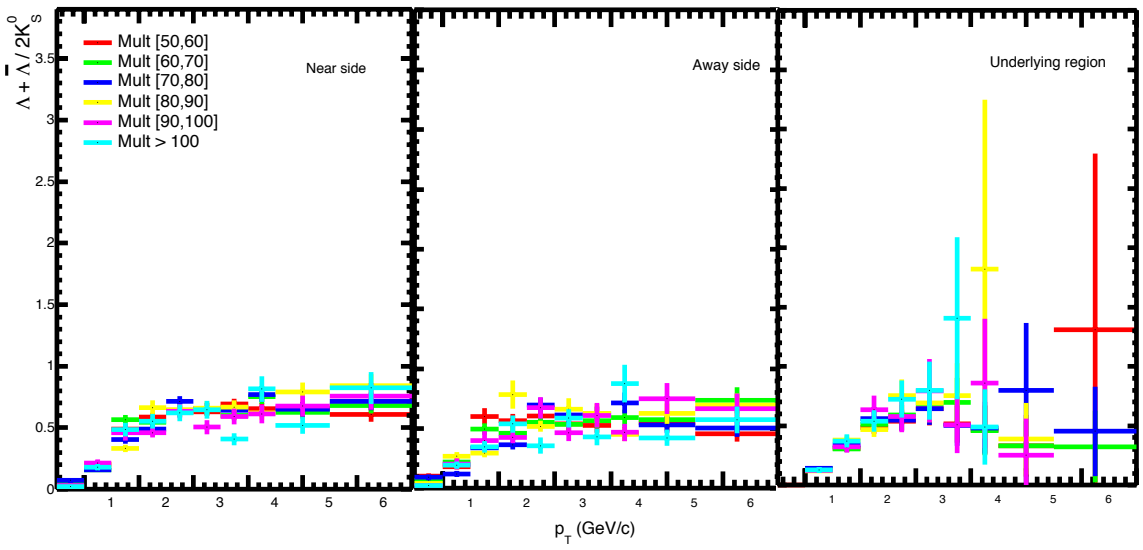

Figure 7.28: Uncorrected Λ+$\bar{\Lambda}/2K^0_S$ ratio in selected multiplicity events for near, away side and underlying region.

7.8 Conclusion

The analysis was performed in 198 million minimum bias pp collisions at LHC energies af 7 TeV. We were able to successfully reconstruct Λ, $\bar{\Lambda}$ and K^0_S particles in real and Monte Carlo data. For ten different associated momentum intervals

two dimensional $\Delta\eta, \Delta\phi$ correlations were extracted for a fixed p_T interval of the leading particle. The azimuthal projection of two dimensional $\Delta\eta, \Delta\phi$ correlations shows clear near-side and away-side jet peaks for identified particle correlations. Two independent model fits functions were introduced to extract possible correlation observables and we show that the near-side particle distribution is not a Gaussian. The calculated jet cone radius for baryons and mesons is nearly equal and found to be 0.4 cm. Particle yield were extracted in near, away and underling event regions and compared with Monte Carlo model PYTHIA Perugia-0. Except for the near-side K^0_S yield PYTHIA strongly underestimates different hadronization mechanisms for baryons and mesons. We show the analysis in different charged particle multiplicity intervals and observe a difference in particle yield as a function of multiplicity in all three regions (near-side, away-side and underlying event). The $\Lambda+\bar{\Lambda}/2K^0_S$ ratio in near- and away-side is was increased at intermediate p_T and saturates in higher momentum regions for all multiplicity classes, while the ratio tends to increase in the intermediate momentum region and decrease at high momentum in the underlying event region, suggesting a more favorable baryon production mechanism at high momentum from hard scattering in all multiplicity classes.

Appendix A

ALICE coordinate system

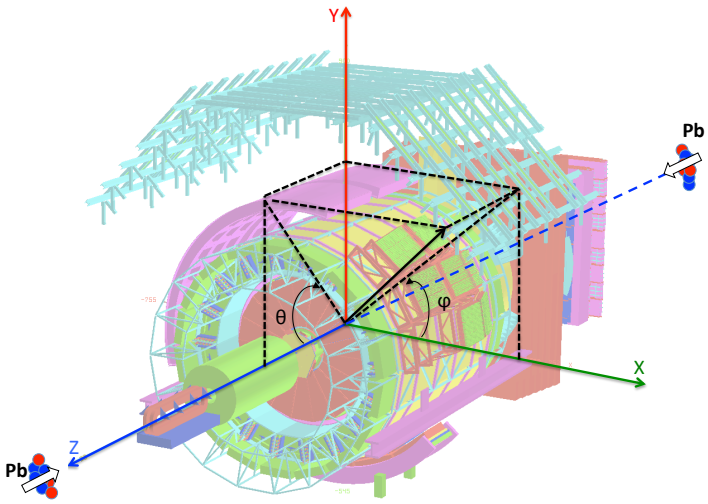

Figure A.1: ALICE coordinate system

The ALICE coordinate system is shown in Figure A.1. It is defined according

to;

1. **Z-axis** is along the beam direction, where the positive Z-axis is along the counter clock vise beam (solid blue Z-axis) and the negative Z-axis is along the clockwise beam (dashed blue Z-axis).

2. **X-axis** is perpendicular to the beam direction and towards the center of the LHC ring.

3. **Y-axis** is perpendicular to the X-axis and pointing upwards.

4. **Azimuthal angle** ϕ increases counter clock vise where ϕ=0 is on the X-axis and ϕ=$\pi/2$ is on the Y-axis with the observer on the positive Z-axis looking towards the clockwise beam.

5. **Polar angle** θ increases from positive Z-axis towards to the negative Z-direction with θ=0 in positive Z-axis and θ=π is in negative Z-direction.

6. x=y=z=0 is at the nominal interaction point.

Appendix B

Kinematic variables

In modern particle accelerators colliding beams travel with nearly the speed of light. Therefore, to explain the dynamics of initial and final particles it is convenient to use relativistic kinematics. In the special theory of relativity a particle's position and momentum is described in terms of four-vectors $\mathbf{X}^{\mu}$ and $\mathbf{P}^{\mu}$, where μ=0,1,2,3.

$$\mathbf{X}^{\mu} = (ct, x, y, z) \tag{B.1}$$

$$\mathbf{P}^{\mu} = (E/c, p_x, p_y, p_z) \tag{B.2}$$

According to the ALICE coordinate system we define transverse momentum (p_T) which is perpendicular to the beam direction, and longitudinal momentum (p_L) along the beam pipe as;

$$p_T^2 = p_x^2 + p_y^2 \tag{B.3}$$

$$p_L = p_z \tag{B.4}$$

It is important to define these two momentum components because, the momentum along the beam-axis may be associated with the initial beam particles, while the transverse momentum is often associated with particles originated at the collision vertex. Moreover p_T is invariant under Lorentz transformation along the beam direction. The distribution of produced particles is usually expressed as a function of rapidity (y) which is defined as;

$$y = \frac{1}{2} ln(\frac{E + p_l}{E - p_l}) \tag{B.5}$$

Even though rapidity is not invariant, it is additive along the beam-line under Lorentz transformation. It is important to know the mid rapidity where we expect the largest density of produced particles. In a typical fixed target experiment such as SPS with a beam energy of 158 GeV and no moving target we can calculate y_{Target}=0 and $y_{Mid} = y_{Target} + (y_{Projectile} - y_{Target})/2 = y_{Projectile}/2 = 2.91$. This is shown in Figure B.2.

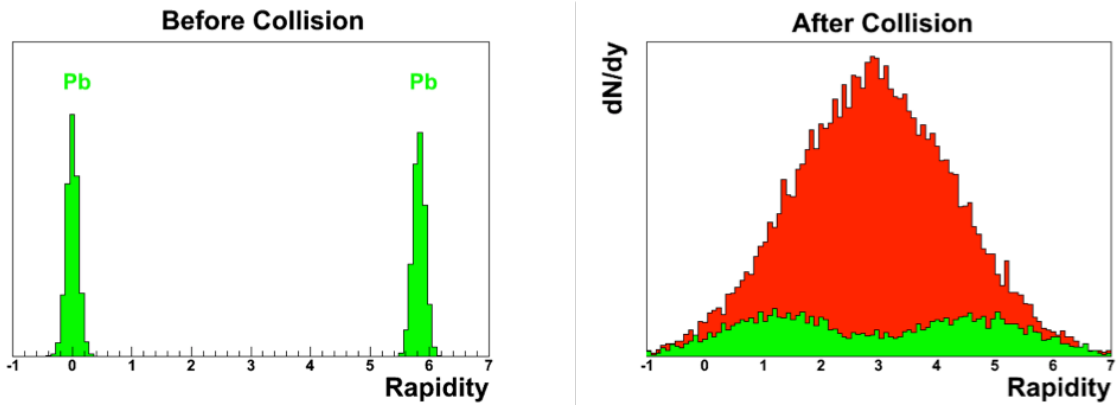

Figure B.1: SPS rapidity distributions

The situation is different in a collider experiment of counter rotating beams of equal energies. For RHIC energies of 100 GeV per beam $y_{Target} = -y_{Projectile} = 5.36$ and $y_{Mid} = y_{Target} + (y_{Projectile} - y_{Target})/2 = 0$

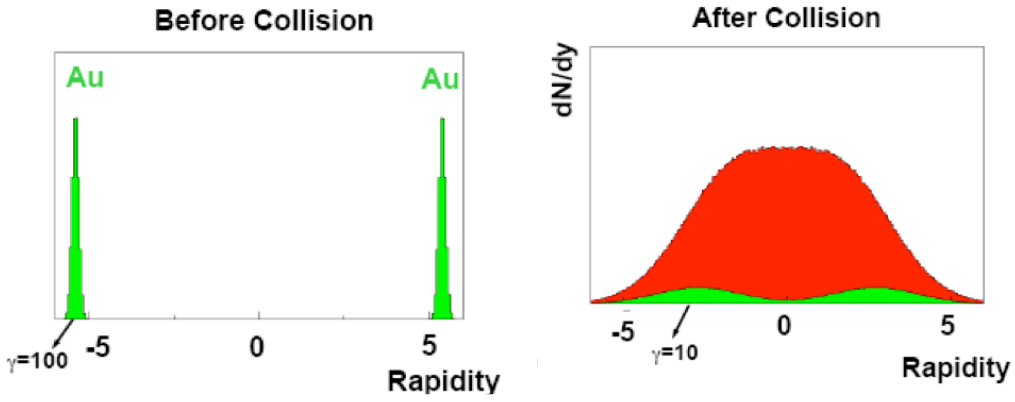

Figure B.2: RHIC rapidity distributions

Since rapidity is a function of energy and momentum it is only strictly defined for identified particles. An alternative is to use pseudo-rapidity (η);

$$\eta = -log(tan(\theta/2)) \tag{B.6}$$

Appendix C

Additional Alice detectors

C.1 Time Of Flight detector (TOF)

The main purpose of the TOF detector is to identify hadrons beyond 1 GeV/c where identification by TPC is not effective. The TOF detector is a large array of Multigap Resistive Plate Chamber (MRPC) with about 153000 readout channel. It is located in the central barrel at a distance of 370 cm from the beam pipe. It has a full azimuthal coverage and in pseudorapidity it coverage is -0.9 < η < 0.9. The inner and outer radius of the TOF is 370 and 399 cm respectively [177]. Figure **??** shows the Schematic view of the TOF wrt ITS and TPC. As one can see TOF consist of 18 sectors in azimuth. Five modules with MRPCs consist of one sector. Particle trajectory detected by ITS and TPC can be combined with a detection and excellent temporal resolution in TOF. The TOF measures the velocity of particles by measuring how long it takes for a particle to reach the TOF. Figure C.1 shows

different particles identified by the TOF.

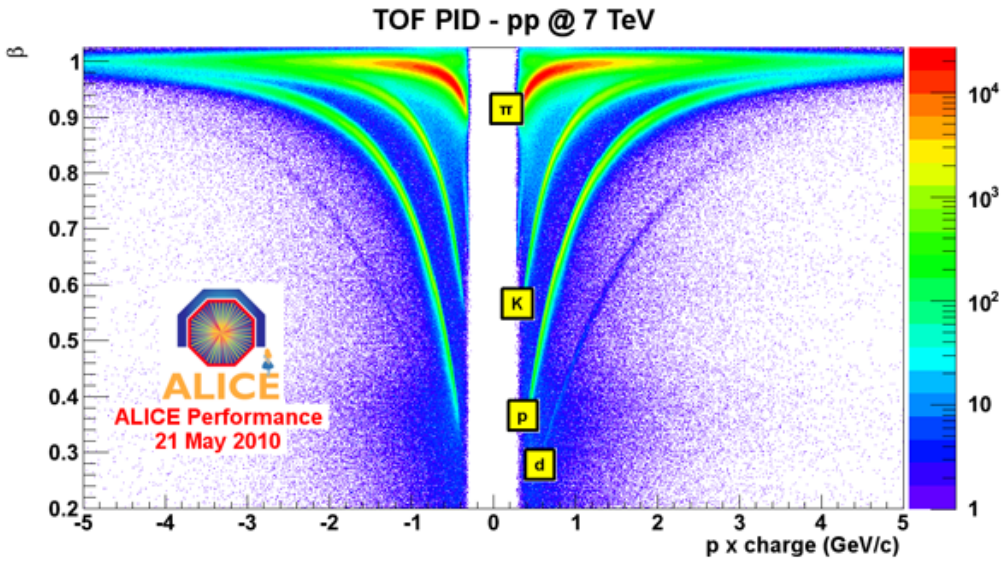

Figure C.1: Velocity β=v/c as measured with the TOF detector as a function of the particle momentum p multiplied with the particle charge number Z[178]

The x-axis is the momentum times charge of the particle, as measured by the TPC, and the Y-axis is the β=v/c. Pions ($\pi^{\pm}$) are the lightest particle (140 MeV/c^2) so at a given momentum, they have the highest velocity. Protons (p) are the heaviest (938 MeV/c^2) so at a given momentum they have the lowest velocity. Complete description of the TOF detector can be found in [179]

C.2 High Momentum Particle Identification Detector (HMPID)

When a particle passes through a material with a higher speed than the light on that medium, it will emit photons, which called the Cherenkov radiation until it achieve the speed of light in that medium. The opening angle of Cherenkov radiation cone is depends on the velocity of the particle. At a given momentum, lighter particles go faster, so lighter particles will emit photons at a larger angle relative to their path. HMPID uses this opening angle as a characteristic measure of the particle species to be identified. The HMPID in ALICE covers -0.6 < η < 0.6 in pseudorapidity and 1.2 < ϕ < 58.8 in azimuth. HMPID consist with seven modules (1.5m X 1.5m each) 4.7m away from the nominal interaction point. It uses C_6F_{14} gaseous radiator. The Cherenkov photons are detected on the pad cathodes of MWPC. Each module is consists with six caesium iodide (CsI) photocathodes (60 cm X 40 cm each) [180]. Figure C.2 shows the mean Cherenkov angle measured by HMPID in pp collisions at 7 TeV as a function of track momentum. The X-axis is the momentum and the Y-axis is the Cherenkov angle. For a given momentum, π^+ is going faster than a kaon or a proton. Thus the pion has the highest radius and proton has the lowest radius for a given momentum.

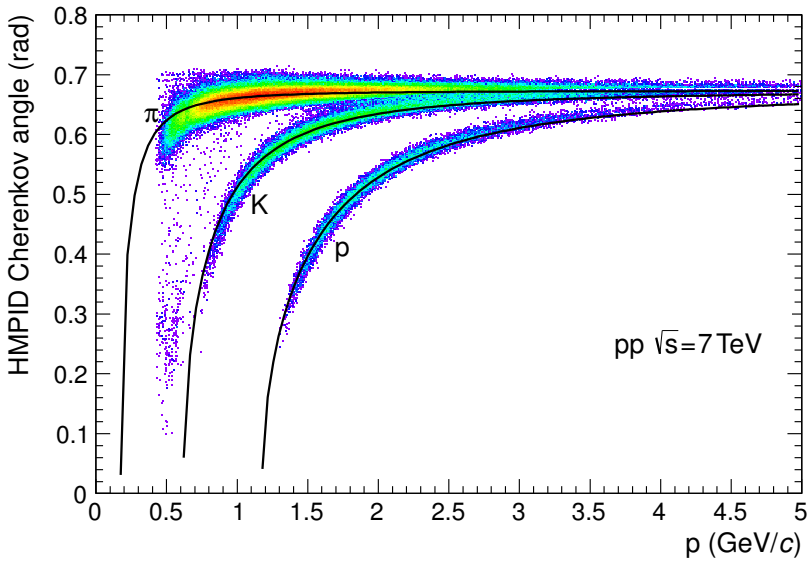

Figure C.2: Mean Cherenkov angle measured by HMPID in pp collisions at 7 TeV as a function of track momentum

C.3 Transition Radiation Detector (TRD)

The main purpose of this detector is to efficiently distinguish electrons and pions, particularly in the case of transverse momentums above1 GeV/c. This distinction is necessary to characterize leptonic decay channels of certain particles, for example, J/ψ decay in to e^+e^- would be more difficult to accomplish in the absence of discriminating between pions and electrons. The TRD detector is one of the detectors with full azimuthal coverage and operates in -0.9 < η < 0.9. The TRD consists of six layers of radiator foil stacks and Time Expansion Chambers filled with Xe/CO_2. More details on TRD can be found on [181, 182]

C.4 Photon Spectrometer (PHOS)

The two main goals of PHOS is to determine thermal properties of the initial phase of the heavy ion collisions and investigate jet quenching effects, by γ-hadron and γ-jet correlations [183]. It is 4.6 m away from the nominal interaction point and consist with five modules. Each PHOS module consists of a charged particle veto (CPV) and a calorimeter segmented with lead-tungstate crystals (PWO). The CPV is a MWPC with a cathode pad readout. The photons from each PWO crystal is read out by one avalanche photon diode. The more technical and functional details on PHOS can be found on [184].

C.5 Forward Muon Spectrometer

Forward Muon Spectrometer is dedicated to detect particles via $\mu^+\mu^-$ decays. Some examples are vector mesons like J/ψ and ψ'. The Forward Muon Spectrometer has the greatest geometrical acceptance for the detection of rare particles ranging from -4 < η < -2.5. The muon spectrometer consists of a composite hadron absorber about one mete away from the interaction point. Tracking of muons are done via five stations of two planes of Cathode Pad Chambers (CPC) with 1.1 M readout channels. The trigger system of muon spectrometer provided a maximum rate of 1 kHz of heavy ions, which is compatible with the data acquisition system in ALICE ALICE [185, 186].

C.6 Zero-Degree Calorimeter (ZDC)

In a heavy ions collision, we can characterize the collision geometric if we measure the energy carried by spectators nucleons, ie those did not participate in the interaction and that continued in the original beam direction. Depending on how much the smaller the impact parameter of a collision, ie in a more central collision, the lower the energy carried by spectator nucleons. The ZDC detector aims to precisely measure these spectator nucleons, but this does not possible by experimental restrictions and only a portion of the spectator nucleons are effectively measured, and the rest is inferred by models. The ZDC detector is made by two sets of calorimeters each set of detectors consists of two hadronic ?spaghetti? calorimeters and two forward EM calorimeters (ZEM) [187].

Appendix D

Distribution of selection cuts for Λ

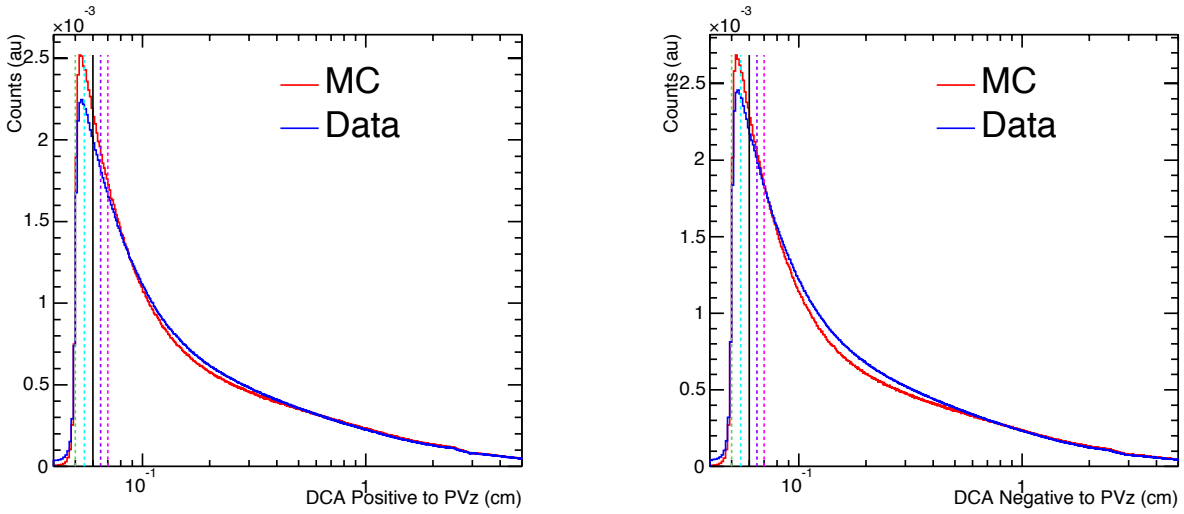

Figure D.1: DCA positive to PVz (left) and DCA negative to PVz (right) for real and MC data for Λ (left).

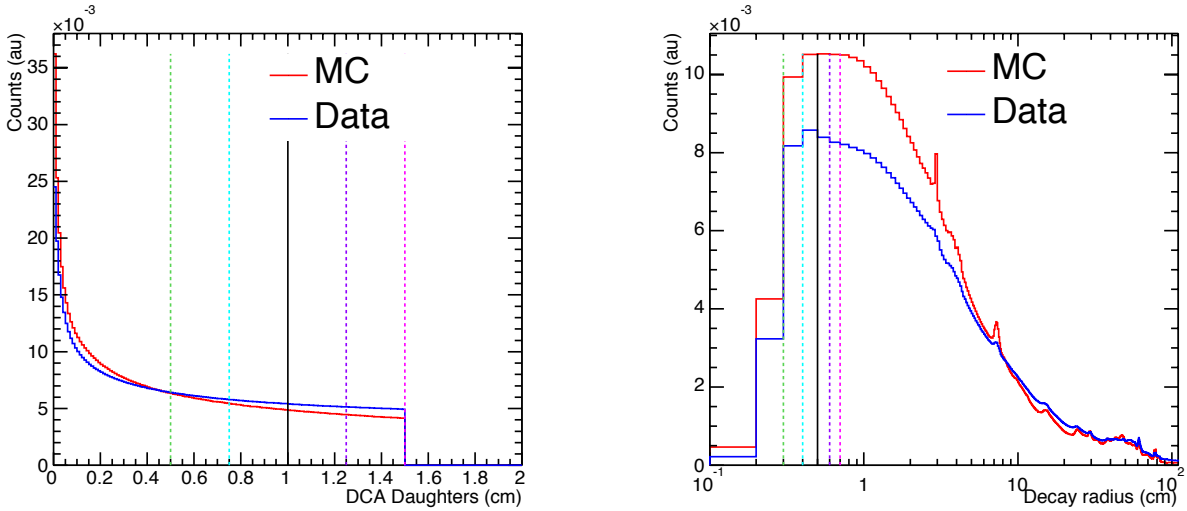

Figure D.2: DCA daughters (left) and decay radius (right) for real and MC data for Λ (left).

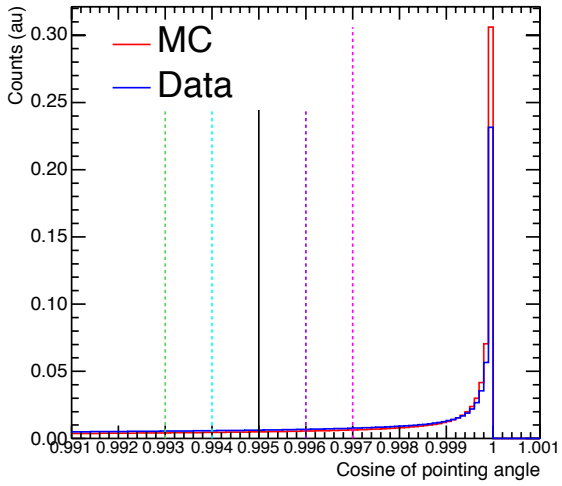

Figure D.3: Cosine of pointing angle for Λ real and MC data.

Bibliography

[1] C. Stringer and P. Andrews. *The Complete World of Human Evolution*. Complete Series. Thames & Hudson, 2005.

[2] P. Jordan. *Neanderthal: Neanderthal Man and the Story of Human Origins*. Sutton, 1999.

[3] F. Halzen and A.D. Martin. *Quarks and leptons: an introductory course in modern particle physics*. Wiley, 1984.

[4] K. White. *Mendeleyev and the Periodic Table*. Primary sources of revolutionary scientific discoveries and theories. Rosen Publishing Group, 2005.

[5] E.A. Davis and I. Falconer. *J.J. Thompson And The Discovery Of The Electron*. Taylor & Francis, 2002.

[6] J.L. Heilbron. *Ernest Rutherford: And the Explosion of Atoms*. Oxford Portraits in Science. Oxford University Press, USA, 2003.

[7] W.N. Cottingham and D.A. Greenwood. *An Introduction to the Standard Model of Particle Physics*. Cambridge University Press, 2007.

[8] M.D. Schwartz. *Quantum Field Theory and the Standard Model*. Quantum Field Theory and the Standard Model. Cambridge University Press, 2013.

[9] P. Langacker. *The Standard Model and Beyond*. Series in High Energy Physics, Cosmology and Gravitation. Taylor & Francis, 2011.

[10] J.F. Donoghue, E. Golowich, and B.R. Holstein. *Dynamics of the Standard Model*. Cambridge Monographs on Particle Physics, Nuclear Physics and Cosmology. Cambridge University Press, 2014.

[11] S.F. Novaes. Standard model: An Introduction. 1999.

[12] K.A. Olive et al. Review of Particle Physics. *Chin.Phys.*, C38:090001, 2014.

[13] A. Seiden. *Particle Physics: A Comprehensive Introduction*. Addison Wesley, 2005.

[14] J.V. Lee. *Search for the Higgs Boson*. Nova Science Publishers, 2006.

[15] M. Born. *Einstein's Theory of Relativity*. Dover Book on relativity and related areas. Dover Publications, 1965.

[16] R.P. Feynman. *Q E D:*. Penguin Books. Penguin, 1990.

[17] J.D. Jackson. *Classical electrodynamics*. Wiley, 1962.

[18] M. Polyak. Feynman diagrams for pedestrians and mathematicians. *ArXiv Mathematics e-prints*, June 2004.

[19] J.W. Rohlf. *Modern Physics: From (Sa (Bto Z0*. New York [etc.] : John Wiley & Sons, 1994.

[20] Antonio Pich. The Standard Model of Electroweak Interactions. 2012.

[21] Peter Dunne. Looking for consistency in the construction and use of feynman diagrams. *Physics Education*, 36(5):366, 2001.

[22] Jonathan L. Rosner. The Eightfold way. 2001.

[23] C. Becchi. Introduction to gauge theories. 1996.

[24] R.K. Ellis, W.J. Stirling, and B.R. Webber. *QCD and Collider Physics*. Cambridge Monographs on Particle Physics, Nuclear Physics and Cosmology. Cambridge University Press, 2003.

[25] Gudrun Heinrich. Perturbative QCD and jets - I. 2013 CERN-Fermilab HCP Summer School. Aug 2013.

[26] Siegfried Bethke. World Summary of α_s (2012). *Nucl.Phys.Proc.Suppl.*, 234:229–234, 2013.

[27] M.N. Chernodub. Background magnetic field stabilizes QCD string against breaking. 2010.

[28] Gines Martinez. Advances in Quark Gluon Plasma. 2013.

[29] Johann Rafelski. Connecting QGP-Heavy Ion Physics to the Early Universe. *Nucl.Phys.Proc.Suppl.*, 243-244:155–162, 2013.

[30] Miklos Gyulassy. The QGP discovered at RHIC. pages 159–182, 2004.

[31] Helmut Satz. QCD and QGP: A Summary. pages 447–464, 1997.

[32] F. Becattini. An Introduction to the Statistical Hadronization Model. 2009.

[33] Michal Petran. Strangeness and charm in quark-gluon hadronization. 2013.

[34] Jan Fiete Grosse-Oetringhaus, Johannes Peter Wessels, Federico Carminati, and Andreas Morsch. *Measurement of the Charged-Particle Multiplicity in Proton-Proton Collisions with the ALICE Detector*. PhD thesis, Munster U., Muenster, 2009. Presented on 17 Apr 2009.

[35] Bernd-Jochen Schaefer and Mathias Wagner. On the QCD phase structure from effective models. *Prog.Part.Nucl.Phys.*, 62:381, 2009.

[36] Grigor B. Alaverdyan, A.R. Harutyunian, and Yu.L. Vartanian. Neutron stars with a quark core. 1. Equations of state. *Astrophysics*, 46:361–367, 2003.

[37] Alain Coc, Jean-Philippe Uzan, and Elisabeth Vangioni. Standard big bang nucleosynthesis and primordial CNO Abundances after Planck. *JCAP*, 1410(10):050, 2014.

[38] E.A. Pashitskii. "Big Bang" as a first-order phase transition in the early Universe. 2014.

[39] A. Bracco, E. Nappi, and Società italiana di fisica. *From the Big Bang to the Nucleosynthesis*. Advances in Biomedical Spectroscopy Series. IOS Press, 2012.

[40] Joseph I Kapusta. Quark - gluon plasma in the early universe. pages 103–121, 2000.

[41] Katarzyna Grebieszkow. Hot strong matter. *PoS*, DIS2014:018, 2014.

[42] Agnes Mocsy. The sound of the little bangs. `http://www.bnl.gov/rhic/inside/news.php?a=21795`, 2010.

[43] J. Letessier and J. Rafelski. *Hadrons and Quark–Gluon Plasma*. Cambridge Monographs on Particle Physics, Nuclear Physics and Cosmology. Cambridge University Press, 2002.

[44] F. Gelis. Color Glass Condensate and Glasma. *Int.J.Mod.Phys.*, A28:1330001, 2013.

[45] T. Lappi and H. Mäntysaari. Particle production from the Color Glass Condensate: Proton-nucleus collisions in light of the HERA data. *Nucl.Phys.*, A, 2014.

[46] Larry D. McLerran. The Color glass condensate and small x physics: Four lectures. *Lect.Notes Phys.*, 583:291–334, 2002.

[47] Chiho Nonaka and Masayuki Asakawa. Modeling a Realistic Dynamical Model for High Energy Heavy Ion Collisions. *PTEP*, 2012:01A208, 2012.

[48] Helen Caines. What's interesting about strangeness production?: An Overview of recent results. *J.Phys.*, G31:S101–S118, 2005.

[49] A. Capella. Strangeness enhancement in heavy ion collisions. *Phys.Lett.*, B364:175–180, 1995.

[50] Johann Rafelski. Strangeness Enhancement: Challenges and Successes. *Eur.Phys.J.ST*, 155:139–166, 2008.

[51] J. Rafelski. Redistribution of strangeness between quark-gluon plasma and hadronic gas. *Physics Letters B*, 190(1âĂŞ2):167 – 172, 1987.

[52] A.K. Chaudhuri. A short course on Relativistic Heavy Ion Collisions. 2012.

[53] G. Agakishiev et al. Strangeness Enhancement in Cu+Cu and Au+Au Collisions at $\sqrt{s_{NN}}$ = 200 GeV. *Phys.Rev.Lett.*, 108:072301, 2012.

[54] S. Afanasiev et al. Measurement of Direct Photons in Au+Au Collisions at $\sqrt{s_{NN}}$ = 200 GeV. *Phys.Rev.Lett.*, 109:152302, 2012.

[55] M. Klasen, C. Klein-Bösing, F. König, and J.P. Wessels. How robust is a thermal photon interpretation of the ALICE low-p_T data? *JHEP*, 1310:119, 2013.

[56] A. Adare et al. Enhanced production of direct photons in Au+Au collisions at $\sqrt{s_{NN}}$ = 200 GeV and implications for the initial temperature. *Phys.Rev.Lett.*, 104:132301, 2010.

[57] Stephen D. Ellis and Davison E. Soper. Successive combination jet algorithm for hadron collisions. *Phys.Rev.*, D48:3160–3166, 1993.

[58] Matteo Cacciari, Gavin P. Salam, and Gregory Soyez. The Anti-k(t) jet clustering algorithm. *JHEP*, 0804:063, 2008.

[59] Alan D. Martin. Proton structure, Partons, QCD, DGLAP and beyond. *Acta Phys.Polon.*, B39:2025–2062, 2008.

[60] G.R. Boroun and S. Zarrin. An approximate approach to the nonlinear DGLAP evaluation equation. *Eur.Phys.J.Plus*, 128:119, 2013.

[61] K. Aamodt et al. Suppression of Charged Particle Production at Large Transverse Momentum in Central Pb–Pb Collisions at $\sqrt{s_{NN}}$ = 2.76 TeV. *Phys.Lett.*, B696:30–39, 2011.

[62] Jean-Paul Blaizot and Jean-Yves Ollitrault. J / psi suppression in Pb Pb collisions: A Hint of quark - gluon plasma production? *Phys.Rev.Lett.*, 77:1703–1706, 1996.

[63] T Matsui and Helmut Satz. J/psi suppression by quark-gluon plasma formation. *Phys. Lett. B*, 178(BNL-38344. 4):416–422. 17 p, Jun 1986.

[64] Alfredo Vega and Jorge Flores. Heavy quarkonium properties from Cornell potential using variational method and supersymmetric quantum mechanic. 2014.

[65] Agnes Mocsy. Potential Models for Quarkonia. *Eur.Phys.J.*, C61:705–710, 2009.

[66] Betty Abelev et al. J/ψ suppression at forward rapidity in Pb-Pb collisions at $\sqrt{s_{NN}}$ = 2.76 TeV. *Phys.Rev.Lett.*, 109:072301, 2012.

[67] C. Markert, R. Bellwied, and I. Vitev. Formation and decay of hadronic resonances in the QGP. *Phys.Lett.*, B669:92–97, 2008.

[68] A.G. Knospe. Hadronic resonance production in Pb-Pb collisions at the ALICE experiment. *J.Phys.Conf.Ser.*, 420:012018, 2013.

[69] V.L. Eletsky, B.L. Ioffe, and Joseph I. Kapusta. Mass shift, width broadening and spectral density of rho mesons produced in heavy ion collisions. *Nucl.Phys.*, A661:514–517, 1999.

[70] E. Halkiadakis. Proceedings for TASI 2009 Summer School on 'Physics of the Large and the Small': Introduction to the LHC experiments. 2010.

[71] John C. Collins, Davison E. Soper, and George F. Sterman. Factorization of Hard Processes in QCD. *Adv.Ser.Direct.High Energy Phys.*, 5:1–91, 1988.

[72] Giovanni Antonio Chirilli. High-Energy QCD factorization from DIS to pA collisions. *Int.J.Mod.Phys.Conf.Ser.*, 20:200–207, 2012.

[73] Ivan Vitev. The Perturbative QCD factorization approach in high energy nuclear collisions. *J.Phys.*, G31:S557–S572, 2005.

[74] 17. fragmentation functions in e + e, ep and pp collisions 1 17. fragmentation functions in e + e, ep and pp collisions.

[75] E. Pace, G. Salme, and F.M. Lev. Deep inelastic scattering and final state interaction in an exactly solvable relativistic model. *Phys.Rev.*, C57:2655–2668, 1998.

[76] Alberto Accardi and Jian-Wei Qiu. Collinear factorization for deep inelastic scattering structure functions at large Bjorken x(B). *JHEP*, 0807:090, 2008.

[77] Ringaile Placakyte. Parton Distribution Functions. 2011.

[78] Walter T. Giele, Stephane A. Keller, and David A. Kosower. Parton distribution function uncertainties. 2001.

[79] C. Targett-Adams. Structure functions and parton distribution functions at the HERA ep collider. pages 227–232, 2005.

[80] Kunihiro Nagano. Parton Distribution Functions: Impact of HERA. 2008.

[81] Gerhard John Krige. CERN from the mid-1960s to the late 1970s. Some preliminaries. 1987.

[82] CNGS. Cern neutrinos to gran sasso. `https://proj-cngs.web.cern.ch/proj-cngs/Download/Download.htm`, 2010.

[83] John Krige. The 1984 nobel physics prize for heterogeneous engineering. *Minerva*, 39(4):425–443, 2001.

[84] T. Berners-Lee. The world-wide web initiative, 1993.

[85] R. Bouclier, G. Charpak, Z. DimÄĎovski, G. Fischer, F. Sauli, G. Coignet, and G. FlÃijgge. Investigation of some properties of multiwire proportional chambers. *Nuclear Instruments and Methods*, 88(1):149 – 161, 1970.

[86] Georges Aad et al. Observation of a new particle in the search for the Standard Model Higgs boson with the ATLAS detector at the LHC. *Phys.Lett.*, B716:1–29, 2012.

[87] Serguei Chatrchyan et al. Observation of a new boson at a mass of 125 GeV with the CMS experiment at the LHC. *Phys.Lett.*, B716:30–61, 2012.

[88] C.E. Hill, A. Lombardi, R. Scrivens, M. Vretenar, A. Feschenko, et al. Tests of the CERN proton linac performance for LHC - type beams. *eConf*, C000821:TUD17, 2000.

[89] D Manglunki. LEIR operations for the LHC and future plans. 2013.

[90] Dan Faircloth. Ion sources for high-power hadron accelerators. 2013.

[91] Charles Hill. The cern hadron ion sources. `http://linac2.home.cern.ch/linac2/sources/source.htm`, 1999.

[92] Simone Gilardoni, Django Manglunki, Jean-Paul Burnet, Christian Carli, Michel Chanel, et al. Fifty years of the CERN Proton Synchrotron : Volume 2. 2013.

[93] P. Lefevre. Present and Future Performance of the CERN PS Accelerator Complex. 1977.

[94] P. Lefaasvre T. S. Pettersson. The Large Hadron Collider: conceptual design. *CERN-AC-95-05 LHC*, 1995. .

[95] J.L. Abelleira Fernandez et al. A Large Hadron Electron Collider at CERN: Report on the Physics and Design Concepts for Machine and Detector. *J.Phys.*, G39:075001, 2012.

[96] Lyndon Evans and Philip Bryant. LHC Machine. *JINST*, 3:S08001, 2008.

[97] Oliver S. Bruning, P. Collier, P. Lebrun, S. Myers, R. Ostojic, et al. LHC Design Report. 1. The LHC Main Ring. 2004.

[98] O. Buning, P. Collier, P. Lebrun, S. Myers, R. Ostojic, et al. LHC Design Report. 2. The LHC infrastructure and general services. 2004.

[99] M. Benedikt, P. Collier, V. Mertens, J. Poole, and K. Schindl. LHC Design Report. 3. The LHC injector chain. 2004.

[100] Lhc portal. `http://www.lhcportal.com/Forum/viewtopic.php?t=46`, 2009.

[101] A. Perin, J. Casas-Cubillos, S. Claudet, C. Darve, G. Ferlin, et al. Commissioning of the cryogenics of the LHC long straight sections. *AIP Conf.Proc.*, 1218:1309–1316, 2010.

[102] G. de Rijk, M. Bajko, M. Cornelis, M. Durante, P. Fessia, J. Miles, M. Modena, G. Molinari, J. Rinn, F. Savary, K. Schirm, F. Simon, D. Tommasini, T. Tortschanoff, and J. Vlogaert. Status report on the lhc main magnet production. *Applied Superconductivity, IEEE Transactions on*, 15(2):1078–1083, June 2005.

[103] Collisions. `http://lhc-machine-outreach.web.cern.ch/lhc-machine-outreach/collisions.htm`.

[104] Lhc programme coordination web pages. `http://lpc.web.cern.ch/lpc/`, 2015.

[105] S. Dittmaier et al. Handbook of LHC Higgs Cross Sections: 1. Inclusive Observables. 2011.

[106] Nikolaos Rompotis. Beyond Standard Model Higgs boson physics with the ATLAS experiment at the LHC. 2014.

[107] Gail G. Hanson. Searching for the higgs. *Physics*, 2:106, Dec 2009.

[108] Tobias Golling. LHC searches for physics beyond the Standard Model with top quarks. *J.Phys.Conf.Ser.*, 452:012010, 2013.

[109] John Ellis. Searching for Particle Physics Beyond the Standard Model at the LHC and Elsewhere. *AIP Conf.Proc.*, 1446:9–28, 2012.

[110] Sung-Won Lee. Searches for Physics Beyond the Standard Model at CMS. 2010.

[111] Fabiola Gianotti and Michelangelo L. Mangano. LHC physics: The First one-two year(s). pages 3–26, 2005.

[112] S. Aronson, K. Assamagan, H. Gordon, M. Leite, Micheal J. Levine, et al. A Nuclear physics program at the ATLAS experiment at the CERN large hadron collider. 2002.

[113] Olga Kodolova and Michael Murray. Heavy Ion Physics Program in CMS Experiment. *Nucl.Phys.*, A830:97C–104C, 2009.

[114] G. Aad et al. The ATLAS Experiment at the CERN Large Hadron Collider. *JINST*, 3:S08003, 2008.

[115] Johannes Albrecht. Search for New Physics in rare decays at LHCb. *Nucl.Phys.Proc.Suppl.*, 241-242:49–54, 2013.

[116] F Carminati et al. ALICE: Physics performance report, volume I. *J.Phys.*, G30:1517–1763, 2004.

[117] B Alessandro et al. ALICE: Physics performance report, volume II. *J.Phys.*, G32:1295–2040, 2006.

[118] The alice experiment at the cern lhc. *JINST*, 3(08):S08002, 2008.

[119] P.G. Kuijer. Commissioning and Prospects for Early Physics with ALICE. *Nucl.Phys.*, A830:81C–88C, 2009.

[120] A. Rossi and for the ALICE Collaboration. Alice Alignment, Tracking and Physics Performance Results. *ArXiv e-prints*, January 2011.

[121] C. Fabjan and J. Schukraft. The story of ALICE: Building the dedicated heavy ion detector at LHC. *ArXiv e-prints*, January 2011.

[122] The alice tpc, a large 3-dimensional tracking device with fast readout for ultra-high multiplicity events. *Nuclear Instruments and Methods in Physics Research Section A: Accelerators, Spectrometers, Detectors and Associated Equipment*, 622(1):316 – 367, 2010.

[123] K. Aamodt et al. Production of pions, kaons and protons in *pp* collisions at $\sqrt{s}$ = 900 GeV with ALICE at the LHC. *Eur.Phys.J.*, C71:1655, 2011.

[124] P Cortese et al. ALICE technical design report on forward detectors: FMD, T0 and V0. 2004.

[125] E. Abbas et al. Performance of the ALICE VZERO system. *JINST*, 8:P10016, 2013.

[126] S. Gorbunov et al. Alice hlt high speed tracking on gpu. *Nuclear Science, IEEE Transactions on*, 58(4):1845–1851, Aug 2011.

[127] D. Evans, S. Fedor, G.T. Jones, P. Jovanovic, A. Jusko, L. Kralik, R. Lietava, L. Sandor, J. Urban, and O. Villalobos-Baillie. The alice central trigger system. In *Real Time Conference, 2005. 14th IEEE-NPSS*, pages 5 pp.–, June 2005.

[128] F. Carena, W. Carena, S. Chapeland, V. Chibante Barroso, F. Costa, E. Dénes, R. Divià, U. Fuchs, A. Grigore, T. Kiss, G. Simonetti, C. Soós, A. Telesca, P. Vande Vyvre, and B. von Haller. The {ALICE} data acquisition system. *Nuclear Instruments and Methods in Physics Research Section A: Accelerators, Spectrometers, Detectors and Associated Equipment*, 741(0):130 – 162, 2014.

[129] G Rubin, P Van de Vyvre, P Csató, T Kiss, Z Meggyesi, J Sulyán, L Szendrei, G Harangozo, J Harangozo, I Novák, S Szilágyi, and G Vesztergombi. Development of the ALICE detector data link prototype. (CERN-ALI-98-09. CERN-ALICE-PUB-98-09), 1997.

[130] F Carena, W Carena, S Chapeland, E Dénes, R Divià, T Kiss, J C Martin, K Schossmaier, C Soos, P Van de Vyvre, and Alessandro Vascotto. The ALICE Data-Acquisition Read-out Receiver card. 2004.

[131] R. Brun, P. Buncic, F. Carminati, A. Morsch, F. Rademakers, et al. Computing in ALICE. *Nucl.Instrum.Meth.*, A502:339–346, 2003.

[132] F Carminati and Andreas Morsch. Simulation in ALICE. Technical Report physics/0306092, CERN, Geneva, Jun 2003.

[133] Andreas Morsch. ALICE Simulation Framework. (CERN-ALI-99-38. CERN-ALICE-PUB-99-38):4 p, Nov 1999.

[134] I G Caballero, F Carminati, and Andreas Morsch. ALICE experience with GEANT4. Technical Report physics/0306025, CERN, Geneva, Jun 2003.

[135] I Hrivnacova and V V Berejnov. GEANT4 in ALICE. Technical Report CERN-ALI-99-40. CERN-ALICE-PUB-99-40, CERN, Geneva, Nov 1999. Proposal of abstract for CHEP2000.

[136] A. Fasso', A. Ferrari, S. Roesler, J. Ranft, P. R. Sala, G. Battistoni, M. Campanella, F. Cerutti, L. De Biaggi, E. Gadioli, M. V. Garzelli, F. Ballarini, A. Ottolenghi, D. Scannicchio, M. Carboni, M. Pelliccioni, R. Villari, V. Andersen, A. Empl, K. Lee, L. Pinsky, T. N. Wilson, and N. Zapp. The FLUKA code: present applications and future developments. *ArXiv Physics e-prints*, June 2003.

[137] D Adamová, J Chudoba, T Kouba, P Mendez Lorenzo, P Saiz, J ęvec, and J Hampl. Status of the grid computing for the alice experiment in the czech republic. *Journal of Physics: Conference Series*, 219(7):072023, 2010.

[138] A Bogdanov, L Jancurova, A Kiryanov, V Kotlyar, V Mitsyn, Y Lyublev, E Ryabinkin, G Shabratova, L Stepanova, V Tikhomirov, V Trofimov, W Urazmetov, D Utkin, A Zarochentsev, and S Zotkin. Grid processing and analysis of alice data at distributed russian tier2 centre ? rdig. *Journal of Physics: Conference Series*, 219(7):072054, 2010.

[139] S Bagnasco, L Betev, P Buncic, F Carminati, C Cirstoiu, C Grigoras, A Hayrapetyan, A Harutyunyan, A J Peters, and P Saiz. Alien: Alice environment on the grid. *Journal of Physics: Conference Series*, 119(6):062012, 2008.

[140] Muhammad Ajaz, Seforo Mohlalisi, Peter Hristov, and Jean Pierre Revol. Quality assurance for the ALICE Monte Carlo procedure. 2009.

[141] K Nakamura and Particle Data Group. Review of particle physics. *Journal of Physics G: Nuclear and Particle Physics*, 37(7A):075021, 2010.

[142] Zi-Wei Lin, Che Ming Ko, Bao-An Li, Bin Zhang, and Subrata Pal. A Multi-phase transport model for relativistic heavy ion collisions. *Phys.Rev.*, C72:064901, 2005.

[143] R Brun, F Bruyant, M Maire, A C McPherson, and P Zanarini. *GEANT 3: user's guide Geant 3.10, Geant 3.11; rev. version*. CERN, Geneva, 1987.

[144] A. Bhasin, D. Evans, G.T. Jones, P. JovanoviÄĞ, A. Jusko, R. Kour, M. Krivda, C. Lazzeroni, R. Lietava, Z.L. Matthews, S. Navin, R.J. Platt, H. Snow, J.D. Tapia Takaki, and O. Villalobos Baillie. Minimum bias trigger for pp physics with alice. *Indian Journal of Physics*, 84(12):1733–1738, 2010.

[145] G Aglieri Rinella and ALICE collaboration. Performance of alice detector and electronics under first beam conditions. *Journal of Instrumentation*, 5(12):C12008, 2010.

[146] Betty Abelev et al. Measurement of inelastic, single- and double-diffraction cross sections in proton–proton collisions at the LHC with ALICE. *Eur.Phys.J.*, C73(6):2456, 2013.

[147] Eva Sicking, J P Wessels, and A Morsch. *Multiplicity Dependence of Two-Particle Angular Correlations in Proton-Proton Collisions Measured with ALICE at the LHC*. PhD thesis, Munster U., Münster, Dec 2012. Presented 26 Sep 2012.

[148] R. Brun, P. Canal, M. Frank, A. Kreshuk, S. Linev, P. Russo, and F. Rademakers. Developments in ROOT I/O and trees. *Journal of Physics Conference Series*, 119(4):042006, July 2008.

[149] N. Pataki. C++ Standard Template Library by template specialized containers. *ArXiv e-prints*, November 2011.

[150] A. Kusina, T. Stavreva, S. Berge, F.I. Olness, I. Schienbein, et al. Strange Quark PDFs and Implications for Drell-Yan Boson Production at the LHC. *Phys.Rev.*, D85:094028, 2012.

[151] M. Batra and A. Upadhyay. Strange and non-strange sea quark-gluon effects in nucleons. *Nucl.Phys.*, A922:126–139, 2014.

[152] Gunnar Graf, Elvira Santini, Hannah Petersen, Jan Steinheimer, Michael Mitrovski, et al. Strangeness production in hadronic models and recombination models. *J.Phys.*, G37:094010, 2010.

[153] Thorsten Renk and Kari J. Eskola. Hard dihadron correlations in heavy-ion collisions at RHIC and LHC. *Phys.Rev.*, C84:054913, 2011.

[154] Rudolph C. Hwa and C.B. Yang. Dihadron correlation in jets produced in heavy-ion collisions. *Phys.Rev.*, C70:054902, 2004.

[155] Serguei Chatrchyan et al. Studies of azimuthal dihadron correlations in ultra-central PbPb collisions at $\sqrt{s_{NN}} = 2.76$ TeV. *JHEP*, 1402:088, 2014.

[156] Xiangrong Zhu. Two-particle correlations in pp and Pb-Pb collisions with ALICE. 2013.

[157] Betty Abelev et al. Long-range angular correlations on the near and away side in p-Pb collisions at $\sqrt{s_{NN}} = 5.02$ TeV. *Phys.Lett.*, B719:29–41, 2013.

[158] P. Bartalini, E.L. Berger, B. Blok, G. Calucci, R. Corke, et al. Multi-Parton Interactions at the LHC. 2011.

[159] V.P. Druzhinin, S.I. Eidelman, S.I. Serednyakov, and E.P. Solodov. Hadron Production via e+e- Collisions with Initial State Radiation. *Rev.Mod.Phys.*, 83:1545, 2011.

[160] F. O. Dur A poundses, V. P. Gon A Salves, F. S. Navarra, A. L. V. R. dos Reis, and G. Wilk. Gluon saturation and leading particle spectra in pp collisions. *Brazilian Journal of Physics*, 37:122 – 125, 03 2007.

[161] Serguei Chatrchyan et al. Measurement of the underlying event activity in pp collisions at $\sqrt{s} = 0.9$ and 7 TeV with the novel jet-area/median approach. *JHEP*, 1208:130, 2012.

[162] Betty Bezverkhny Abelev et al. Underlying event measurements in pp collisions at $\sqrt{s} = 0.9$ and 7 tev with the alice experiment at the lhc. *Journal of High Energy Physics*, 2012(7), 2012.

[163] S.S. Adler et al. Dense-Medium Modifications to Jet-Induced Hadron Pair Distributions in Au+Au Collisions at s(NN)**(1/2) = 200-GeV. *Phys.Rev.Lett.*, 97:052301, 2006.

[164] Mark Fischler and David Sachs. An Object oriented minimization package for HEP. *eConf*, C0303241:MOLT004, 2003.

[165] K. P. Nelson and S. Umarov. The Relationship between Tsallis Statistics, the Fourier Transform, and Nonlinear Coupling. *ArXiv e-prints*, November 2008.

[166] Constantino Tsallis, Silvio V. F. Levy, André M. C. Souza, and Roger Maynard. Statistical-mechanical foundation of the ubiquity of the lévy distributions in nature. *Phys. Rev. Lett.*, 77:5442–5442, Dec 1996.

[167] Roger Barlow. Systematic errors: Facts and fictions. pages 134–144, 2002.

[168] Betty Bezverkhny Abelev et al. K^0_S and Λ production in Pb-Pb collisions at $\sqrt{s_{NN}}$ = 2.76 TeV. *Phys.Rev.Lett.*, 111:222301, 2013.

[169] Peter Zeiler Skands. Tuning Monte Carlo Generators: The Perugia Tunes. *Phys.Rev.*, D82:074018, 2010.

[170] Andy Buckley, Hendrik Hoeth, Heiko Lacker, Holger Schulz, and Eike von Seggern. Monte Carlo tuning and generator validation. pages 267–283, 2009.

[171] Betty Bezverkhny Abelev et al. Multiplicity Dependence of Pion, Kaon, Proton and Lambda Production in p-Pb Collisions at $\sqrt{s_{NN}}$ = 5.02 TeV. *Phys.Lett.*, B728:25–38, 2014.

[172] E. L de Santa Helena, C.M. Nascimento, and G.J.L. Gerhardt. An alternative way to characterize a q-gaussian distribution by a robust heavy tail measurement. 2014.

[173] Aki-Hiro Sato. q-gaussian distributions and multiplicative stochastic processes for analysis of multiple financial time series. In *Journal of Physics: Conference Series*, volume 201, page 012008. IOP Publishing, 2010.

[174] Torbjorn Sjostrand, Stephen Mrenna, and Peter Z. Skands. PYTHIA 6.4 Physics and Manual. *JHEP*, 0605:026, 2006.

[175] Sparsh Navin. Diffraction in Pythia. 2010.

[176] Drago Velicanu. Ridge correlation structure in high multiplicity pp collisions with CMS. *J.Phys.*, G38:124051, 2011.

[177] Betty Abelev et al. Measurement of electrons from semileptonic heavy-flavour hadron decays in pp collisions at $\sqrt{s} = 7$ TeV. *Phys.Rev.*, D86:112007, 2012.

[178] Christian Lippmann. Particle identification. *Nucl.Instrum.Meth.*, A666:148–172, 2012.

[179] *ALICE Time-Of-Flight system (TOF): Technical Design Report*. Technical Design Report ALICE. CERN, Geneva, 2000.

[180] Levente Molnar. The ALICE HMPID detector ready for collisions at the LHC. *Nucl.Instrum.Meth.*, A595:27–30, 2008.

[181] Yvonne Pachmayer. Physics with the ALICE Transition Radiation Detector. *Nucl.Instrum.Meth.*, A706:6–11, 2013.

[182] Jochen Klein. Triggering with the ALICE TRD. *Nucl.Instrum.Meth.*, A706:23–28, 2013.

[183] *J. Phys. G: Nucl. Part. Phys.*, 34(8):S719, 2007.

[184] Per Thomas Hille. Commissioning of the ALICE PHOS Detector and Integration into the ALICE High Level Trigger.

[185] P. Crochet. The alice forward muon spectrometer. *Pramana*, 60(5):1051–1054, 2003.

[186] A. Morsch. The {ALICE} forward muon spectrometer at the {LHC}. *Nuclear Physics A*, 638(1?2):571c – 574c, 1998. Quark Matter '97 Proceedings of the Thirteenth International Conference on Ultra-Relativistic Nucleus-Nucleus Collisions.

[187] C. Oppedisano. Performance of the alice zero degree calorimeters in pb-pb collisions at lhc. In *Nuclear Science Symposium and Medical Imaging Conference (NSS/MIC), 2011 IEEE*, pages 2055–2059, Oct 2011.